M2LW-20OR0402036

Light Water Reactor Sustainability Program

Evaluation of Critical Parameters to Model Stress Corrosion Crack Initiation in Alloy 600 and Alloy 182 in PWR Primary Water

September 2020

U.S. Department of Energy

Office of Nuclear Energy

M2LW-20OR0402036

Evaluation of Critical Parameters to Model Stress Corrosion Crack Initiation in Alloy 600 and Alloy 182 in PWR Primary Water

Ziqing Zhai
Jing Wang
Mychailo B. Toloczko
Stephen M. Bruemmer

Pacific Northwest National Laboratory

September 2020

Prepared for the
U.S. Department of Energy
Office of Nuclear Energy

ABSTRACT

Conventional Ni-base Alloy 600 is still in use in many operating domestic pressurized water reactors (PWR), especially in thick-section components where primary water stress corrosion crack (PWSCC) has been observed and is a concern to PWR life extension. While SCC initiation is considered to encompass the majority of the lifespan of Alloy 600 components, mechanistic understanding of this process remained insufficient for better lifetime predictions, safety assessments and risk management during extended operation of nation's existing LWR fleet. This report provides a detailed review of the extensive PWSCC initiation research performed thus far on Alloy 600 at PNNL under LWRS. It highlights the effects established for multiple parameters such as applied stress, cold work, and temperature on PWSCC initiation in Alloy 600. It also summarizes the systematic data analysis conducted in parallel with SCC initiation testing that elucidated the transition criteria between different SCC initiation precursor stages and quantified the influence of key parameters. This key information has enabled the development of an SCC initiation model based on improved mechanistic understanding, of which the details is also presented in this report.

Meanwhile, Alloy 182 was widely used to LWR pressure boundary construction as the compatible weld metals of Alloy 600 and has been shown to be susceptible to SCC in service. LWRS is collaborating with the U.S. Nuclear Regulation Commission (NRC) and the Electric Power Research Institute (EPRI) on a joint program on SCC initiation testing of Alloy 182. In this report, a brief summary is provided on the test status of Alloy 182. Its SCC initiation behavior is compared to Alloy 600 and the implications on the applicability of the SCC initiation model developed for Alloy 600 to predict Alloy 182 behavior is discussed.

ACKNOWLEDGEMENT

The authors gratefully acknowledge the financial support from the U.S. Department of Energy, Office of Nuclear Energy, for the Light Water Reactor Sustainability Program. In addition, support is recognized from the U.S. NRC on SCC crack growth rate testing of Alloy 600 materials, as well as from U.S. NRC and EPRI on SCC initiation testing of Alloy 182 and additional Alloy 600 materials. These collaborations have been essential to the success of the LWRS SCC initiation research. The helpful discussions with Dr. Daniel Schreiber and Dr. Matthew Olszta on interpretations of microscopy characterization results of intergranular (IG) damage precursors in Alloy 600 is graciously acknowledged. Dr. John Deibler is recognized for finite element modeling on stress intensity estimation of small cracks. Key technical assistance from Ryan Bouffioux, Ferdinan Colon, Ryley Peterson, Anthony Guzman, and Michael Blazon is acknowledged for SCC initiation testing and specimen preparation activities.

CONTENTS

FIGURES

TABLES

ACRONYMS

AW	as-welded
BSE	backscatter electron
CDF	cumulative distribution function
CF	cold-forged
CGR	crack growth rate
CR	cold-rolled
CRDM	control rod drive mechanism
CT	compact tension
CTS	cold tensile strained
CW	cold-worked
DCPD	direct current potential drop
DDC	ductility dip cracking
DH	dissolved hydrogen
EBSD	electron backscattered diffraction
ECP	electrochemical corrosion potential
EDF	Électricité de France
EDM	electric discharge machining
EDS	energy dispersive x-ray spectroscopy
EPRI	Electric Power Research Institute
FEM	finite element modeling
GB	grain boundary
HAGB	high-angle grain boundary
IG	intergranular
IGA	intergranular attack
LWR	light water reactor
MA	mill-annealed
NRC	Nuclear Regulatory Commission
PDF	probability density function
PNNL	Pacific Northwest National Laboratory
PWR	pressurized water reactor
PWSCC	primary water stress corrosion crack
SA	solution-annealed
SCC	stress corrosion cracking
SE	secondary electron
SEM	scanning electron microscope
SGB	solidification grain boundaries
SRDM	strain-rate damage mechanics
SSRT	slow-strain rate test
TG	transgranular
TT	thermally treated
xLPR	Extremely Low Probability of Rupture program
YS	yield stress

Evaluation of Critical Parameters to Model Stress Corrosion Crack Initiation in Alloy 600 and Alloy 182 in PWR Primary Water

PROJECT BACKGROUND

Objective

This research project addresses one of the least understood aspects of stress corrosion cracking (SCC) for light water reactor (LWR) pressure boundary components - crack initiation. The focus of the work is to investigate important material (composition, processing, microstructure, strength) and environmental (temperature, water chemistry, electrochemical potential, stress) effects on the SCC susceptibility of corrosion-resistant, nickel-base alloys. The primary objectives are to identify mechanisms controlling crack nucleation, investigate the transition from short to long crack growth in these alloys under realistic LWR conditions and help establish the framework to effectively model and mitigate SCC initiation processes.

Approach

Alloy 600 materials were selected for the first phase of SCC initiation experimentation followed by testing on the more resistant Alloy 690 materials. For both alloys, material variants known to influence SCC response are being examined including cold/warm work (forged, rolled and tensile strained), banded/inhomogeneous microstructures (plate versus extruded tubing), grain boundary precipitation (heat-to-heat variations, mill-annealed, solution annealing and changes due to thermal treatments) and surface grinding (various damage depths, surface roughness and nanocrystalline layers). Materials and material conditions have been identified and obtained from an ongoing research project for the U.S. Nuclear Regulatory Commission (NRC) where stress-corrosion crack growth has been characterized, thus creating an important link between SCC initiation and propagation behavior. Detailed examinations have been performed using optical and electron microscopy to establish key bulk and surface microstructural features that may act as initiation precursors. Dedicated test systems with continuous in-situ detection of crack formation were designed and constructed enabling SCC initiation experimentation of a range of Alloy 600 and 690 materials. After SCC testing in high temperature autoclave systems, surface and near-surface characterizations were conducted to document nano-to-microscale initiation precursors leading to macroscopic stress corrosion cracks. The fundamental understanding of how the near-surface microstructure is degraded during high-temperature water exposure is essential to an improved predictive methodology for SCC initiation.

Focus of Current Report

This report builds on the results accumulated through the multi-year PWRSCC initiation research on Alloy 600 at PNNL and offers an in-depth review of the mechanistic insights obtained from systematic testing and characterizations. Previous results have revealed that the SCC initiation in Alloy 600 involves three stages: nucleation and growth of intergranular attack (IGA), short crack growth and coalescence, and transition to stable crack growth. By the end of this fiscal year, constant load SCC initiation tests have been completed on 81 Alloy 600 specimens from eight different heats in various material and cold work conditions with more extensive microstructural characterizations performed on selected specimens. This allowed us to identify critical parameters and establish quantitative relationships for the development of an SCC initiation model for Alloy 600, which is the major focus of this report. In addition, a test

update on Alloy 182 is provided. This activity is carried out through collaboration with the NRC-EPRI joint program where Alloy 182 SCC initiation testing and characterizations are being performed to evaluate the effect of microstructure, cold work, and applied stress on SCC initiation behavior. The applicability of the SCC initiation model proposed for Alloy 600 to predict Alloy 182 will be discussed.

LITERATURE REVIEW OF SCC INITIATION MODELS FOR ALLOY 600

Before diving into details on our test results and attempts for model development, a brief literature review on available models proposed for PWSCC initiation in Alloy 600 is presented in this chapter. While not exhaustive in its coverage, this review provides a quick look at the vast efforts made for predicting Alloy 600 PWSCC initiation through empirical, probabilistic, and mechanistic models. The gaps for more reliable predictions are identified, and our approach to address these gaps are introduced.

Alloy 600 SCC Initiation Models in Literature

Empirical Models

E1. The basic power law model

The most widely used empirical model is the power law model that links applied stress and temperature with SCC initiation time, as in the form of Equation (1) [1, 2]. The power law relationship was initially observed by Bandy and van Rooyen [1] for their testing on Alloy 600 under constant load in high temperature deaerated water. This type of power law model is also selected as one of the recommended models for estimating SCC initiation time in the Extremely Low Probability of Rupture (xLPR) program [3]. The model considers that the SCC initiation time was primarily affected by applied stress and operating temperature in PWR primary water environment. The intrinsic material variabilities are expressed in the form of a constant pre-exponential factor and a stress exponent.

$$\frac{1}{t_{INI,nom}} = A\, exp\left(\frac{-Q}{RT}\right)\sigma^n \quad \sigma \geq \sigma_{th} \tag{1}$$

$t_{INI,nom}$ = initiation time under fixed set of conditions
T = temperature
σ = surface stress
σ_{th} = stress threshold parameter
A = Direct Model 1 proportionality constant
n = stress exponent
Q = activation energy for initiation
R = universal gas constant

E2. The Index Model

The power law model was then included in an "index model" for Alloy 600 empirical applications by Amzallag at EDF [2]. In this model, the initiation time was constructed as in Equations (2) and (3), where the material index I_m describes material intrinsic susceptibility, I_θ is the temperature index, and I_σ is the stress index. The global index for SCC initiation susceptibility is the product of these three indexes. For simplicity in practice, the global susceptibility index measured for an Alloy 600 tube subjected to an applied stress of 450 MPa at 325°C was assigned as 1, serving as the reference point. Therefore, the estimation of minimum failure time can be quickly referenced based on a set of pre-generated table, as in report [4].

$$t_{ini} = \frac{10000}{I_m \cdot I_\theta \cdot I_\sigma} \tag{2}$$

$$I_\theta = exp\left[\left(-\frac{E}{R}\right)\left(\frac{1}{T}-\frac{1}{598}\right)\right], \quad I_\sigma = \left(\frac{\sigma}{450}\right)^4 \tag{3}$$

E3. The Strain-Rate Damage Mechanics (SRDM) Model and its Derivatives

The SRDM model was developed by Garud and EPRI to simulate the formation and growth of a part-through circumferential crack in steam generator tubings to reduce the effort for on-site engineering and maintenance activities [5-7]. Instead of using applied stress as the principal variable, the model assumes the local IGSCC damage rate $\dot{D}$ is related to the total local strain rate $\dot{\varepsilon}$ by a power law relation with Arrhenius type dependence on temperature:

$$\dot{D} = \alpha \exp\left(\frac{-Q}{RT}\right)(\dot{\varepsilon})^{\phi} \tag{4}$$

where α is a coefficient related to cold work and Q is the apparent activation energy.

Due to the complexity involved with predicting the strain rate in this semi-empirical approach, Garud later developed a simplified model to predict SCC initiation time under constant stress condition using a logarithm relationship with stress ratio in the form of Equation (5) where A is a parameter related to mechanical strength properties. The logarithm relationship was developed based on the curves best-fitted to experimental data, and its applicability has been validated using field data [6]. The key difference between this model and the power law model is that instead of dependence on the power of applied stress, the SCC initiation time is proportional to the logarithm of to the ratio of yield stress over the applied stress. Conceptually this approach is more generalized than power law since it includes the effects of initial mechanical strength in the model.

$$t_{ini} = \alpha\, exp\left(\frac{Q}{RT}\right) ln\left(A\left(\frac{\sigma_y}{\sigma}\right)\right) \tag{5}$$

Garud later developed a more generalized model for EPRI based on Equation (5) with detailed parameterizations focusing on the effects of cold work [8], as shown in Equation (6). It has the same form as the previous model, with the addition of an approximation a_{n} to explicitly assess cold work effects and a modifying term z to consider threshold stress effect. The model parameters were estimated and validated using field data published in the 1980s and 1990s. This is another model that is being considered in the xLPR program for establishing SCC initiation time estimation. One limitation of this model is that it requires quantification of a large number of parameters often through empirical equations fitted to published data using additional variables, of which the values also need to be determined first. Any proper estimation of SCC initiation times would require significant amount of data be generated from parametric studies, which renders it challenging in reality.

$$t_I = a_{\mathrm{n}} \lambda\, ln\left(\frac{A - z}{\frac{\sigma}{\sigma_y} - z}\right) \frac{ln\, A}{ln\left(\frac{A - z}{1 - z}\right)} \tag{6}$$

a_{n} = normalized cold work-SCC resistance factor

λ = material/environment factor, including the Arrhenius temperature dependence, defined to have unit of time

A = material/stress resistance parameter

$\frac{\sigma}{\sigma_y}$ = stress severity, equals effective tensile stress vs. tensile yield strength

z = stress severity – threshold stress model parameter

E4. EdF's Phenomenological Model

Le Hong et al. proposed a phenomenological model with a focus on the surface cold work effect on SCC initiation based on constant load and slow strain rate test (SSRT) results on three Alloy 600MA tubing heats [9]. The macroscopic SCC initiation is thought to take place through an incubation period, followed by slow propagation, and finally a rapid propagation stage. The incubation period is short in most cases and only becomes long in sub-yield stress condition. The SCC initiation is considered to be dominated by the slow propagation stage, which is mainly affected by strain rate, surface condition, and material microstructure. Equations (7) and (8) illustrate the initiation model developed based on SSRT testing results, where a_c is the critical crack length calculated from stress intensity factor at initiation time, T_f is the SCC initiation time, $\dot{\varepsilon}$ is the strain rate, W_D is the width of diffraction peak corresponding to the cold work level using X-ray diffraction, and $\dot{\eta}$ is the intergranular viscosity. This model can be generalized to constant load scenarios through linking strain rate to applied stress. The authors demonstrated that replacing strain rate and solve the equation resulted in a power law relationship between initiation time T_f and applied stress. The author further discussed the potential of adding temperature effects by including an Arrhenius relationship in the strain rate function.

$$a_c = \int_0^{T_f} \left(\frac{da}{dt}\right) dt \tag{7}$$

$$da/dt = C_4 \dot{\varepsilon}^{0.58} {W_D}^{1.9} \eta^{-0.76} \tag{8}$$

Probabilistic Models

P1. Models Based on Probability Distributions

Another popular model category for SCC initiation is the probabilistic models. As the detailed SCC mechanism is unclear and the industry has limited ability to predict SCC with deterministic models, probabilistic models, which are already commonly used for product lifetime estimation, failure analysis and survival analysis, have been proposed. A thorough analysis of the applicability of using statistical models to estimate Alloy 600 PWSCC behavior was performed by Gorman and Staehle [10], in which Weibull, log-normal, Gaussian, logistics, and extreme value distributions were evaluated for a series of field data on steam generator tube failures. The report concluded that both Weibull and log-normal represent the SCC degradation well. Note that in this report the degradation refers to the significant through wall cracking instead of SCC initiation.

The probability density function (PDF) and cumulative distribution function (CDF) for the standard form Weibull (will be denoted as two-parameter Weibull hereafter) distribution are shown in Equation (9) and (10), where θ is the scale parameter, β is the shape parameter, and t is the time to failure (in this case, time to initiation). In the two-parameter Weibull distribution, the shape parameter β is related to the failure rate, where $\beta<1$ indicates decreasing failure rate over time, $\beta=1$ indicates a constant failure rate (such as failure by random events), and $\beta>1$ indicates increasing failure rate over l A third parameter t_0 can be added to the model in the t/θ term to form a three-parameter Weibull model.

$$f(t;\beta,\theta) = \frac{\beta}{\theta}\left(\frac{t}{\theta}\right)^{\beta-1} exp\left(-\left(\frac{t}{\theta}\right)^{\beta}\right) \tag{9}$$

$$F(t;\beta,\theta) = 1 - exp\left(-\left(\frac{t}{\theta}\right)^{\beta}\right) \tag{10}$$

Later, Staehle explored using Weibull distribution to detect "earliest failure", which means the ones occur at an extremely low probability in the range of 0.0001 to 0.01, on the secondary side of PWR steam generator tubings [11]. The approach illustrated in the report provided a physically based statistical framework and extensive statistical analyses on relevant factors including metallurgical (cold work, surface finish, etc.), environmental (pH, stress, temperature, etc.), and inherent variabilities in SCC tests, for predicting the early penetration. In the report, the scale parameter θ is observed to have a power law relationship with applied stress and an Arrhenius relationship with test temperature T [Equation (11)]. A maximum likelihood expectation approach is used for the following fitting process. To utilize as many data as possible, Park et al. [12] proposed to include non-initiated data, which is called right-censored data, from laboratory testing. Consequently, the θ in this case is represented in Equation (12), where η_r is a pre-exponential factor and n_r is the stress ratio exponent. The shape parameter β is also very important for detecting early penetration, however its determination remains unclear as correlation study with other factors does not follow consistent pattern. Staehle tested β=1 and β=4 and suggested the former for early penetration case.

$$\theta = \mathrm{C}\, exp(\, Q/T)\sigma^{-n} \tag{11}$$

$$\theta = \eta_r \left(\frac{\sigma}{\sigma_y}\right)^{-n_r} \tag{12}$$

P2. Monte Carlo Simulation based on Weibull Distribution by EdF

Follow the evolution of industry's needs, Benhamou and Amzallag reported a Monte Carlo based approach for prediction of SCC initiation [13]. The Monte Carlo method was employed by the authors with the aim to overcome the Weibull model's limitation in over-estimation of both short and long life times of components. The issue is caused by parameterization of Weibull models, which does not include intrinsic material variabilities that affect SCC initiation. The Monte Carlo approach was conducted on the aforementioned index model [2]. Instead of using a determined mean value for parameter, input the inherent dispersion in materials and environment were taken into account via random sampling. More specifically, the materials index values were assumed to follow a log-normal distribution, based on analysis of both laboratory and field data; activation energy was assumed to follow a normal distribution; operating temperatures of components were assigned a normal distribution based on thermal-hydraulic studies; and stress on materials was also assumed following a normal distribution. The result shows that the Monte Carlo approach produced a better fit to field for the short and long failure times than using the Weibull method alone.

P3. Simulation of Macroscopic SCC Initiation incorporating Crack Coalescence by IHI

Sakakibara et al. investigated the applicability of an SCC engineering model first developed for sensitized 304 stainless steel in BWR environment to Alloy 600 SCC initiation in PWR primary water environment [14]. The model simulates the macroscopic SCC initiation in progressive steps involving crack nucleation at random sites, and crack growth and coalescence until it reaches a critical size relevant to engineering cracks. The number of initiated microcracks were collected from accelerated constant load exposures of Alloy 600MA tensile specimens in a 400°C hydrogenated steam environment. The data is shown to follow a Poisson random process model [Equation (13)], where λ is the hazard rate and m' is a rank obtained by adequately classifying the numbers of cracks within the field of examination.

$$f(m';\lambda) = \frac{\lambda^{m'}}{m'!} exp(-\lambda) \tag{13}$$

Statistical distributions were assumed to other critical variables to enable the simulation. For example, the initiation time for each crack is assumed to follow an exponential distribution, the initiation site follows a uniform distribution, and the crack length and depth follows a log-normal distribution. The size, aspect ratio, and growth rate of microcracks initially generated were estimated via empirical fitting of experimental data. In addition, this simulation incorporated the scenario of crack coalescence using criterion developed for SS304-BWR system based on test data and fracture mechanics studies.

Mechanistic Models

M1. EDF's Local IGSCC Engineering Model

In recent years, Couvant et al. developed a local model to predict PWSCC initiation in Alloy 600 focusing on the physical phenomenon of SCC occurrence based on grain boundary (GB) oxidation and stress localization [15-17]. It builds upon existing data at EDF on the influence of various environmental and material factors on SCC initiation of Alloy 600, but a series of new tests were also conducted for refined model calibration. This model simulates three scenarios: incubation, initiation, and crack extension. The incubation period is where intergranular (IG) oxidation takes place and the maximum depth p_i is assumed to have a logarithmic dependency on time and is modeled using Equation (14). It also depends on dissolved hydrogen (DH) via the term of $f(\Delta EcP)$ linking DH to the electrochemical potential of the alloy and has an Arrhenius relationship with temperature that is included in the term of $g(T)$:

$$p_i = \frac{1}{a_i} ln(1 + b_i t) \times f(\Delta EcP) \times g(T) \tag{14}$$

The initiation in this model is defined as the failure of an oxidized GB and assumed possible when: 1. the oxidation depth is deeper than a critical value; and 2. the local stress at GB is higher than the critical opening stress. Crystal plasticity modeling is used to estimate the stress concentrations at GB during this step to evaluate whether the local stress has reached the critical opening stress.

Finally, this model incorporates a stage of crack extension where a crack is growing at low crack growth rates (CGR) estimated by a sigmoid function of stress intensity *K* before transition into a fast growing "engineering" crack. An upper bound of the sigmoid crack extension law is given as below:

$$\max(CGR) = \ g_1 \times \frac{K^{g_2}}{1 + \exp\left[-g_3 \times (K - g_4)\right]} \times f_H \times \exp\left(\frac{-Q_g}{RT}\right) \tag{15}$$

where g_1 to g_4 are constant, and f_H is a term related to ΔEcP the potential difference of the electrochemical potential of the alloy.

Gaps and PNNL's Approach

A summary of the key features of the above-mentioned models is provided in Table 1. It's obvious that the majority of existing Alloy 600 SCC initiation models predict time to SCC initiation based on one or a few influencing factors via an empirical or probabilistic relationship derived from field data on degraded steam generator tubes or laboratory data acquired using conventional test methods such as U-bend and SSRT. Although they work to some degree of satisfactory, there are several issues concerning a wider application of these models. Firstly, an unambiguous definition of SCC initiation is missing. The data used as time to SCC initiation in these models are usually associated with the time to rupture or the detection of a visible crack on a specimen at test interruptions. This indicates a large component of crack growth is involved in the data and can result in significant error in prediction. In addition, the not-well-known or not-well-controlled environmental, material, or mechanical conditions from which the data was

generated can also affect the accuracy of prediction. For example, plant operations usually involve multiple shutdowns and startup that can change the environment and stress state of steam generator tubes. Another example is that the U-bend specimens that are often used to generate SCC initiation data can suffer from significant creep relaxation. These variations can affect material SCC initiation behavior and determination of parameter dependencies but were usually neglected during model development. Finally, IG oxidation has been identified as a necessary precursor to SCC initiation in Alloy 600, but this stage was not considered in most models except a recent local model proposed by EDF. However, the functionality of applied stress and strain is missing in this model for the incubation stage (i.e. IG oxide growth), which is inconsistent with actual scenarios where materials are subject to stress and high-temperature water simultaneously. As a result, a model based on a better mechanistic understanding on the processes leading to a well-defined point of SCC initiation is much needed to facilitate inspection and maintenance planning of Alloy 600 components that are still in service. Thanks to previous investments from LWRS, PNNL has established the state-of-the-art SCC testing technique with well-controlled water chemistry, active load control and in-situ direct current potential drop (DCPD) detection for crack initiation. This capability enabled us to obtain high-quality SCC initiation data that is not compromised by stress relaxation or unknown stress state, drift in electrochemical potential, and uncertainty in time to initiation. Meanwhile, we also conducted complimentary unstressed exposure tests and SCC CGR tests on to determine rate-controlling process in the different stages leading to practical SCC initiation. With a series of carefully designed parametric study on multiple Alloy 600 heats, we have established relationships between key parameters and SCC initiation of Alloy 600 in PWR primary water. We have also developed innovative characterization methods to generate quantitative data for the development of a mechanistic-based SCC initiation model. In the following chapters, the test methods we used in this study will be introduced, followed by a detailed summary of test results that led to an improved mechanistic understanding of the PWSCC initiation behavior in Alloy 600 and the model development.

Table 1. Comparison of key features of the models summarized in the literature review.

Model ID & ref.	Model Category	Main Characteristics of the Model	Model outcome	Major Factors Included in Model	Data Source	Test type	Specimen Type
E1 [1]	Empirical	Power-law	Time to initiation (direct)	Stress	Lab	Constant Load	Tensile
E2 [2]	Empirical	Power-law	Time to minimum failure time (direct)	Stress, temperature (T), intrinsic material susceptibility	Mixed	Mixed	Oval tubes, U-bends, field data
E3-1 [5, 7]	Empirical	Power-law	Time to initiation (indirect via critical accumulated damage)	Strain rate, T, intrinsic material susceptibility	NM*	NM*	NM*
E3-2 [6]	Empirical	Logarithm	Time to initiation (direct)	Stress, T	Mixed	Constant load for Lab	Reverse U-bend for Lab
E3-3 [8]	Empirical	Logarithm	Time to initiation (direct)	Stress, T, Cold work	Mixed	Mixed	Mixed
E4 [9]	Empirical	Power-law	Time to initiation (indirect via critical crack size)	Strain rate, Stress, T, Surface cold work	Lab	SSRT and constant load	Tube
P1 [10, 11]	Statistical	Weibull, and other statistical distributions	Probability to failure or earliest penetration	Stress, various environmental and material factors	Field in [10]; Mixed in [11]	Multiple in [11]	Multiple in [11]
P2 [13]	Statistical	Monte Carlo with various statistical distributions	Probability to initiation	Stress, T, intrinsic material susceptibility	Field	Field	Field
P3 [14]	Statistical	Monte Carlo with Poisson Process and various statistical distributions	Probability to initiation	Stress, T, grain size, crack coalescence	Lab	Uniaxial constant load	Tensile
M1 [15-17]	Mechanistic	Logarithmic for incubation, sigmoidal for crack growth, crystal plasticity modeling for stress estimation	Time to initiation (indirect via critical crack size)	Stress, environment (T and DH), GB carbide coverage, and intrinsic material susceptibility	Lab	SSRT, constant load tensile, unstressed exposure and post-exposure straining	Tensile

EXPERIMENTAL METHODS

As mentioned in the previous chapter, high-quality test data is a necessity for improving the mechanistic understanding of SCC initiation in Alloy 600 and to aid model development. In this chapter, the state-of-the-art test method we developed in this program to evaluate PWSCC initiation response of Ni-base alloys will be presented in detail, along with two complimentary test methods we used to investigate individual steps associated with macroscopic SCC initiation in Alloy 600. The microstructural characterization methods we employed to examine SCC initiation features and to collect quantitative data will also be described.

SCC Initiation Testing on Alloys 600 and 182

Specimen Design and Surface Preparation

A key goal for this program is to correlate SCC initiation response to various aspects of materials processing including bulk microstructure, near surface microstructure, surface texture, existence of surface defects and applied stress level. Prior experience with Alloys 600 and 690 has shown that their SCC resistance is extremely sensitive to the degree of plastic deformation, and therefore accurate characterization in the test specimen was an important factor in the specimen design. Several different specimen types were considered for the crack initiation testing including U-bend, bent beam, tensile, and blunt-notch compact tension (CT) geometries.

A tensile specimen geometry was the most attractive because it has none of the shortcomings associated with U-bend, bent beam and blunt-notch specimens. This design produces a uniaxial stress state, the gauge region is accessible allowing control over the surface microstructure, various types of micro/macroscopic defects can be generated and there are several ways to produce specimens with well-known amounts of uniform plastic strain. In addition, prior work at KAPL [18] has shown that DCPD can be effectively used to detect crack initiation. Several factors played into the specific design of the tensile specimens employed for SCC initiation testing [19], the most important was maximizing the ability of DCPD to detect crack initiation. The DCPD signal is affected not only by crack growth, but also by elastic and plastic strains including creep. Initiation tests are typically conducted at or near the yield stress (YS) where small amounts of creep occur at PWR primary water temperatures. To reduce the magnitude of the creep contribution to the DCPD signal, the gauge length was kept as short as possible while allowing a sufficient number of grain boundaries to be exposed. The short gauge length also played favorably for the desire to be able to fully survey the specimen gauge surface for cracks by scanning electron microscopy (SEM) in a reasonable length of time. This characterization is essential to assess crack precursors and the transition from intergranular attack (IGA) to micro-crack nucleation to short crack growth in Alloy 600. In addition, one practical issue was the desire to have an initiation specimen size that fit within the dimensions of a 0.5T CT specimen such that any material prepared for SCC crack growth studies could also be used for SCC crack initiation studies. The final tensile design was refined to the point that a crack initiation specimen could be cut from an SCC-tested 0.5T CT specimen as long the crack length to width ratio (a/W) in the CT specimen did not exceed 0.7. This a/W is below the range of typical crack lengths in SCC studies conducted by PNNL allowing routine extraction of crack initiation specimens as desired. Other factors for the design were the need to electrically isolate the specimen and eliminate any significant stress risers.

The effect of resistivity change on the DCPD signal for Ni-base alloys exposed to PWR relevant temperatures was measured and subtracted from the gauge signal. This was accomplished by monitoring a larger diameter region of the specimen where the stress is approximately 15% of the gauge stress (depending on gauge diameter). For this low stress region, neither crack initiation nor any substantial amount of creep will occur, and the inherent resistivity change of the material can be measured. The specimen dimensions along with a photo of the specimen are shown in Figure 1. After taking into account all design considerations, a 30.5 mm tall tensile specimen with a 4.0 mm gauge length was selected.

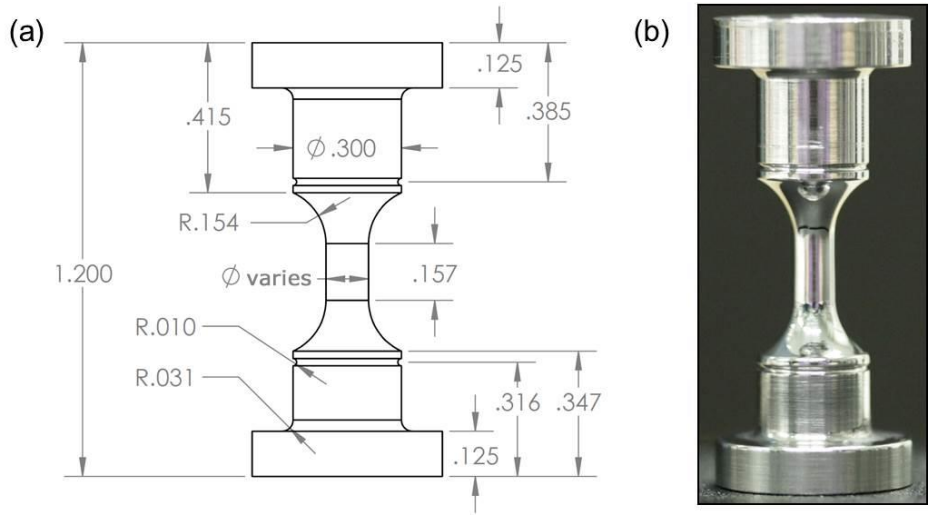

Figure 1. PNNL initiation specimen design. Gauge diameter is selected based on material strength and can be varied from 2.75-4.5 mm (0.11-0.18 inches) and the gauge length is 4.0 mm (0.157 inches). Overall height is 30.5 mm (1.2 inches).

Materials have been tested in various material conditions with or without cold work. Cold working was typically achieved either by cold rolling or cold forging. Cold rolling performed on the plate material was done such that the rolling direction was the same direction as the original plate processing direction. Specimens taken from CRDM tubing were cut with the gauge axis parallel to the CRDM tubing axis. The gauge axis of specimens cut from the plate material was parallel to the "S" direction relative to the plate processing. Prior to insertion of the specimens into the autoclave, the gauge section either was polished to a 1 µm finish or was rough ground. A "C" finish used for some of the specimens attempts to emulate the surface damage layer created by typical service component grinding operations [20]. The details of the surface preparation procedure have been provided elsewhere [21, 22]. Generally, aggressive grinding produces a nanocrystalline layer that promotes corrosion across the entire surface and delays water access to bulk grain boundaries. This has been found to have a small effect on initiation times as discussed in earlier publications [21, 23]. In comparison, a highly polished surface ensures that all grain boundaries reaching the surface are immediately exposed to water. From an examination perspective, a ground surface impairs observation of surface cracks due to the rough surface and microscale fold-overs that often have a crack-like appearance. A polished surface eliminates these complicating factors and enables a better optical and SEM assessment of IGA and crack nucleation as a function of the material, environment and test conditions, therefore most specimens tested after 2015 were given a highly polished surface finish.

Test Methods

Figure 2 shows the load train and DCPD instrumentation for the typical SCC initiation specimen set up at PNNL. Currently two smaller SCC initiation systems and one large SCC initiation system are being used under the scope of LWRS. The two small SCC initiation systems have been converted to test up to 6 fully instrumented specimens during the past year, and the large SCC initiation system allows 36 specimens be tested simultaneously with up to 24 specimens instrumented. The load frame in both types of systems is designed to sustain the load even when individual specimens fail during the test enabling the test to continue for the other specimens loaded in the same string. To make this possible, the controlling software is programed to partially unload the system when a sharp strain increase in an individual specimen is detected by DCPD. The load decrease (typically to ~80% of the starting value) enables the SCC-initiated tensile specimen to fail safely without significantly impacting the entire system. After the failure of the specimen is confirmed (usually by losing DCPD signal), the load is brought back to yield

stress again while monitoring stress versus strain curve using DCPD for every specimen. It is important to note that none of the LWRS Alloy 600 or Alloy 690 specimens have been allowed to fail during an SCC initiation test and all specimens have been removed shortly after DCPD-indicated initiation to assess cracking.

A reversing DCPD technique developed by General Electric [24] and KAPL [25] was adapted with the configuration shown in Figure 3. DCPD voltage across the gauge section is sensitive not only to reduction in cross-sectional area of the gauge region due to crack formation, but also to changes in gauge length and diameter from creep strains that occur during testing. Resistivity drift caused by exposure of Alloy 600 or Alloy 690 at elevated temperature can also produce a substantial contribution to the DCPD signal. In order to minimize the impact of the latter on DCPD data, a reference voltage was also measured across a thick section where significant creep strain and SCC initiation would not occur, and this was subtracted from the gauge voltage. Since creep deformation is believed to have the primary influence on the resistivity-corrected DCPD signal up to the point of initiation, it was decided to report the DCPD response as a strain value. A formula for strain as a function of voltage starts first with the dependence of voltage on gauge dimensions:

$$V = \rho(L/A) \cdot I \tag{16}$$

V is the measured voltage, ρ is the material resistivity, L is the distance between measurement points, A is the cross-sectional area and I is the applied current. Because plastic strain (including creep) is volume conservative, the relationship can be rewritten as:

$$V = (\rho/v)L^2 \cdot I \tag{17}$$

where v is the volume of material between the voltage measurement points. By rearranging this equation to solve for L and inserting it into the equation for true strain ($\varepsilon = \ln(L/L_o)$), strain is obtained as a function of voltage from the following formula:

$$\varepsilon_{\text{referenced}} = \frac{1}{2}\left[\ln\left(\frac{V_{\text{gauge}}}{V_{\text{gauge}_0}}\right) - \ln\left(\frac{V_{\text{ref}}}{V_{\text{ref}_0}}\right)\right] \tag{18}$$

where $\varepsilon_{\text{referenced}}$ is the resistivity corrected creep strain, and "gauge" and "ref" are measurements across the gauge section and reference region, respectively.

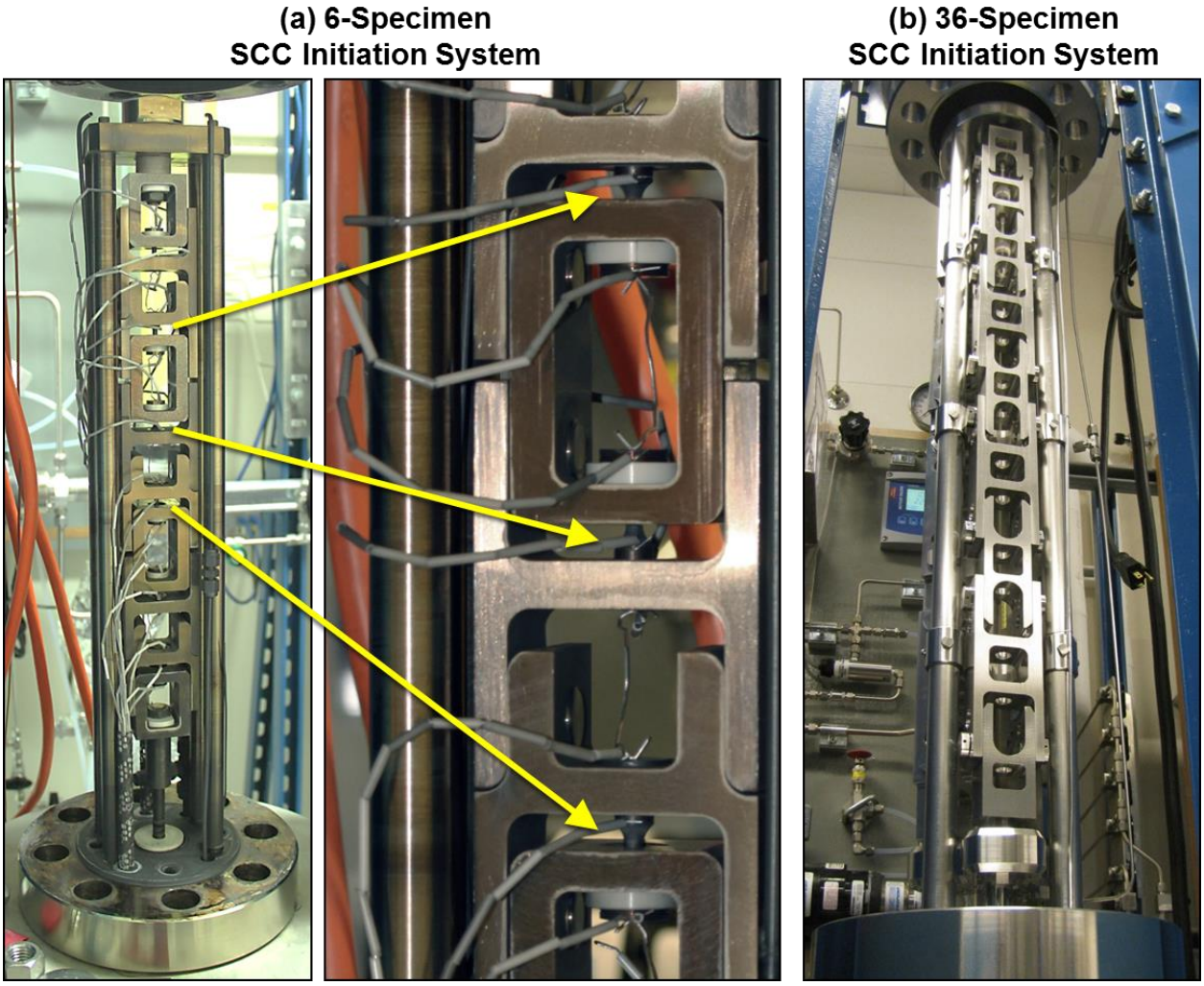

Figure 2. Crack initiation test system load train at PNNL in the (a) small SCC initiation test system with capacity of testing up to 6 fully instrumented specimens and the (b) large SCC initiation test system with capacity of testing up to 24 instrumented specimens and up to 36 specimens in total.

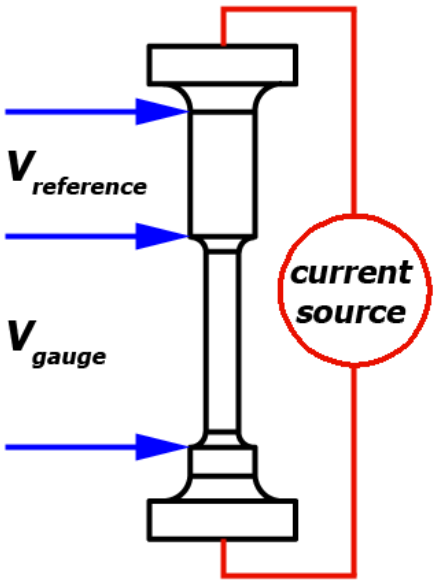

Figure 3. Sketch of the tensile specimen showing desired DCPD measurement points.

Due to the difficulty of spot-welding the wires for DCPD at the idealized voltage measurement points, the actual voltage pickup points were at slightly different locations. The deviation in voltage from idealized pickup points was assessed using finite element modeling (FEM), and a simple linear correction factor as a function of gauge diameter was found to compensate for the non-ideal voltage measurement points. Further details on the development of this DCPD technique can be found in Ref. [26].

Most SCC initiation tests were conducted in an environment that simulates the PWR primary water (1000 ppm B, 2 ppm Li) at 360°C and 20.4 MPa with a dissolved hydrogen concentration of 25 cc/kg to maintain a electrochemical corrosion potential (ECP) at the Ni/NiO stability line. Test temperature effects on SCC initiation have also been evaluated on selected Alloy 600 materials and the dissolved hydrogen content adjusted to maintain the ECP at the Ni/NiO stability line. Nearly all specimens have been tested at their yield stress under constant load with a small number evaluating the influence of lower applied stresses. Full load was applied to the specimens within 1-2 days of reaching the test temperature enabling specimens to be pre-oxidized before loading. At the start of a test, the target load (the load at ~0.2% plastic strain) was achieved over a period of ~1 hour at a constant strain rate of ~10^{-5} mm/s. This rate was chosen to load specimens to their yield stress sufficiently fast to reduce the risk for SCC formation during the initial loading. It also allows DCPD to monitor the stress-strain evolution with a sufficiently low noise level during this loading step. As shown in Figure 4, one specimen would sometimes yield slightly earlier than the others in a multi-specimen load train system due to intrinsic difference in yield strength and/or gauge diameter. In this case, small amounts of plastic strain up to ~1.5% were allowed in order to achieve yield in the other specimens. The specimens were then held at actively controlled constant load until crack initiation. All relevant environmental parameters and DCPD data were monitored and continuously written to a file. If a test was interrupted for surface examinations of precursor damage, or if a specimen had exhibited crack initiation, the remaining specimens were taken back to their original load upon restart of the test, again while monitoring stress versus strain during loading. Figure 5 shows the evolution of both non-referenced and referenced strains throughout exposure of a plate specimen. As mentioned in the previous section, by subtracting the reference voltage from the gauge voltage, the contribution of resistivity drift is eliminated in the referenced strain response. While creep and cracking are both likely to be simultaneously contributing to the measured response, the SCC initiation time is determined as any obvious increase in strain rate. Tests were stopped after clear confirmation of DCPD-based initiation to allow detailed characterizations of the specimen just after the onset of initiation as well as any accompanying specimens that had not yet initiated.

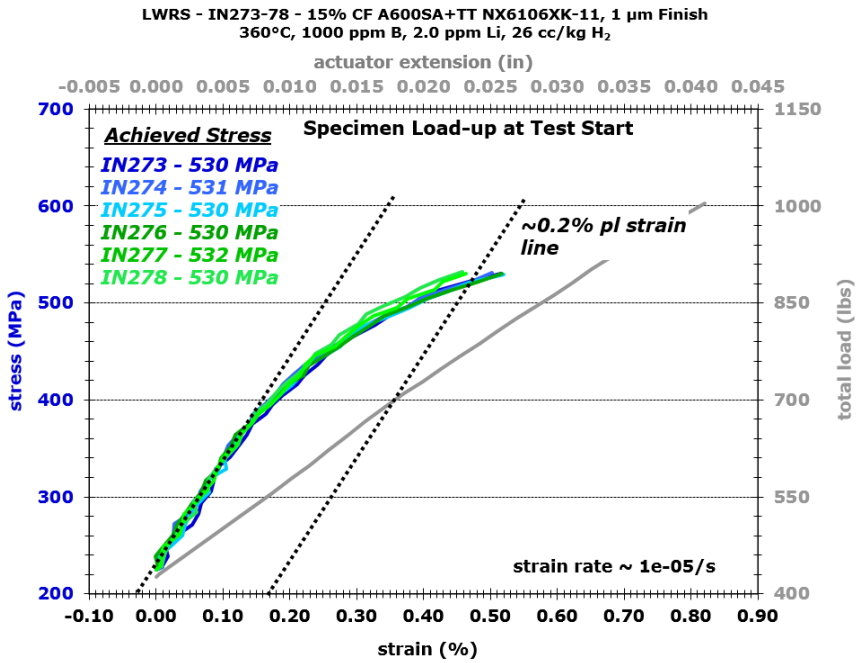

Figure 4. Example of stress versus strain plot during initial loading of tensile specimens for SCC initiation testing. The displacement in actuator and the total load is plotted in the secondary x (upper) and y (right) axis, respectively.

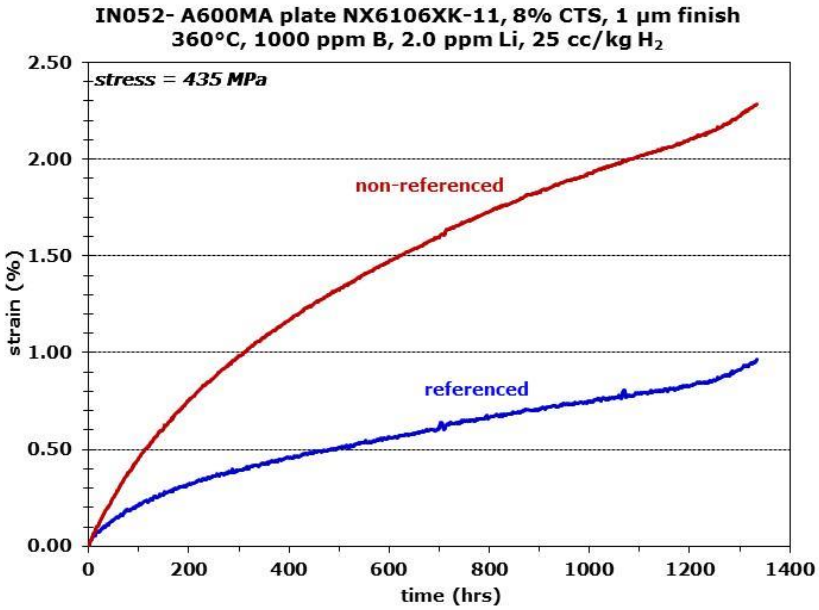

Figure 5. Non-referenced and referenced DCPD strain response for IN052, an 8%CW specimen from Alloy 600MA plate heat NX6106XK-11.

Complimentary Unstressed Exposure Testing on Alloy 600

Corrosion tests on unstressed specimens were conducted in simulated PWR primary water to assess material condition effects on IGA in collaboration with a recent EPRI project [27] at PNNL. Three material conditions were evaluated: as-received, mill annealed (MA); solution annealed (SA) at 1100°C and thermally treated (SA+TT) at 705°C. Circular plate coupons prepared using electric discharge machining (EDM) that were ~15 mm in diameter and ~5 mm in thickness (Figure 2A) were used for the unstressed exposure tests. All surfaces of the as-machined coupons were removed with coarse SiC paper to eliminate contaminants introduced by the EDM process (S and Cu in particular). Both flat surfaces were then polished to 600 grit SiC and one side was further polished to an electron backscatter diffraction (EBSD) quality finish with 50 nm colloidal silica. In total three heats were evaluated, but the results presented herein focus on heat NX6106XK-11 since SCC initiation tests have only been performed for this heat. Coupons were produced from each material condition in triplicate with the intention of extracting one coupon from each material set at different exposure times of 1000 hours, 4400 hours and ~20,000 hours. The final exposure is still ongoing and has reached 16,000 hours at the time of this report. The fully assembled coupon tree installed into the stainless-steel autoclave is shown in Figure 6B. Coupons were suspended individually with a Pt wire wrapped in a ceramic sheath to prevent galvanic coupling. The edge of each coupon was also engraved with the sample name to confirm the material heat and thermomechanical history. A summary table of the coupons from the heat NX6106XK-11 and their exposure times are identified in Table 2.

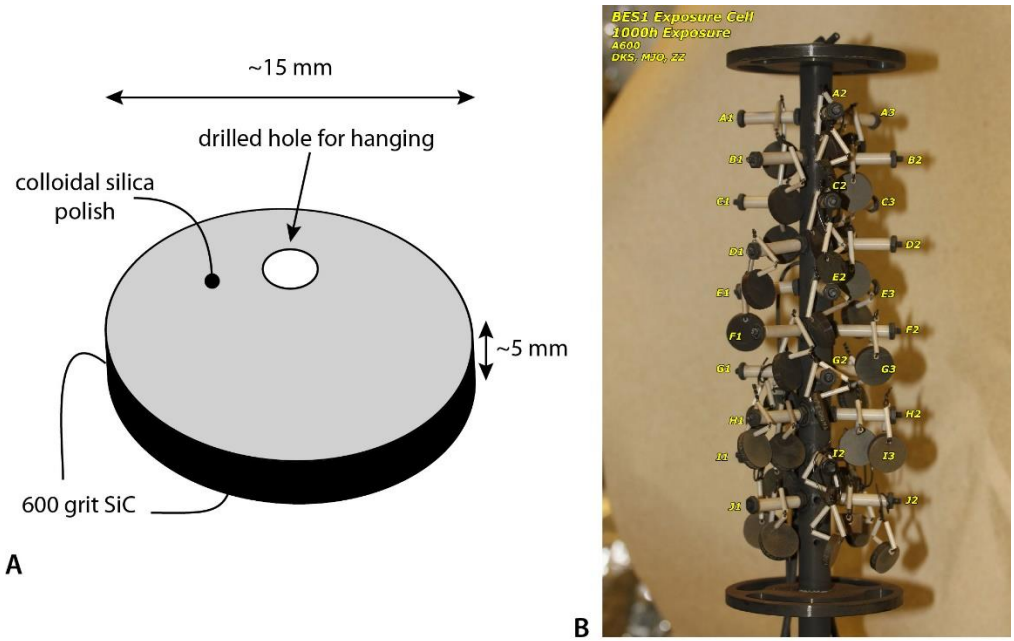

Figure 6. (A) Schematic illustration of the exposure coupon geometry and respective surface finishes. (B) Photograph of the exposure coupons on the tree mounted into the stainless autoclave. Coupons of each material condition were produced in triplicate and each coupon is suspended from the exposure tree by ceramic-encased Pt wire strung through a drilled hole.

The water chemistry was established at 1000 ppm B and 2 ppm LiOH to simulate PWR primary water with temperature maintained at 360°C to facilitate accelerated testing of the IG corrosion/oxidation response. The electrochemical potential was set at the Ni/NiO line using a dissolved concentration of 25 cc H_2/kg H_2O where IGA/SCC susceptibility is expected to be maximized. At each target exposure time, the autoclave was cooled and drained then one coupon from each material condition was extracted, rinsed

and dried for destructive examinations. The remaining coupons were returned to the autoclave to resume exposure to longer times.

Table 2. Summary of Alloy 600 heat NX6106XK-11 exposure coupons. Each row corresponds to an individual coupon of the indicated material condition and time exposed to 360°C simulated PWR primary water.

Thermal History	Cold Work	Time (h)
SA	0	1000
SA	0	4400
SA	0	25000+*
SA+TT	0	1000
SA+TT	0	4400
SA+TT	0	25000+*
MA	15%	1000
MA	15%	4400
MA	15%	25000+*
SA	15%	1000
SA	15%	4400
SA	15%	25000+*
SA+TT	15%	1000
SA+TT	15%	4400
SA+TT	15%	25000+*

* Ongoing exposure as of August 2020.

Complimentary Crack Growth Rate Testing on Alloy 600

To help explain the SCC initiation results, testing was conducted in collaboration with an NRC project on SCC crack growth and the joint NRC-EPRI project on SCC initiation to evaluate temperature and stress intensity (*K*) effects. Standard 0.5T compact tension (CT) specimen is used for crack growth rate (CGR) testing and a schematic of the specimen geometry is provided in Figure 7. Four different heats (SA tubing heat 31907, MA plate heat 522068, MA CRDM nozzle heat WNP5, and MA plate heat 33375-2B) in 15%CF condition were evaluated for the temperature effects at a *K* level of ~20-25 MPa√m. Temperatures of 360, 342, 325 and 300°C were assessed with dissolved hydrogen concentrations adjusted to maintain Ni/NiO ECP conditions. One specimen was prepared from each heat and loaded into the test systems in pairs after a precrack of ~1.1 mm long from the notch was produced by fatigue in air. The tests started with a series of routine transitioning steps to maximize the opportunity of IG engagement for SCC evaluation. DCPD technique was used on all specimens to monitor the CGR response in-situ. An example is shown in Figure 8, where rapid SCC growth occurred at 360°C and enabled temperature effects to be evaluated quickly as documented in Figure 9. A consistent decrease in CGRs can be seen with decreasing temperature from 360 to 342 to 325 to 300°C in all four tested specimens, enabling activation energy to be calculated for each heat. The results will be shown later in the next chapter.

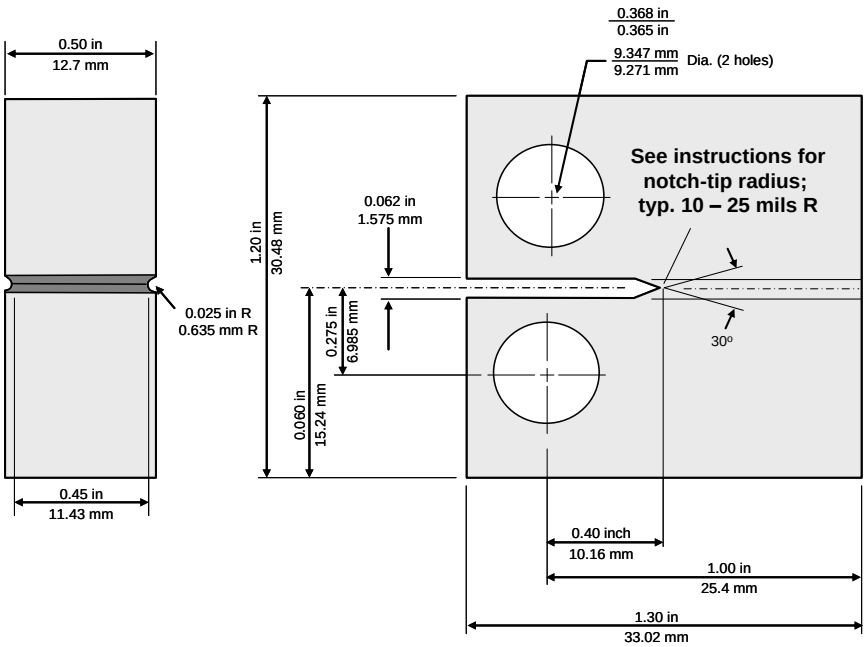

Figure 7. Dimensions of the 0.5T CT specimen used for CGR testing.

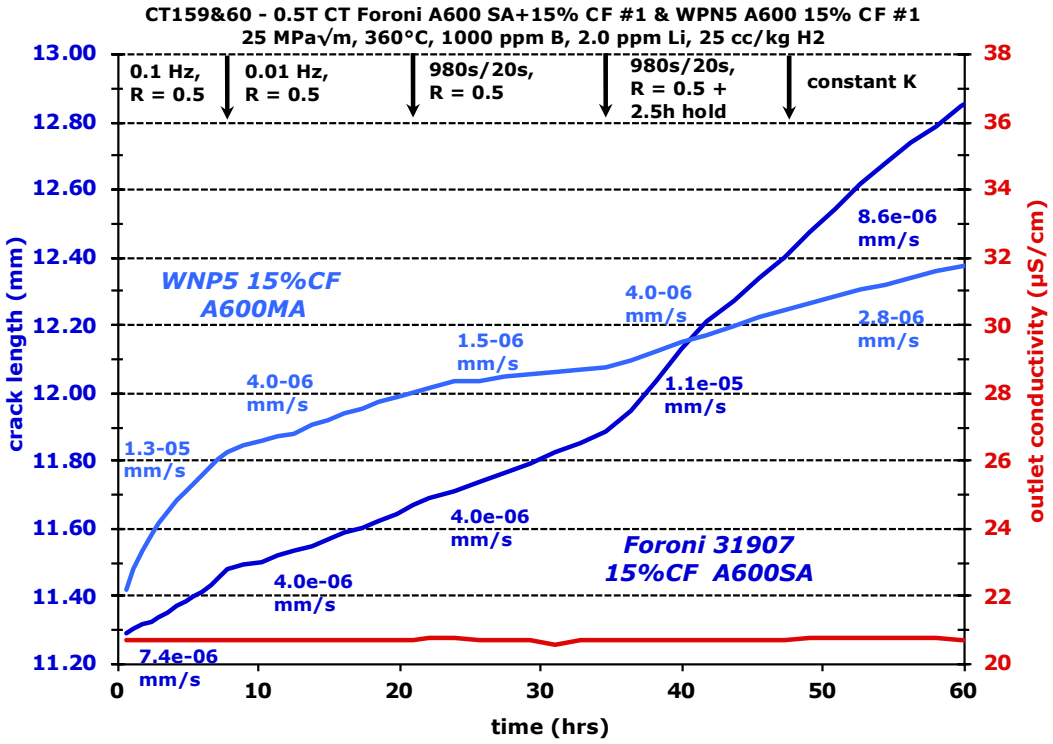

Figure 8. DCPD-indicated CGR response during the transitioning steps for the 15% CF Alloy 600 specimens CT159 (heat 31907) and CT160 (heat WNP5) in 360°C simulated PWR primary water.

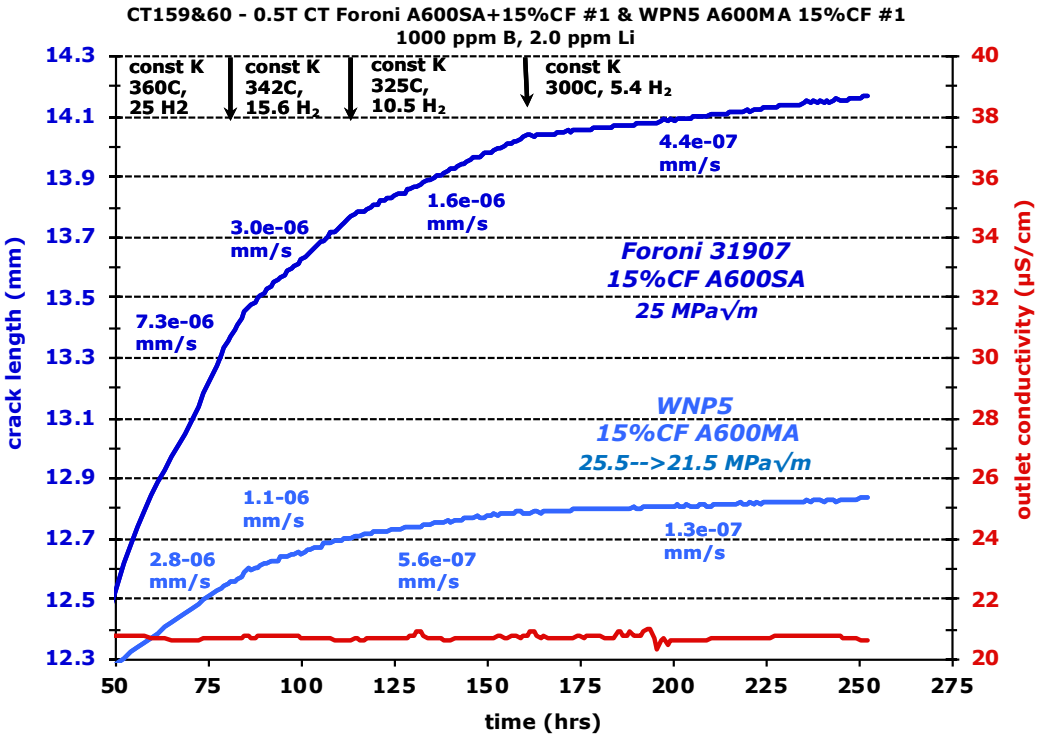

Figure 9. DCPD-indicated SCC CGR response as a function of test temperature at constant *K* in simulated PWR primary water for the 15% CF Alloy 600 specimens CT159 (heat 31907) and CT160 (heat WNP5).

The evaluation of the effects of low-*K* on SCC crack growth response was performed on five different heats (SA tubing heat 31907, MA plate heat 522068, MA CRDM nozzle heat WNP5, MA plate heat 33375-2B, and MA plate heat NX6106XK-11) also in the 15%CF condition. The tests were performed in either 325 or 360°C simulated PWR water with dissolved hydrogen concentration at Ni/NiO stability line. For most tests, the SCC evaluation would start at a higher *K* level of ~20–25 MPa√m and was re-established consecutively by 5 MPa√m decrement until a low *K* of ~5 MPa√m was reached. The load drop was achieved via negative d*K*/d*a* using a cycle+hold step over a distance of 50–100 µm, and constant load would be re-established afterwards for a sufficiently long period of time (>100 hours) so that a SCCCGR can be measured confidently. In Figure 10, an example is provided showing the SCC evaluation for two specimens from 15 to 10 MPa√m. The constant load testing at each *K* level continued for ~120 hours showing a decreased SCC CGR value with decreasing *K*.

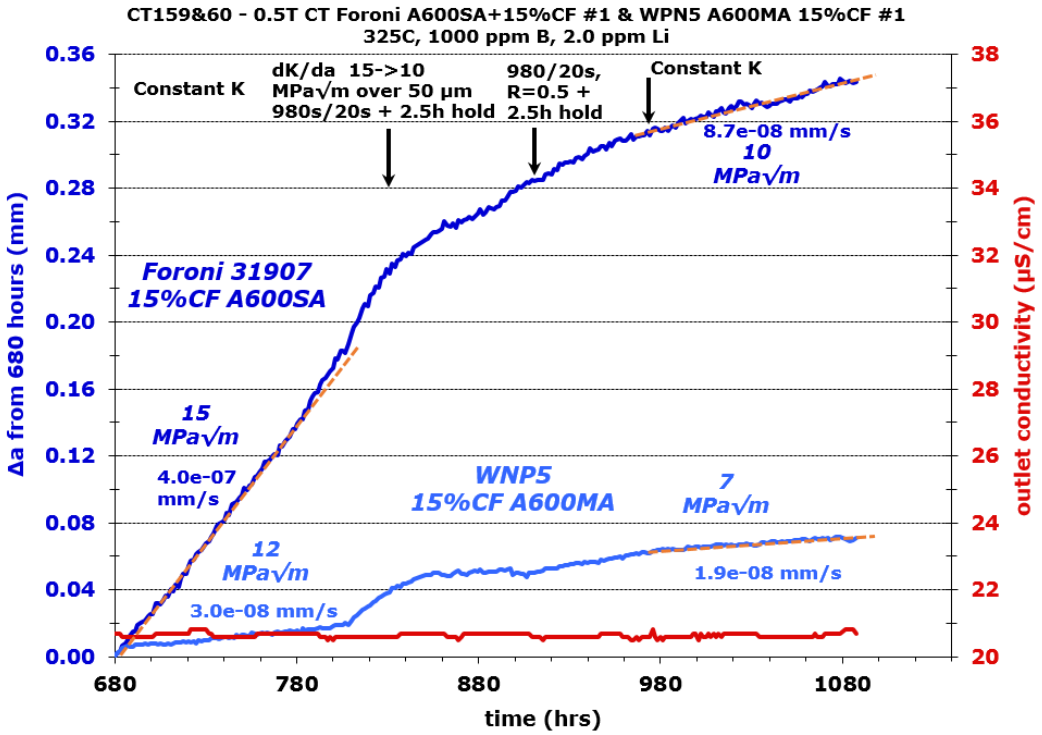

Figure 10. DCPD-indicated CGR response for two Alloy 600 specimens CT159 (SA+15%CF 31907) and CT160 (MA+15%CF WNP5) tested in tandem at a lower *K* level (10 MPa√m) followed by transitioning from another low *K* level (15 MPa√m).

Microstructural Characterizations

The microstructural characterizations focus mainly on acquiring morphological and quantitative information of IGA and cracks for further analyses. Most examination was performed using a JEOL 7600 SEM in the backscatter electron (BSE) mode. The characterization procedure for each test will be detailed in the following sections. Supplementary high-resolution characterizations by transmission electron microscopy and atom probe tomography when needed. The latter techniques were utilized to better understand the IG corrosion/oxidation behavior as a function of GB chemistry and are reported elsewhere [28]. The content below focuses on the characterization methods performed using SEM.

Examination of Alloy 600 Unstressed Exposure Coupons

The exposure coupons taken out at each test interruption were cut in half using EDM. One half of each coupon was mounted into epoxy and mechanically polished to a “mirror finish” using colloidal silica for SEM examinations in cross-section. It is critical to ensure that the edge of the cross-sections do not curve during mechanical polish, otherwise it will easily lead to inaccurate measurements of the depth (usually less than 2 µm) of IGA located on these edges. To accomplish this, the cross-sectioned coupons were clamped between two stainless steel fixture plates like a sandwich using coiled spacers (Figure 11). The whole set was then mounted into epoxy and polished to an EBSD quality finish with 50 nm colloidal silica. The material of the stainless-steel plates had a similar hardness as the test coupons so that material was removed evenly during polishing to provide a sufficiently flat edge for reliable IGA depth measurement.

Low acceleration voltage was used during SEM imaging to reveal detailed compositional contrast of the IGA. For each examined coupon, the IGA depth measurements were performed on at least 50, as many as 120, neighboring high-energy GBs. This provides a representative sample size for statistical

analysis. In addition, the IGA morphology at some GBs were documented at higher magnifications enabling comparisons between material conditions and exposure times.

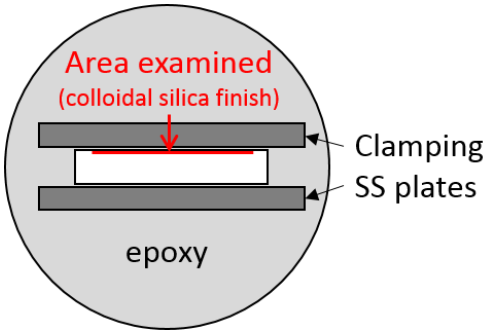

Figure 11. Schematic of the mounted exposure coupons for cross-section examination. In this study, only the side with a colloidal silica finish on the surface was examined.

Examination of Alloys 600 and 182 SCC Initiation Specimens

One key focus of this study is to evaluate the evolution of precursor damage and crack formation in the Alloy 600 having different thermomechanical histories. To achieve this, periodical examinations were performed on the surface and cross-section of SCC initiation specimens whenever possible through planned test interruptions, or at least at the conclusion of the tests. More specifically, the surface examination was performed on all specimens after each test interruption and at the end of the test using a JEOL 7600 SEM. Oxford Aztec software was used to automate stage movement such that the entire gauge surface could quickly be mapped enabling montages to be created. Four fiducial scribe marks (90° to one another) were made at the button ends of each specimen to keep track of the specimen orientation. Each of the four orientations was then mapped using high-keV BSE montage imaging so that features covered by thin surface oxides can be revealed. As shown in Figure 12, the surface of the entire gauge section and most of the fillet region of the specimens was examined on each rotation.

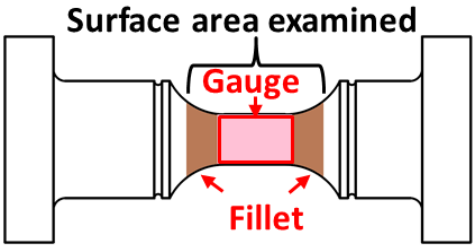

Figure 12. Schematic of the surface area of one rotation mapped in SEM for pre-test examination. The gauge surface mapped in SEM is highlighted in pink and the surface in the fillet region mapped in SEM is highlighted in taupe.

Destructive examinations for precursor damage was also performed on selected specimens removed at test interruption or at the conclusion of the test. The specimens for this observation were sliced into two halves along axial direction using EDM with one half mounted into epoxy and carefully polished to an EBSD quality finish with 50 nm colloidal silica. Similar to the observation conducted on the cross-section of unstressed exposure coupons, low-keV SEM-BSE imaging was performed on more than 100 neighboring high-energy GBs to reveal detailed compositional contrast of the IGA and to measure their depth.

ALLOY 600 TEST RESULTS AND MODEL DEVELOPMENT

While different aspects of the test results on Alloy 600 SCC initiation have been presented in more details in previous reports, an up-to-date summary of tested materials and test status is provided in this chapter. More importantly, it offers a systematic overview of the mechanistic insights gained into PWSCC initiation in Alloy 600 by combing through the data generated via testing and characterizations over the past six years on Alloy 600 in this program and in collaboration with a joint NRC-EPRI SCC initiation program and an NRC SCC CGR program, many are presented for the first time. Key parameters and their effects in the consecutive steps of IGA development and short crack growth and coalescence that lead to practical SCC initiation in Alloy 600 are identified, and the criteria of transition between these steps are established. These data are utilized to develop an SCC initiation model for Alloy 600 and preliminary results are also presented in this chapter.

Overview of Alloy 600 SCC Initiation Test Results

Materials

Eight Alloy 600 heats from different manufacturers were evaluated in the SCC initiation research at PNNL. Most heats and material conditions were evaluated under LWRS, while testing on four heats at a single cold work level were collaborated with an ongoing NRC-EPRI initiation program at PNNL. Their basic information and bulk composition are listed in Table 3. Among these eight materials, four materials (11415, NX6106XK-11, 33375-2B, and 522068) were received in the form of 50.8-76.2 mm (2-3 inch) thick plates. One (31907) was received as a bar with a diameter of 152.4 mm (6 inch) and three others (M3935, WNP5, and 93510) were control rod drive mechanism (CRDM) tubing materials. In particular, M3935 was a CRDM material harvested from the upper head nozzle removed after ~15 years of service [29] in the Davis-Besse Nuclear Power Station and is known to be highly susceptible to PWSCC [30]. In addition, three of these eight materials (31907, 11415, and NX6106XK-11) were chosen for an SCC initiation round robin organized by the International Cooperative Group on Environmentally-Assisted Cracking of Water Reactor Materials, with the objective of generating good quality SCC initiation data for Alloy 600 and evaluating lab-to-lab variability in assessing SCC initiation susceptibility using common test technique. The results of this round robin from multiple laboratories were summarized in a recent publication [31].

The majority of tests were conducted on these materials in cold-worked (CW) condition with at least one cold work level evaluated for each heat. Testing of CW Alloy 600 is motivated by the fact that cold work due to component fabrication and installation was found to be a significant contributor to both initiation and growth of SCC cracks in PWR primary coolant water. Cold working was achieved either by cold tensile straining (CTS), cold rolling (CR) or cold forging (CF). For the plate materials, the direction of rolling or forging was set to be coincident with the original plate processing direction. For the bar and tubing materials, the straining/rolling/forging direction was along the axial direction. The level of cold work evaluated ranged from 7% to 20%, which is considered relevant to the plastic strains produced by component assembly, mechanical finishing and/or welding processes used in plant. Besides the baseline tests of cold-worked materials, several key material, environmental, and mechanical factors on SCC initiation were evaluated with special focuses on surface finish, cold work level, temperature, GB carbide distribution, and applied stress. These factors were selected as they have been considered as of high relevance to engineering applications. As indicated in Table 3, at least two heats, each with a minimum set of three specimens, were investigated for each factor to count for heat-to-heat variability in SCC initiation response.

The base microstructure of these heats differs greatly in grain size and carbide distribution as summarized in Table 4 and as presented in Figures 13 and 24.

Table 3. Bulk compositions, heat treatment conditions, and test focus of the Alloy 600 heats investigated in this study.

Source and Heat No.	Manufacturer & Description	Composition (wt%, unless specified otherwise)	Heat Treatments		Test Focus**				
					Surface Finish	CW level	Temp	Carbide	Stress
GE 31907	Foroni 6”-diameter bar	Ni-15.6Cr-7.92Fe-0.01C-0.46Mn-0.22Si-0.22Al-0.28Ti-0.01Cu-0.0002S-0.009P-46 appm B*	SA	1100ºC/0.5 h, water quench (WQ)			x		
Rolls Royce 11415	Rolls Royce 2”-thick plate	Ni-15.6Cr-8.36Fe-0.04C-0.19Mn-0.20Si-0.03Cu-0.001S-0.003P-1.7 appm B*	SA	1050ºC/1 h, WQ					
PNNL NX6106XK-11	Special Metals 2”-thick plate	Ni-16.4Cr-8.5Fe-0.06C-0.23Mn-0.22Si-0.22Al-0.30Ti-0.01Cu-0.001S-0.004P-83 appm B*	MA	927ºC/3.5 h, WQ	x	x	x	x	
			SA	1100ºC/0.5 h, WQ				x	
			SA+TT	above + 704ºC/12 h, air cooling (AC)				x	
KAPL 33375-2B	G.O. Carlson 2”-thick plate	Ni-14.9Cr-7.4Fe-0.07C-0.42Mn-0.37Si-0.20Al-0.24Ti-0.01Cu-0.001S-0.004P-63 appm B*	MA	Not available					o
ATI 522068	California Metals 3” thick plate	Ni-16.1Cr-9.25Fe-0.05C-0.21Mn-0.14Si-0.06Al-0.01Ti-0.08Cu-0.001S-0.008P-0.002B*	MA	968ºC/3.5 h, AC			x		
Davis Besse M3935	Service CRDM	Ni-15.6Cr-6.3Fe-0.03C-0.27Mn-0.37Si-0.01Cu-0.002S-0.004P-69 appm B*	MA	871-927°C	x	x			
GE 93510	CRDM tube	Ni-15.4Cr-8.9Fe-0.05C-0.23Mn-0.30Si-0.19Al-0.34Ti-0.01Cu-0.002S-0.005P-88 appm B*	MA	Not available	x	x			
WNP5	Service CRDM	Ni-16.5Cr-6.0Fe-0.03C-0.28Mn-0.35Si-0.18Al-0.25Ti-0.01Cu-<0.001S-<0.005P-140 appm B*	MA	Not available			o	x	o
			SA	1100ºC/0.5 h, WQ				x	
			SA+TT	above + 704ºC/12 h, AC				o	

*The B content is measured by glow discharge mass spectrometry (GDMS).

** x – completed tests; o – ongoing tests as of August 2020.

Table 4. Baseline microstructure and mechanical properties of the Alloy 600 heats investigated in this study.

Source and Heat ID	Heat Treatments	Carbide Distribution	Grain Size	15%CF Yield Stress at 360°C (MPa)	15%CF Hardness (HV)
GE 31907	SA	No IG precipitates	duplex: ~50–200 μm	357	200±16
Rolls Royce 11415	SA	No IG precipitates	duplex: ~100–500 μm	416	222±13
PNNL NX6106XK-11	MA	TG carbides along ghost GBs and non-uniform distribution of IG carbides; banded TG carbides are also visible.	average grain size 65 μm, with occasional elongated large grains up to ~1 mm long along processing direction	548	251±9
	SA	Negligibly low IG carbide coverage, banded distribution of TG carbides	100–300 μm	468	242±13
	SA+TT	Semi-continuous IG carbides of 100–500 nm in size with sub-μm rod-shape TG carbides mostly close to GBs	100–300 μm	531	261±16
KAPL 33375-2B	MA	Semi-continuous IG carbides of 100–800 nm in size with sub-μm rod-shape TG carbides	average grain size of ~100 μm	551	250±16
ATI 522068	MA	Semi-continuous IG carbides of 0.5–3 μm in size with sporadic fine TG carbides of similar sizes	average grain size of ~150 μm	473	242±15
Davis Besse M3935	MA	Semi-continuous IG carbides	duplex grain size of ~150–500 μm	420*	N/A
GE 93510	MA	Primarily TG carbides	average grain size of ~20-25 μm	740*	N/A
WNP5	MA	Low coverage of IG carbides of ~100–500 nm in size; low density of TG carbides usually appear in isolated streaks	10–50 μm	506	244±9
	SA	No observable IG and TG carbides, intragranular TiN precipitates visible	average grain size of ~300 μm	391	220±14
	SA+TT	Semi-continuous IG carbides of 100–500 nm in size with a few-nm sized TG carbides dispersed in the matrix	average grain size of ~300 μm	445	230±18

*YS measured in 20%CTS condition for Davis Besse M3935, and in 18%CTS condition for GE 93510.

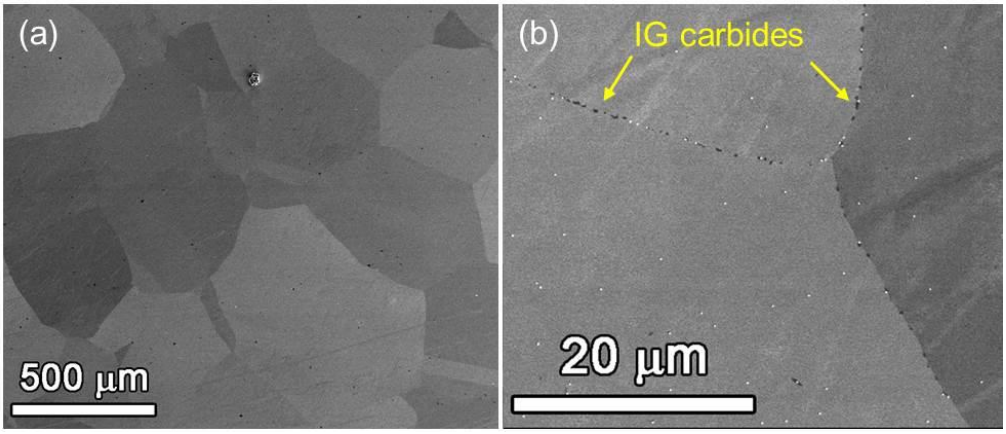

Figure 13. SEM-BSE images illustrating (a) the general microstructure and large grain size and (b) the uniform distribution of IG carbides in the Alloy 600MA service CRDM heat M3935.

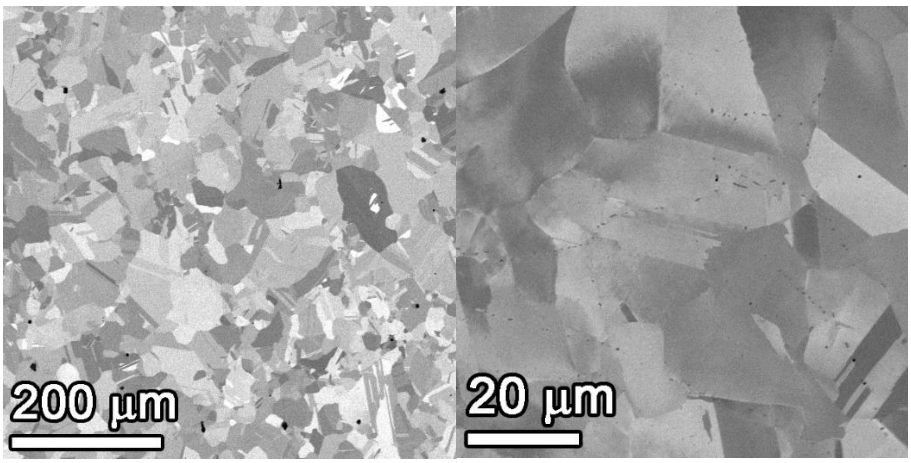

Figure 14. SEM-BSE images illustrating the microstructure of the Alloy 600MA CRDM tube heat 93510 and the TG nature of the carbides.

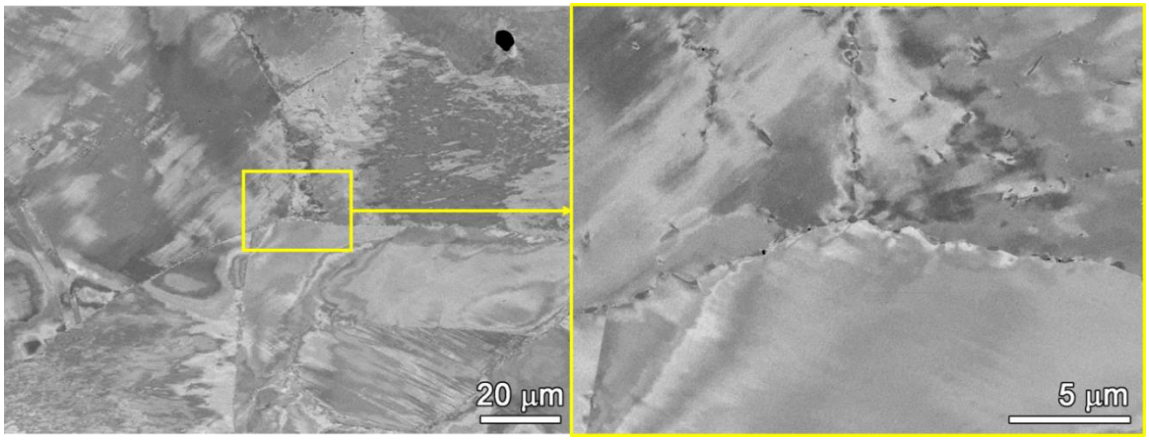

Figure 15. SEM-BSE images illustrating the microstructure of the Alloy 600MA plate heat 33375-2B.

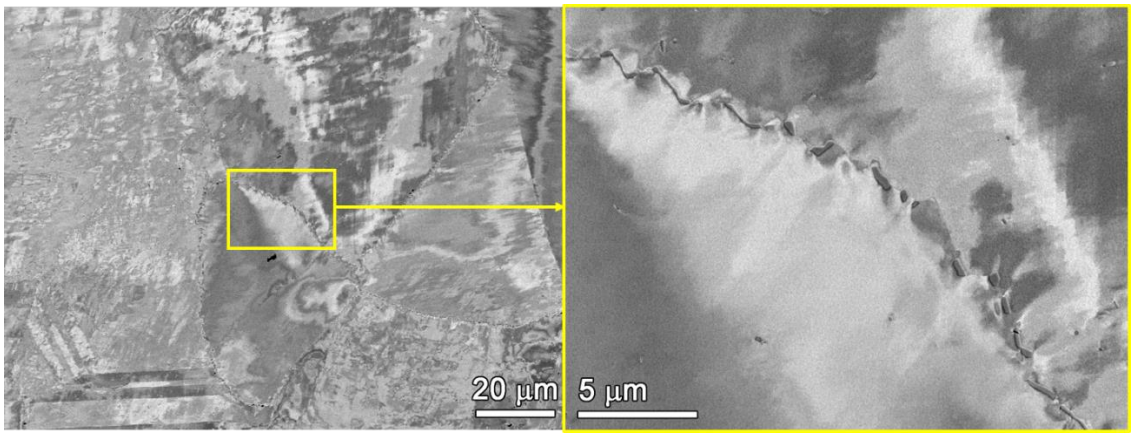

Figure 16. SEM-BSE images illustrating the microstructure of the Alloy 600MA plate heat 522068.

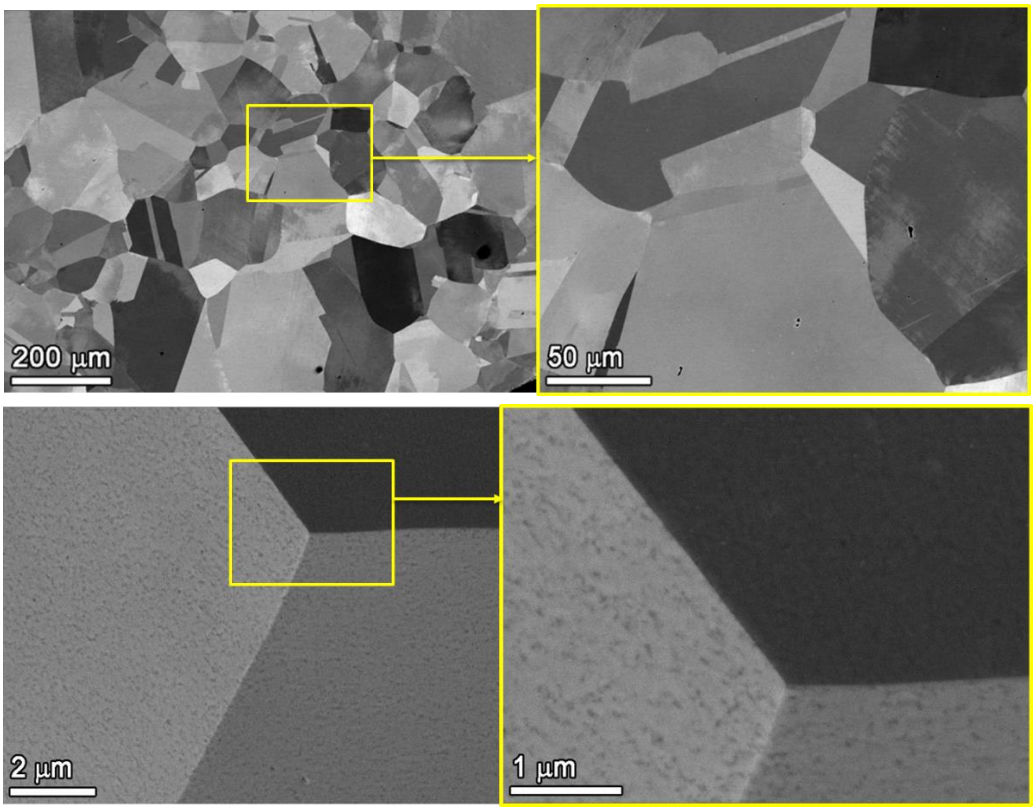

Figure 17. SEM-BSE images of grain size distribution (top) in the Alloy 600SA plate heat 31907 (Foroni) material and higher-magnification images of a grain boundary (bottom) revealing no apparent IG precipitation.

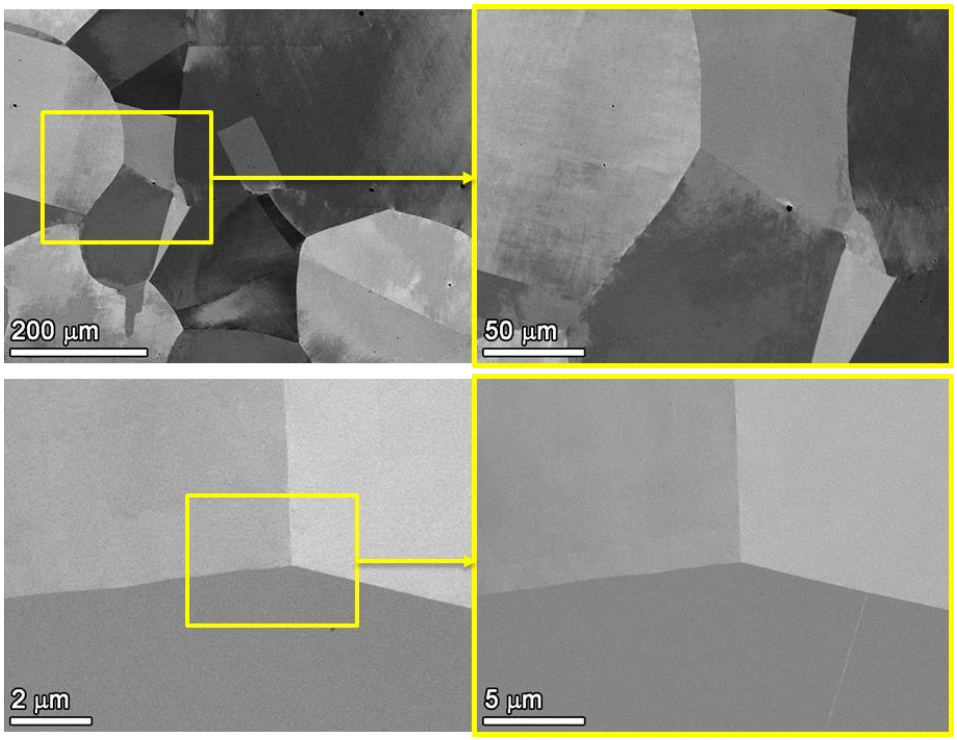

Figure 18. SEM-BSE images of grain size distribution (top) in the Alloy 600SA plate heat 11415 (Rolls Royce) material and higher-magnification images of a grain boundary (bottom) revealing no IG precipitation.

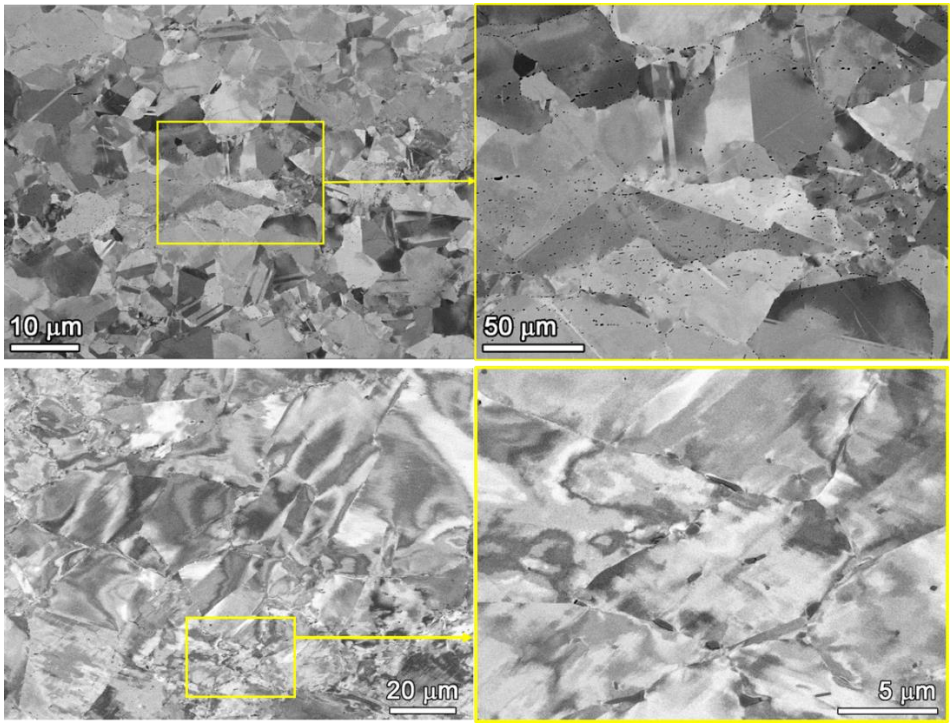

Figure 19. Representative SEM-BSE images of the grain size and carbide distribution in the 15%CF Alloy 600MA plate heat NX6106XK-11.

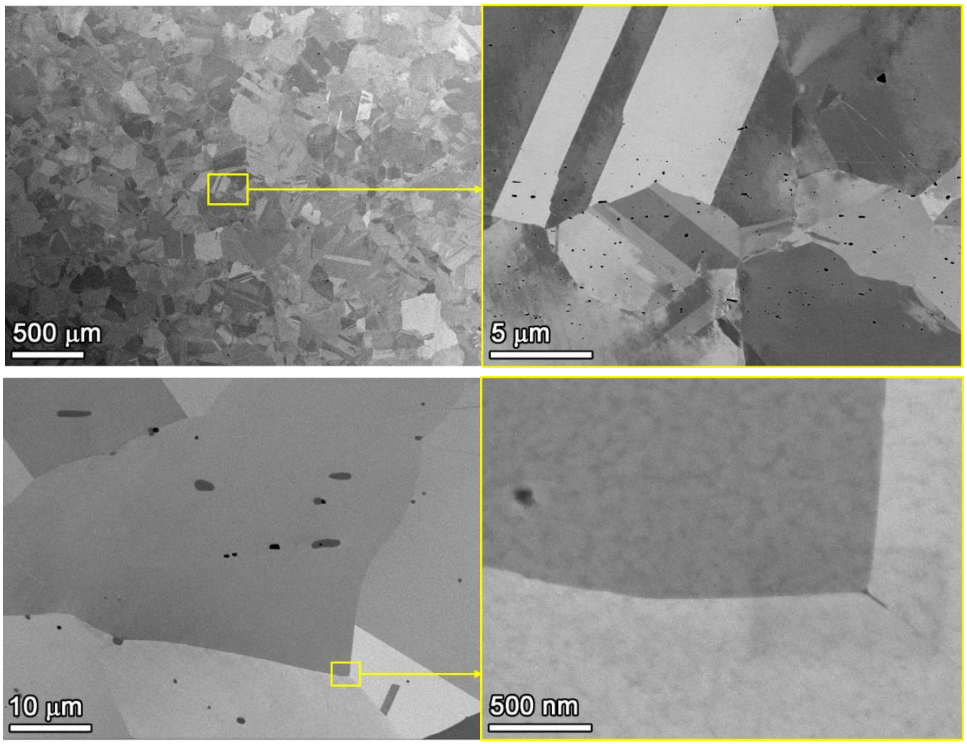

Figure 20. Representative SEM-BSE images of the grain size and carbide distribution in the 15%CF Alloy 600SA plate heat NX6106XK-11.

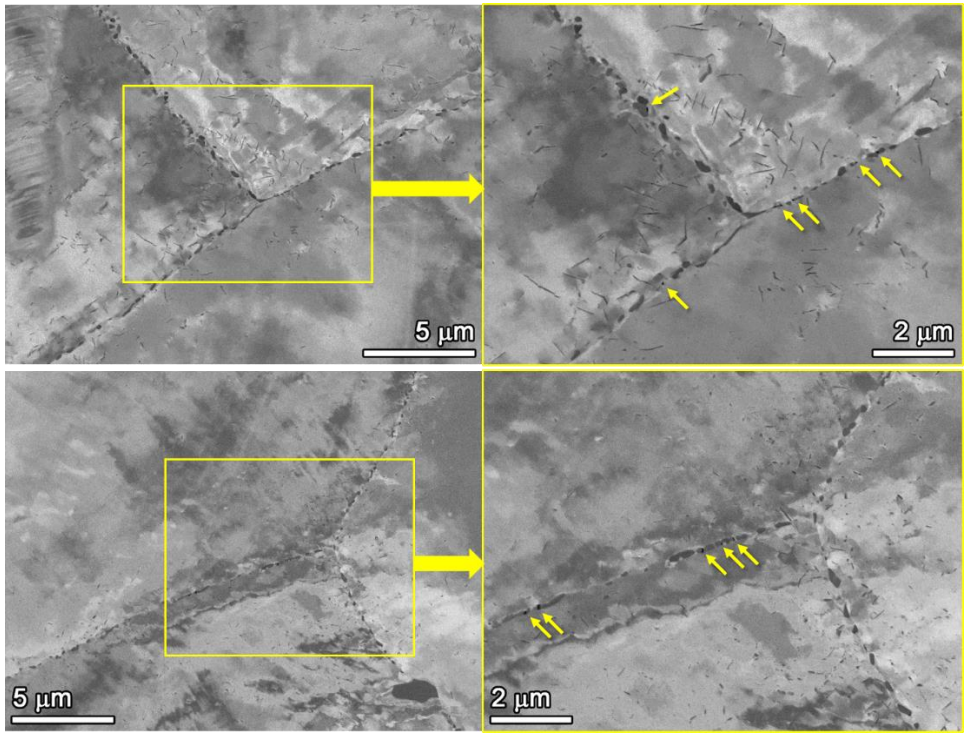

Figure 21. Representative SEM-BSE images of the GB carbides coverage in the 15%CF Alloy 600TT heat NX6106XK-11 material prior to testing. Arrowed features are cavities at carbide-matrix interface or cracks inside carbides produced by cold forging.

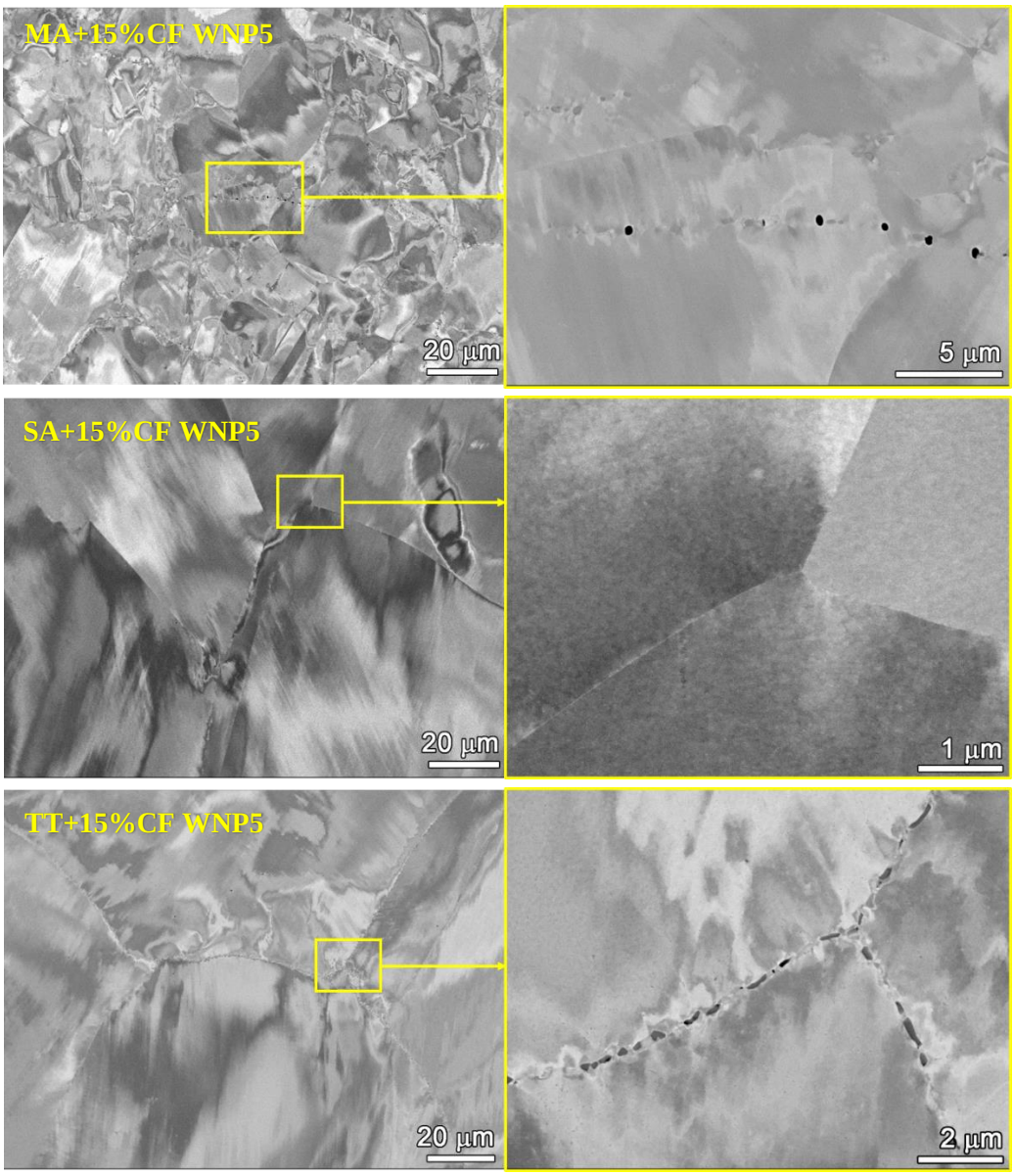

Figure 22. Representative SEM-BSE images of the grain size and carbide distribution in the 15%CF Alloy 600 plate heat WNP5 in the MA (upper), SA (middle), and TT (lower) condition.

Quantification of DCPD-Indicated SCC Initiation

A variety of definitions have been proposed for "SCC initiation" ranging from microscopically small cracks that are usually less than one grain diameter to larger ones that can be detected by non-destructive examination (typically >1 mm long) [32]. In this study, SCC initiation has been based on in-situ DCPD response combined with insights from microstructural characterizations. As mentioned in the Experimental Methods section, while creep and cracking are both likely to be simultaneously contributing to the measured DCPD signal, the SCC initiation time is determined as any obvious increase in strain rate occurs in the referenced DCPD strain response. Figure 23 illustrates representative referenced DCPD strain responses of both non-CW and CW materials using one Alloy 600MA plate heat as an example. As shown in Figure 23a, a significant change in DCPD strain rate by a factor of 3 occurred in the 8%CTS specimen IN052 from the NX6106XK-11 heat in the MA condition after 1250 hours of exposure. In comparison, the non-CW specimens IN014 and IN015 from the same material showed a very gradual increase in slope (25-50%) at exposure times ~6X longer than that for the 8%CTS IN052 specimen (Figure 23b). Another non-CW specimen IN013 from the same material exhibited a small jump in DCPD-measured strain as illustrated in Figure 23c where a 0.08% jump in strain was observed at 5942 hours. The DCPD record revealed that this jump took place within ~105 s, suggesting a relatively rapid change. Interestingly after the detection of this strain jump, the DCPD strain rate remained similar to the value prior to the jump. This suggests that the crack evolution after the strain jump had not altered appreciably therefore the specimen was considered non-initiated.

(a)

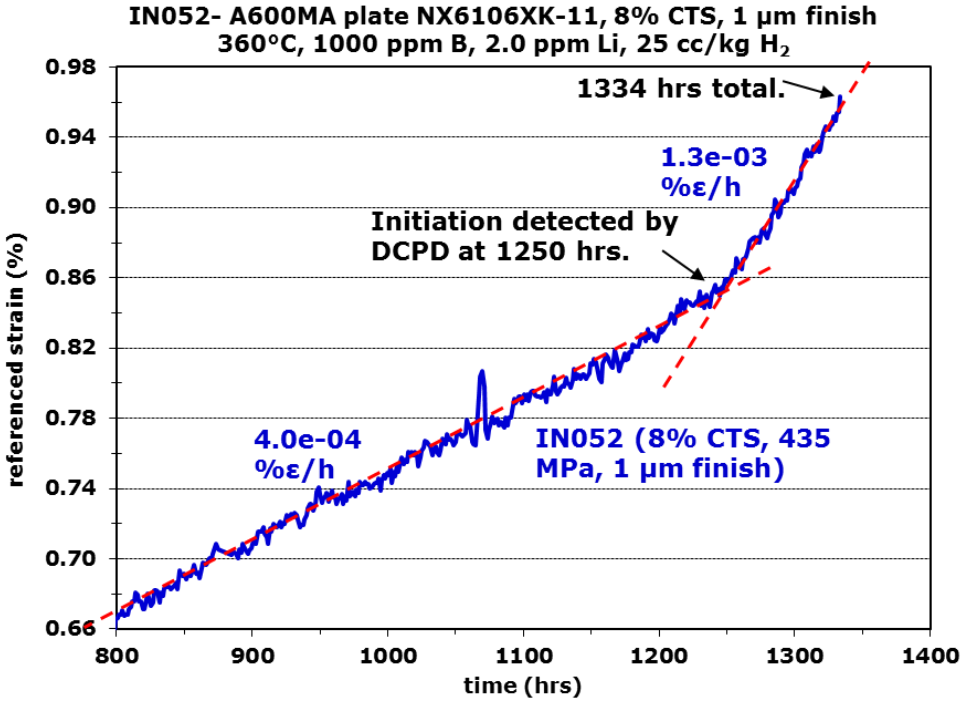

(b)

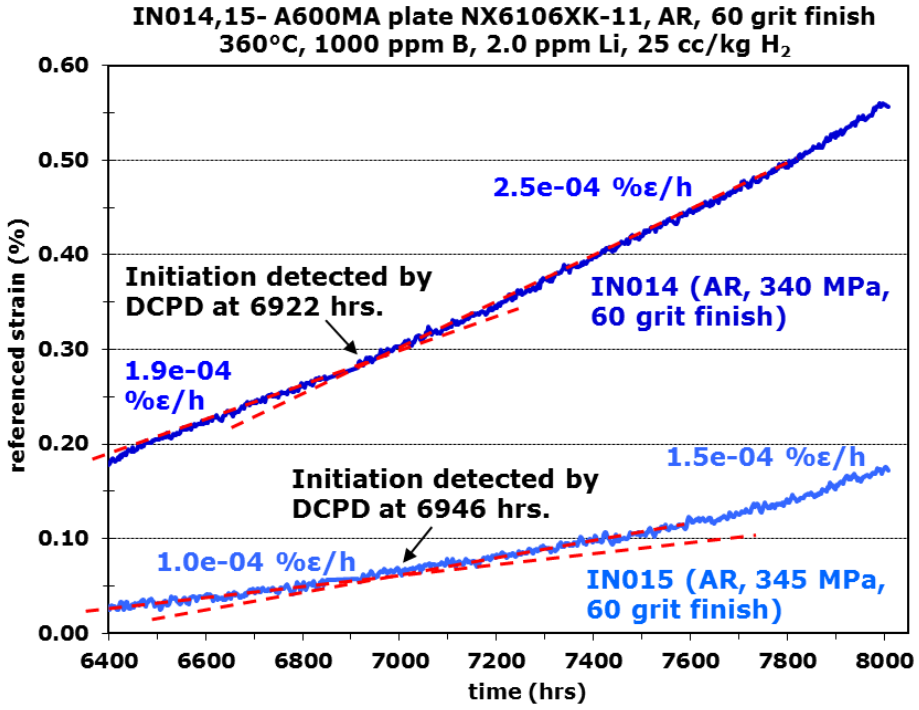

(c)

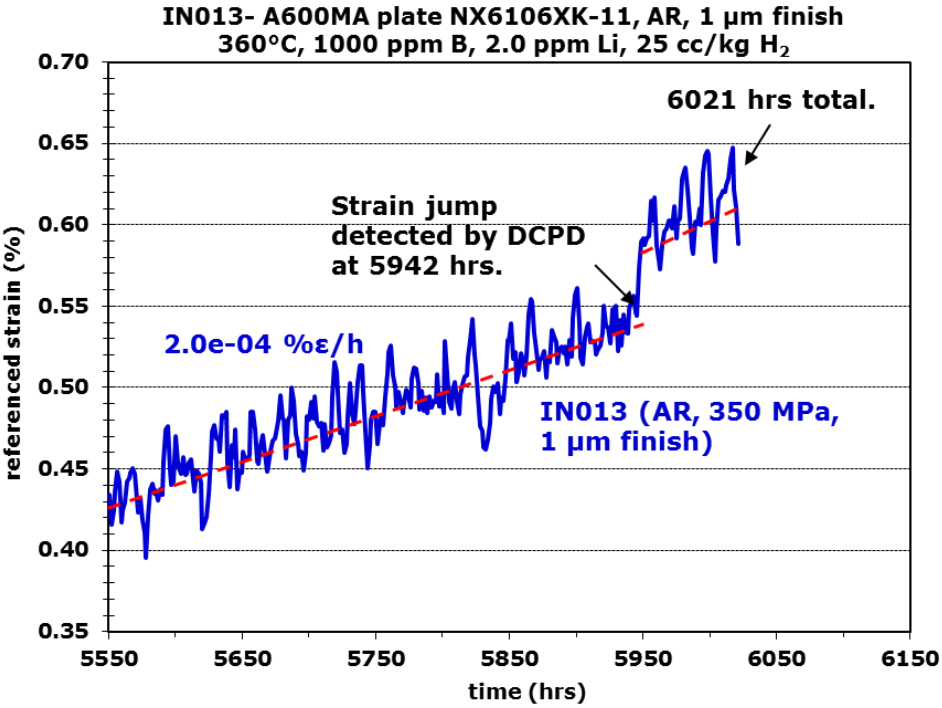

Figure 23. Referenced DCPD strain response for four specimens from the Alloy 600MA plate heat NX6106XK-11 tested at their yield stress: (a) IN052 - an 8%CTS specimen with 1 µm finish, (b) IN014 & 15 - two non-CW specimens with 60 grit finish, and (c) IN013 - a non-CW specimen with 1 µm finish.

To better understand the detectability of DCPD and the difference in SCC initiation behavior between non-CW and CW materials, tests were usually stopped soon after the change in DCPD response occurred and detailed SEM examinations were conducted on all specimens starting with surface morphology documentation. In Figure 24, the SEM surface examination results are shown side-by-side for IN013

(non-CW) and IN052 (8% CW) from the same Alloy 600 plate material at the same scale with opened cracks highlighted in red. Note that the gauge diameter of IN052 is smaller because it was loaded at a yield stress that is higher than for IN013. Large cracks with a surface length extending 100s of micrometers were found in both specimens, but a significant higher density was observed in the non-CW specimen IN013 partly due to its longer exposure time. A zoom-in on the surface revealed that beside opened cracks, extensive shallow grooves delineated GBs in both specimens, indicating that substantial IGA had occurred. Similar phenomenon was observed in non-CW and CW specimens from other heats. Based on these findings, it was concluded that DCPD is not sufficiently sensitive to detect this precursor damage evolution for the current specimen design. For DCPD to detect initiation, the cracking component of the signal must be discernable above the component due to creep. This can be accomplished in two ways. The first is that the increase in DCPD voltage due to a unit change in crack length would have to be very large. A slow growing crack with this attribute would be readily detected above the creep signal. Alternatively, if the increase in DCPD voltage due to a unit change in crack length is small, then crack growth would have to be rapid enough to cause a sufficient increase in the signal to be detectable above creep. Since the microstructural investigations show that extensive crack nucleation and short crack growth occurred before initiation was detected by DCPD, it is thought that this latter scenario best describes what is taking place during the current tests and that the crack growth rate has to be sufficiently high before it can be detected.

Efforts were also made to identify the critical crack geometry at the time when SCC initiation was detected by DCPD. This was achieved through iterative polishing the cross-sections of selected specimens to intersect as many cracks as possible, preferably including the largest/longest ones identified from SEM surface examination. A thin layer (<200 μm) of material was removed during each polish, followed by SEM examination to document depth of all cracks in the cross-sections and the location where the cross-section planes intersect the specimen surface (Figure 25a and b). This enabled reconstruction of depth profile for long cracks along its extension on the surface as illustrated in Figure 25c, where the red solid line represents the crack depth measured after each serial polish, while the dashed line illustrates the hypothetical crack shape created by correlating the measurements of crack length on the surface and crack depth in the cross-section after each polish. In Figure 26, profile reconstruction of the largest cracks that were intersected multiple times during iterative polish is provided with regard to their locations in the gauge section in four specimens from two different Alloy 600MA heats. This include one non-CW and one CW specimen from each material and an illustration of the distribution of large cracks in these specimens were presented at the same scale, facilitating a direct comparison on crack density and size among the specimens. It is obvious that for both heats, large cracks were fewer in density in the CW specimens, but generally exhibiting a higher aspect ratio than those observed in the non-CW specimens. This difference between non-CW and CW specimens will be discussed in more detail in a later section. By comparing Figure 24 and Figure 26, it is obvious that while only a handful of large cracks are present in each specimen that can be intersected ≥3 times during iterative polish for establishing a shape profile, a lot more shorter cracks were encountered once or twice during this process and their depth revealed in the cross-sections were also measured each time. Figure 27 represents the maximum depth measured for all cracks as a function of their surface length for one CW and two non-CW specimens from two different Alloy 600MA heats. It turns out there seem to be a “critical crack size” beyond which the crack aspect ratio starts to differ drastically between specimens in which SCC initiation was detected by DCPD as compared to those that were not. For the initiated specimens, cracks had grown much deeper in depth after reaching the critical size, whereas for non-initiated specimens, cracks tended to extend longer on the surface but without significant growth in depth. Since these specimens have different gauge diameters, the maximum crack depth vs. length distribution was also normalized to get rid of the impact of this variable and the result is presented in Figure 28. Interestingly, it revealed that even though these two heats differ in microstructures and mechanical properties (Table 4), they actually share very similar critical crack size relative to the gauge diameter, i.e. a crack with an aspect ratio of ~0.8 reaching a depth of 4% of the specimen gauge diameter, at which faster crack growth begin to take place. As a result, it seems reasonable to consider that the DCPD detection of SCC initiation is associated with one or a few cracks in

the specimen reaching a critical size, triggering the onset of faster and continuing propagation. This is denoted as “practical SCC initiation” and will be used hereafter to refer to the SCC initiation detected by DCPD in this study.

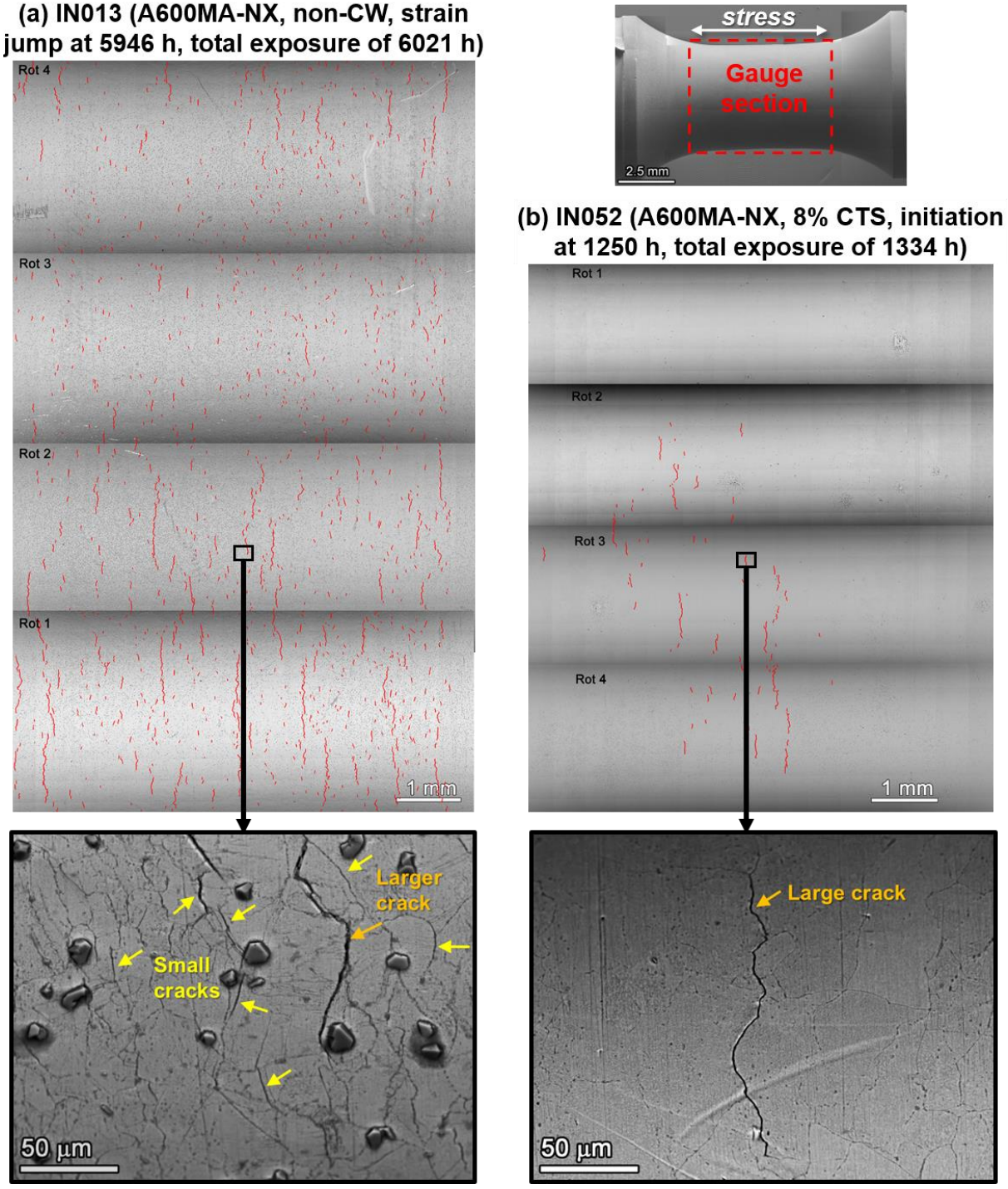

Figure 24. SEM-BSE montage imaging (upper) of the surface morphology of the non-CW and CW specimens from A600MA-NX heat after DCPD change was detected (as shown in Figure 23a and c). Obvious, opened cracks are highlighted in red. A high-magnification SEM-BSE image of a randomly selected site (lower) is also shown for each specimen, revealing most HAGB were affected by IGA.

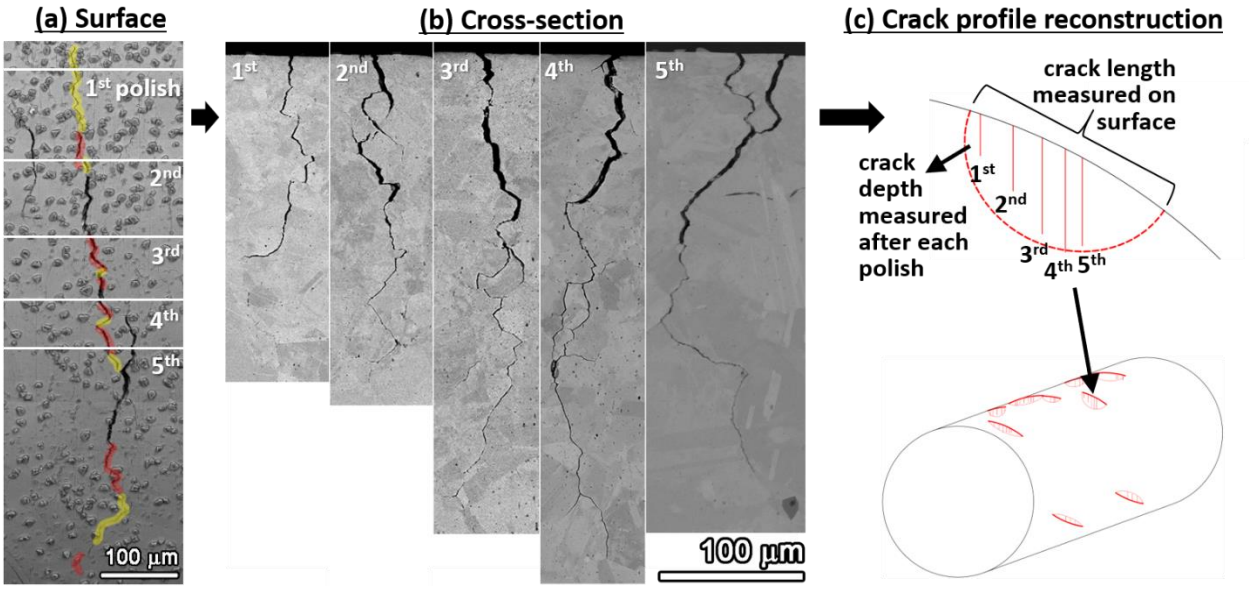

Figure 25. Illustration of steps involved in the reconstruction of a crack profile.

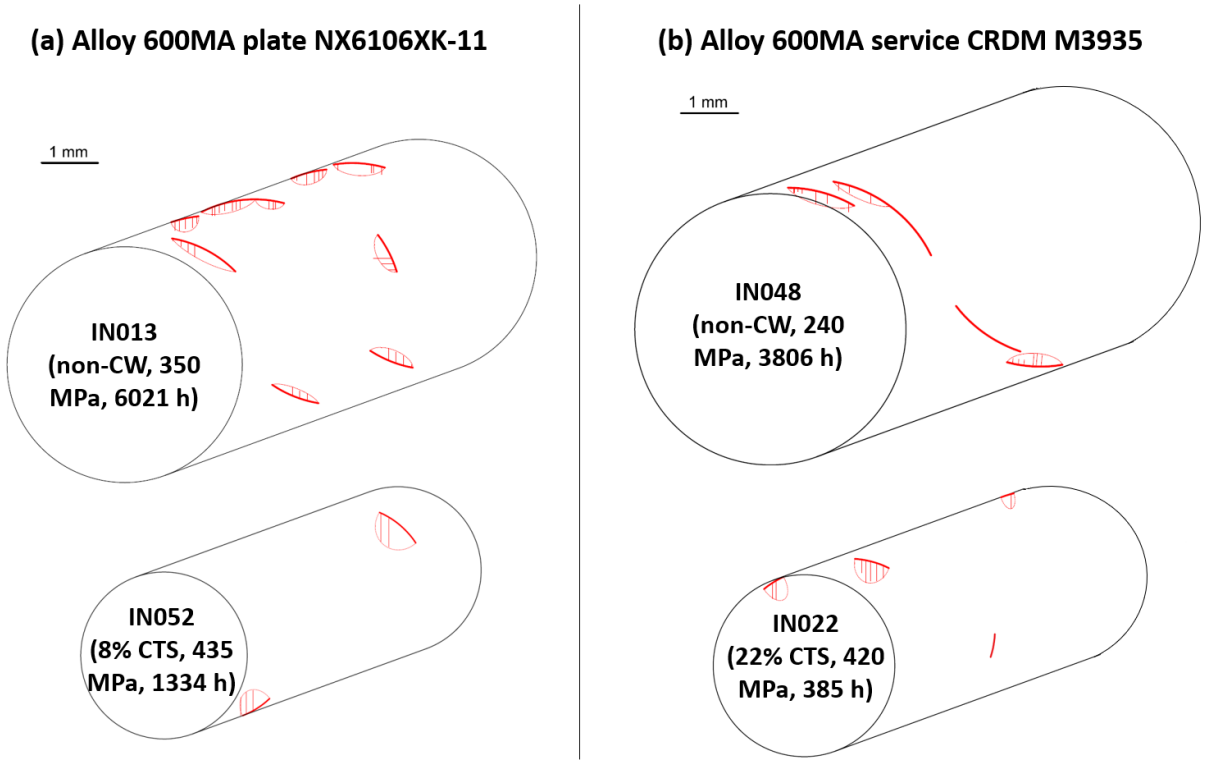

Figure 26. Depth profile of long cracks measured through iterative polish in a non-CW and a CW specimen from (a) Alloy 600MA plate NX6106XK-11 heat and (b) Alloy 600MA service CRDM M3935 heat.

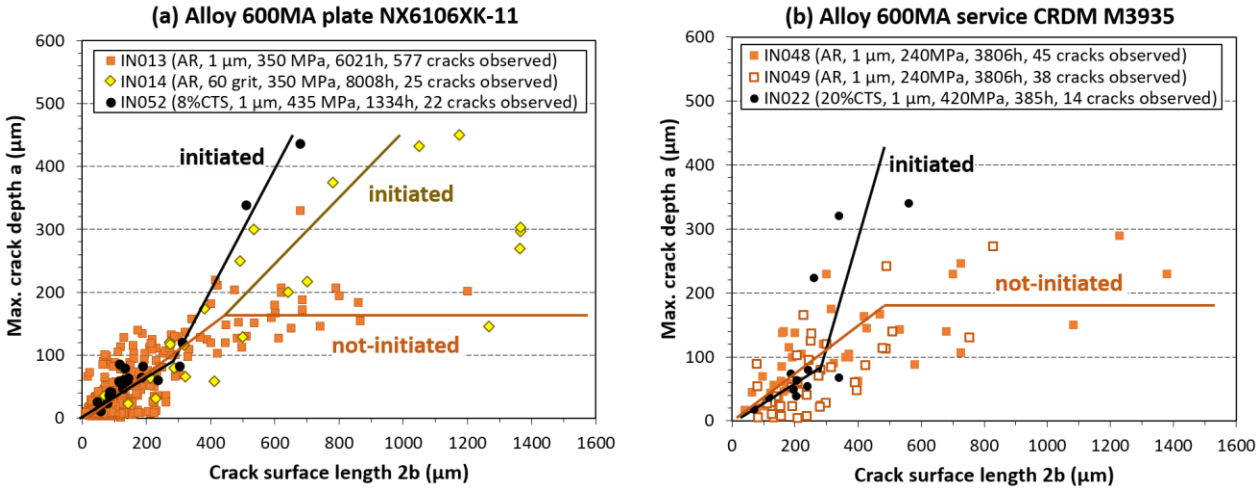

Figure 27. The maximum depth *a* of all measured cracks as a function of their surface length *b* in two non-CW and one CW specimens from (a) Alloy 600MA plate NX6106XK-11 heat and (b) Alloy 600MA service CRDM M3935 heat.

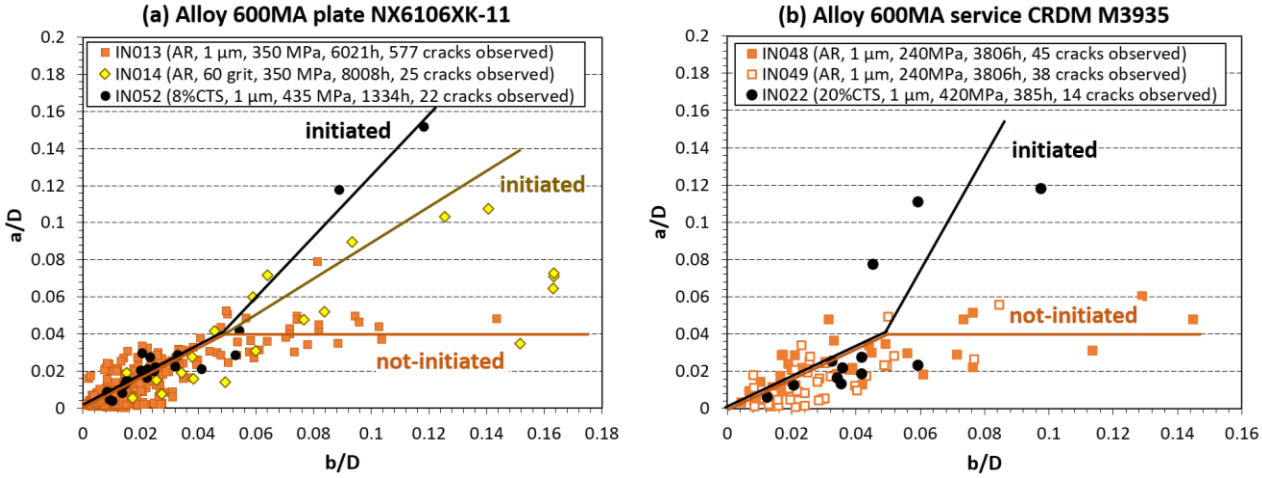

Figure 28. The normalized maximum depth *a/D* of all measured cracks as a function of their ½ surface length *b/D* (*D* is the specimen gauge diameter) in two non-CW and one CW specimens from (a) Alloy 600MA plate NX6106XK-11 heat and (b) Alloy 600MA service CRDM M3935 heat.

Key Steps Leading to Practical SCC Initiation

As mentioned in the previous section, a common feature to all the highly polished Alloy 600 materials that have been examined is for extensive IGA to form on high-angle grain boundaries (HAGB) intersecting the surface irrespective of the loading direction, leading to a darker contrast found delineating the HAGBs under high keV SEM-BSE imaging on specimen surface. Short cracks featuring obvious opening were also observed on the surface, but to a much less density as compared to IGA (Figure 24). To have a better understanding on the distribution and morphology of these precursors, destructive examinations were performed on cross-sections of SCC initiation specimens from various material conditions. Data presented in Figure 29 is the cumulative distribution of the depth of IGA and cracks collected from three different Alloy 600MA heats, each containing one non-CW (closed symbol) and one CW (open symbol) specimen. To ensure representativeness of the data, the measurement was performed on every HAGB intersecting the surface in the 4 mm long gauge in each specimen. The total number of

measured HAGB range from ~40 to 230 depending on the grain size of the material. Note that SCC initiation was only detected in the CW specimen of each heat by the time of the examination specified in the figure. The overall trend revealed is that most of the IG damage remained shallow in all specimens, with more than 90% confined within 5 μm in the CW specimens and 12 μm in the non-CW specimens. Figure 30 presents the deepest IGA and the shortest crack observed during the cross-section examination for the six specimens. Examples of the morphology of relatively long IGA and very short cracks in non-CW and CW samples were also provided in Figure 31 and Figure 32, respectively. In most specimens, the depth of the deepest IGA is similar or slightly longer than the depth of the shortest crack, which suggests a critical depth exists for IGAs to convert to short cracks. By correlating Figure 29 to Figure 30, it is revealed that there seems to be a turning point around the maximum depth of IGA (denoted as D_1 hereafter) beyond which the increase in cumulative percentage starts to drop dramatically with wider extension in crack length. This indicates that once IGA become cracks, the growing rate begins to pick up and eventually leads to formation of large cracks that can trigger DCPD detection of SCC initiation. Another noteworthy observation is that the maximum IGA depth is always higher in non-CW specimens at a lower yield/applied stress in comparison to the CW specimens tested at a higher yield/applied stress (Figure 33). Assuming linear elastic fracture mechanics (LEFM) applies to such small crack geometries near the surface, a preliminary calculation of the stress intensity K associated with D_1 in each specimen using FEM results provided in [33] yielded very similar values at ~1.2 MPa√m. This might mark a threshold K where the growth kinetics start to accelerate, possibly associated with a shift from a corrosion dominated growth to a faster growth governed by stress intensity that will be investigated in more details later.

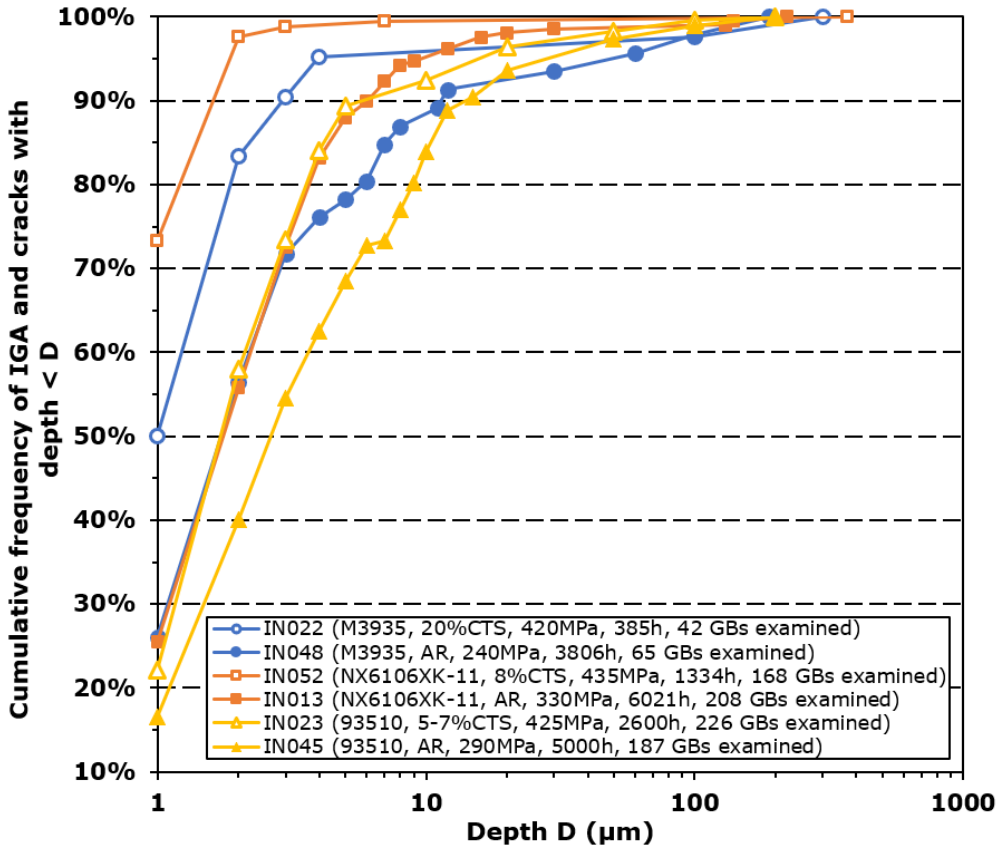

Figure 29. Cumulative distribution of the depth of IGA and cracks measured in one cross-section of 6 SCC initiation specimens from three Alloy 600MA heats on every HAGB intersecting the surface in a length of 4 mm in the gauge section.

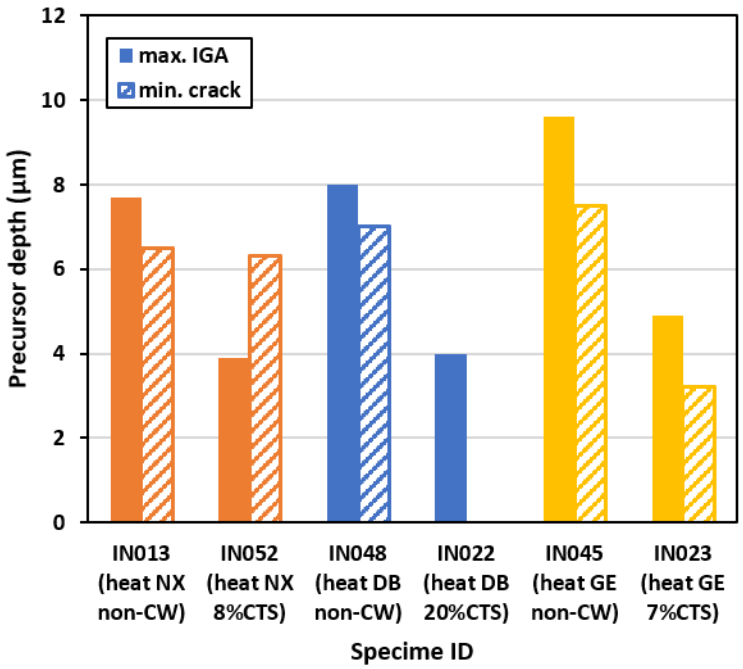

Figure 30. The deepest IGA and shortest crack observed in the cross-section of the six Alloy 600MA specimens shown in Figure 29 during quantification of IG damage depth.

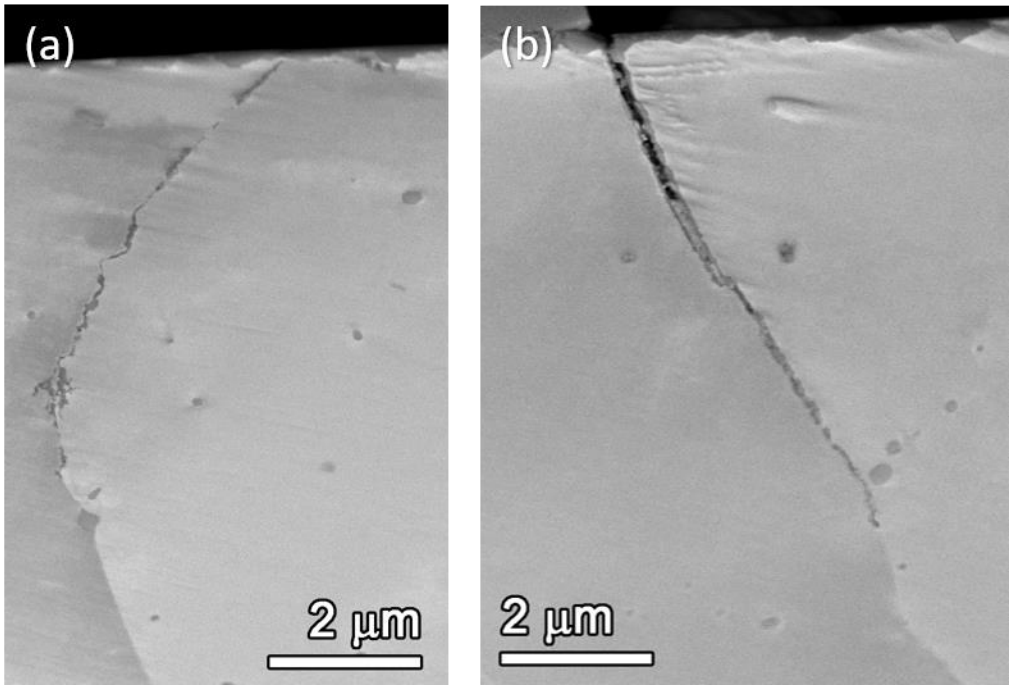

Figure 31. (a) A relatively long IGA and (b) the shortest crack observed in the Alloy 600MA heat 93510 non-CW specimen IN045 after 5,000 hours exposure in 360ºC PWR primary water at material yield stress (290 MPa).

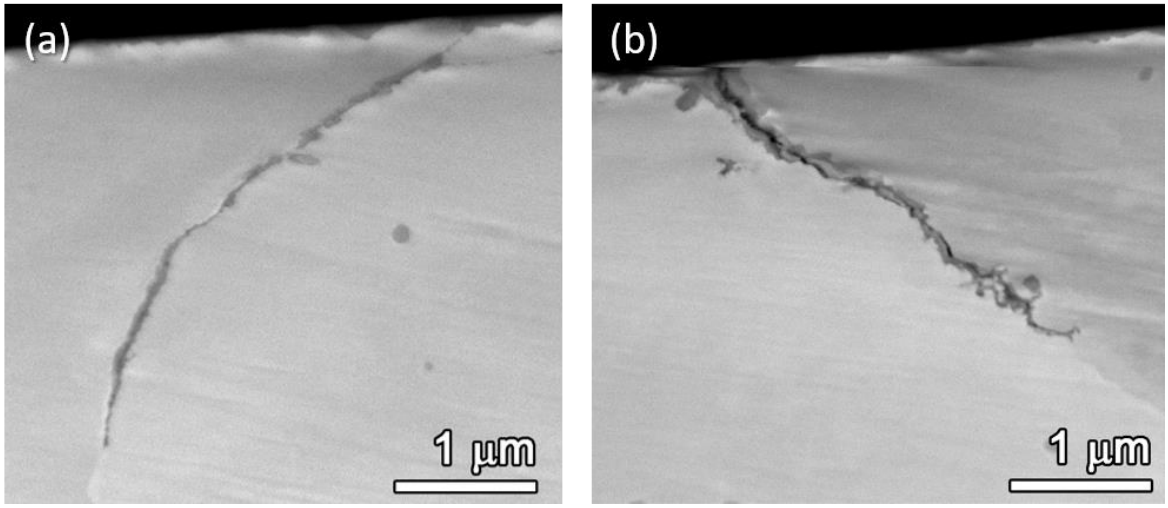

Figure 32. (a) A relatively long IGA and (b) the shortest crack observed in the Alloy 600MA heat 93510 7% CTS specimen IN023 after 2,600 hours exposure in 360ºC PWR primary water at material yield stress (425 MPa).

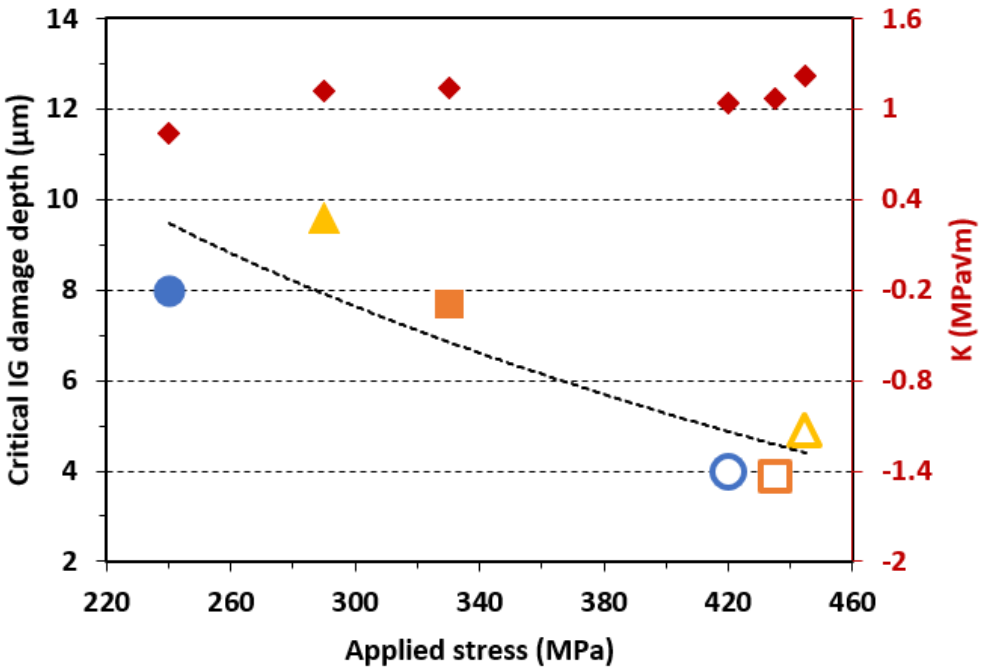

Figure 33. The critical IG damage depth D_1 as a function of the applied stress on the six specimens during test. The estimated stress intensity K associated with D_1 in each specimen is also plotted.

Another common observation by SEM is that long cracks appear to form more often by coalescence of multiple short cracks rather than continued growth of a single crack. This is particularly obvious in non-CW specimens that underwent multiple test interruptions because the specimen surface morphology was documented several times allowing crack evolution to be directly viewed over time (Figure 34). Detailed examinations on highly polished specimen surface revealed that cracks can coalesce in three scenarios:

I. Two coplanar cracks merge into one through shared GBs in between;

II. Two neighboring cracks merge into one with their encountering tips first grow pass, then turn toward each other.

III. Two neighboring cracks merge into one through a bridging GB usually oriented perpendicular to the two parallel cracks.

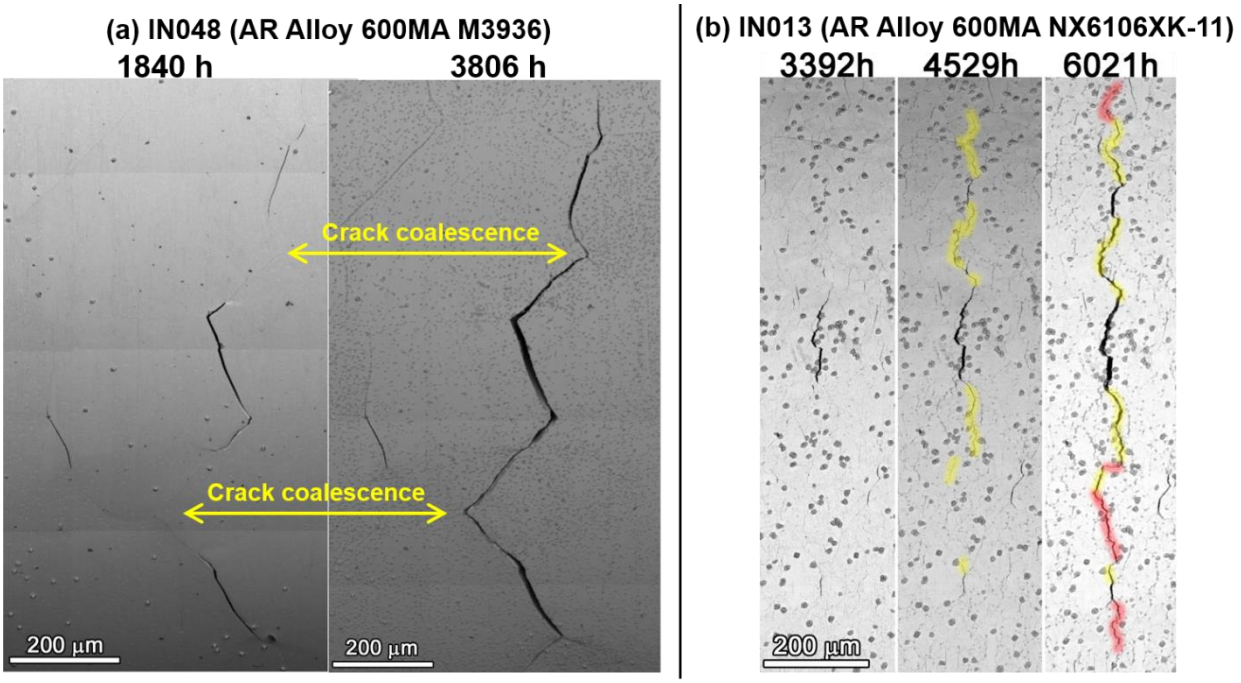

Figure 34. SEM-BSE images of coalescence of multiple cracks observed at the same site with progress in exposure time in the AR, non-CW specimens from two tested heats: (a) IN048 of the CRDM heat M3935 and (b) IN013 of the plate heat NX6106XK-11.

While Scenario I occurs regardless of grain size of the materials as shown in Figure 34, Scenarios II and III prevail in materials with smaller grains, i.e., grain size smaller than the critical crack size specified in Figure 28 needed to trigger faster crack growth. Parkins et al. [34-38] have performed extensive studies on coalescence of SCC cracks in Cr-Mn steels in high pressure gas transmission pipelines. They suggested that coalescence of parallel cracks occur when the distance between crack tips falls within a certain distance, and an empirical crack coalescence criterion was derived based on this notion:

$$h \leq 0.14 \cdot 2\bar{b} \tag{19}$$

where h is the perpendicular distance between two parallel cracks, and $2\bar{b}$ is the mean of the surface length of the two interacting cracks. To examine whether this criterion applies to the Alloy 600 materials in current study, detailed quantification was carried out on two different heats, each containing one non-CW and one CW specimens with highly polished surface. In Figures 35 and 36, the lateral distance h between each interacting crack couples is plotted against the mean of their surface length $2\bar{b}$. It turned out that the straight line separating the coalesced cracks from the uncoalesced ones in all specimens appear to have a slope close to 0.14, which is in accordance with the Parkin's coalescence criterion presented above. [39] also performed SCC coalescence study on two Alloy 600 heats in simulated PWR primary water and reached the same conclusion. The independence of this criterion on material system and environment conditions suggests that it must be mechanics-based. In fact, similar relationship has been derived theoretically under LEFM conditions [35, 40], providing technical justification for using this criterion to assess crack coalescence.

In addition, sequential examinations on specimen surface during interrupted tests also revealed that crack growth can be intermittent due to occurrence of crack coalescence. In addition, dormancy of short

cracks was often observed when other cracks are present in its vicinity beyond the coalescence criterion. This can possibly be attributed to stress shielding effects between cracks and is more evident in non-CW materials exhibiting a high density of shallow, circumferential cracks.

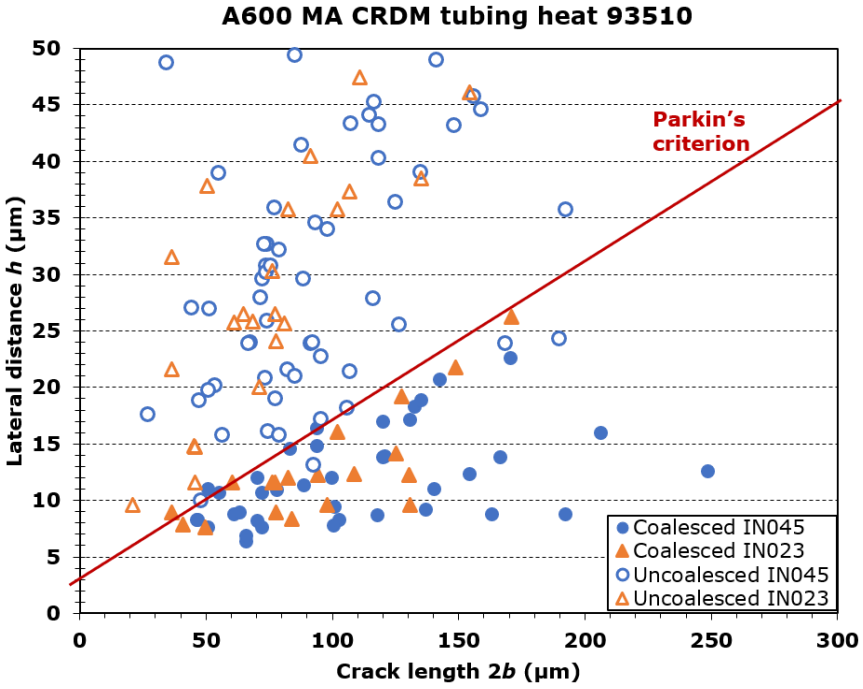

Figure 35. Crack coalescence statistics of the non-CW specimen IN045 and 7%CTS specimen IN023 from the Alloy 600MA CRDM tubing heat 93510 in comparison with Parkin's criterion.

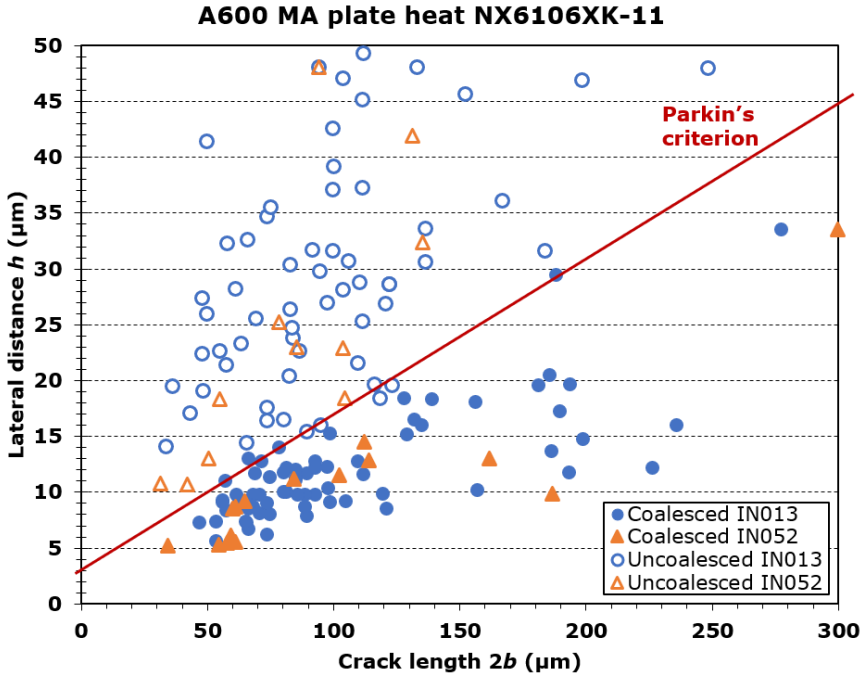

Figure 36. Crack coalescence statistics of the non-CW specimen IN013 and 8%CTS specimen IN052 from the Alloy 600MA plate heat NX6106XK-11 in comparison with Parkin's criterion.

While crack coalescence had complicated the process of formation of large cracks, quantitative analyses demonstrated that the large cracks can be considered as a single crack having a semi-elliptical shape (Figure 26), and that the critical crack size leading to DCPD detection of SCC initiation is independent of material condition (Figures 27 and 28). These observations indicate that the transition to practical SCC initiation is also of mechanical nature. As a result, stress intensity (K) estimation was performed on selected large cracks using finite element modeling (FEM) at PNNL. In addition, an equation has been proposed in literature for estimating K at the crack front of small elliptical cracks in round bars using the following equation:

$$K = F\sigma\sqrt{\pi a} \tag{20}$$

where σ is the applied stress, a is the crack depth, and F is the dimensionless stress intensity factor (SIF), which is dependent on crack size relative to gauge diameter a/D, crack shape in the form of aspect ratio a/b, and the position at the crack front. Values of F as a function of these geometric variables are provided in several published numerical studies [33, 41, 42], allowing quicker estimation of the K at crack front. As shown in Figure 37, a good agreement was found between the SIF values estimated by our FEM analysis and literature data on various geometry of small cracks, suggesting the two methods provide consistent estimations on K, therefore they were both used in our applications for different purposes.

Figure 28 illustrates the K estimated by FEM at the center of the crack front of selected large cracks in three specimens from the MA plate heat NX6106XK-11. Results suggest that in the CW specimen IN052, larger cracks had significantly outpaced the smaller ones with growth rates fast enough to be detected by DCPD at a stress intensity of ~8 MPa√m. In comparison, cracks in the non-CW specimen IN013 at similar K levels did not lead to practical SCC initiation. Comparison of the K levels estimated at large cracks in the non-initiated specimen IN013 and the initiated specimen IN014 seem to suggest that the practical SCC initiation of this heat in non-CW condition seem to be associated with cracks reaching a K of 10–12 MPa√m at the crack front.

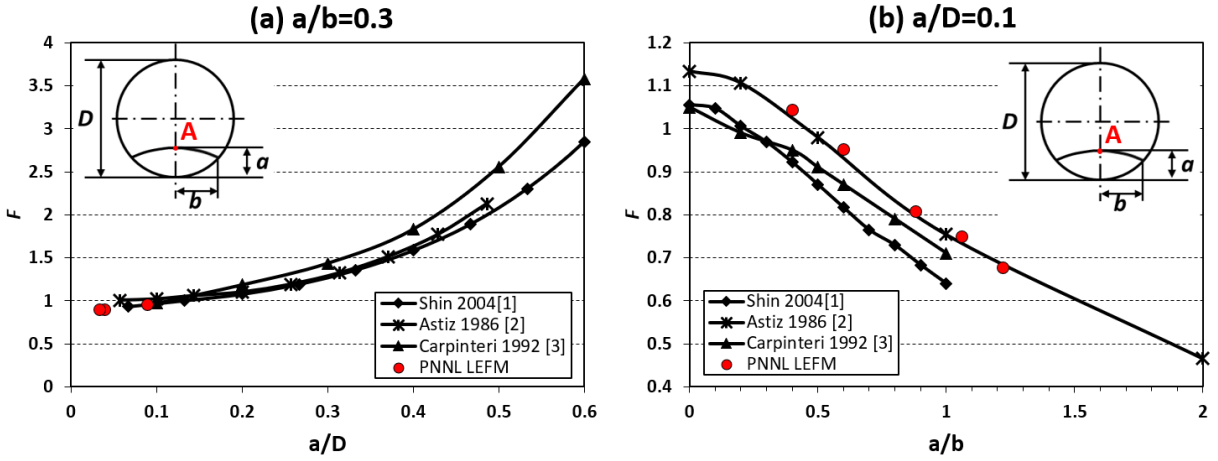

Figure 37. Comparison of the dimensionless SIF (F) values estimated by FEM performed at PNNL with literature at the center of the crack front (point A) of a short semi-elliptical crack with (a) varying values for a/D and a fixed a/b=0.3 and (b) varying values for a/b and a fixed a/D=0.1.

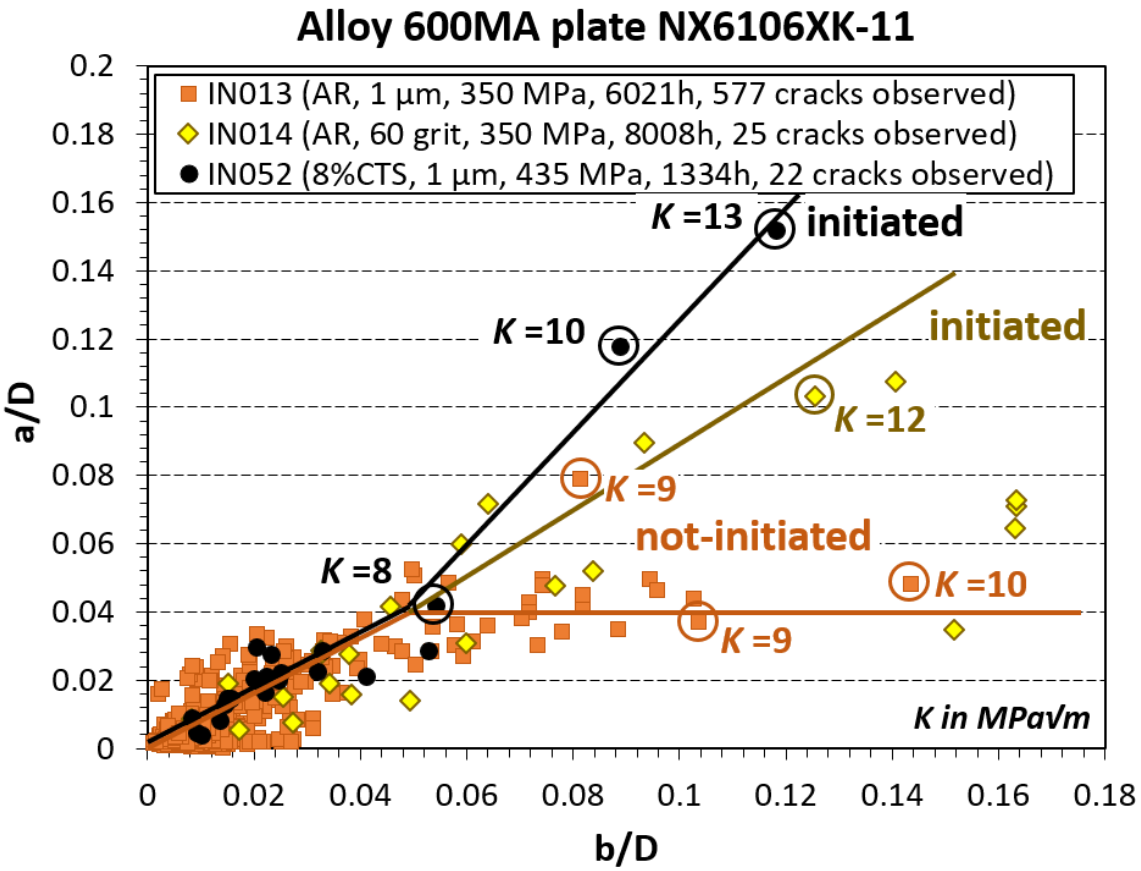

Figure 38. FEM estimation of *K* at the center of the crack front of selected large cracks in the non-CW specimen IN013 (not-initiated) and IN014 (initiated) and the CW specimen IN052 (initiated) from the Alloy 600MA plate heat NX6106XK-11.

In addition, estimates of local *K* have also been made as a function of position along the crack front. Although many numerical studies provided solutions for *F* when crack aspect ratio a/b ≤ 1, Ref. [41] appears to be the only one that considered the situation where a/b > 1, which is the case for the large cracks observed in the two CW specimens. Therefore Ref. [41] was used for this estimation and *K* evolution from the center to the end along the crack front is illustrated in Figure 39. It is shown that for the three non-CW specimens, *K* decreases from the center to the end of the long circumferential cracks. Note that IN013 had a higher *K* predominantly because of the higher applied stress to this specimen. These *K* values are generally below the threshold *K* of 9 MPa√m for SCC growth proposed for MA alloy 600 [43-46] consistent with the fact that no fast growing cracks were observed in these specimens. For the two CW specimens in which SCC initiation have been detected by DCPD, *K* keeps increasing from the center to the end of the large cracks. Results show that the *K* at the center is typically higher than 10 MPa√m and rises up to 15–20 MPa√m at the point where the crack meets the surface. SCC crack growth has a strong dependence on *K* within this range [45], and it is believed that one of the key contributors to the onset of rapidly growing SCC crack is this increase in *K* [9]. On the other hand, it has been reported [47] that a critical aspect ratio $(a/b)_c$ exists for each relative crack depth (a/D), and the dimensionless *K* factor *F* is higher at the crack center when $a/b < (a/b)_c$. However when $a/b > (a/b)_c$, *F* is higher at the crack surface. Combined with the experimental findings of this study, it seems very likely that the transition from short cracks to practical SCC initiation is influenced strongly by a crack reaching a critical shape (both in crack aspect ratio and relative crack depth), so that *K* values sufficient to sustain a faster CGR are produced across the entire crack front.

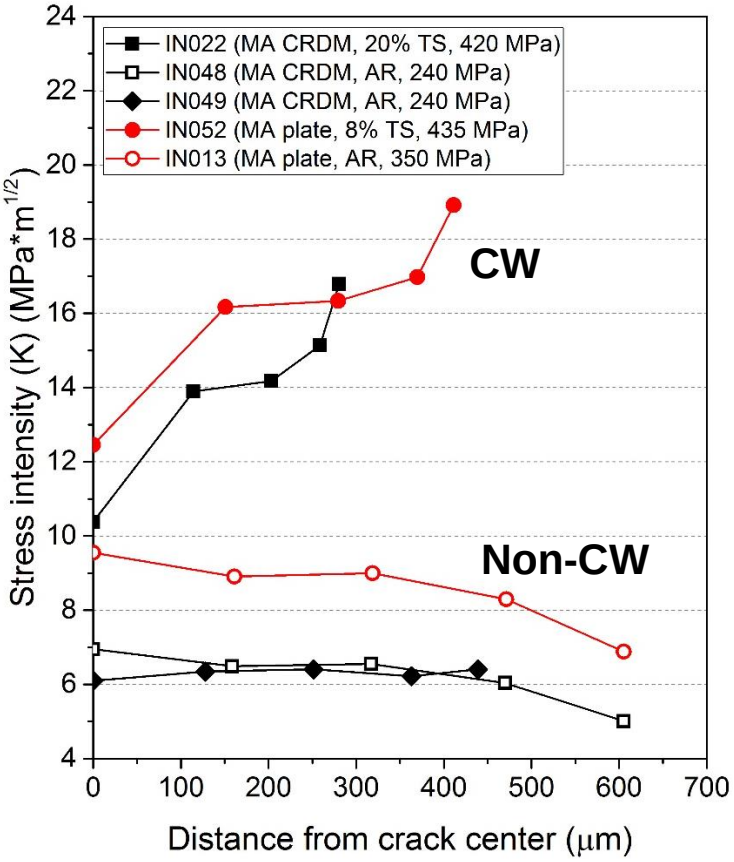

Figure 39. *K* estimated from crack center to crack surface of the largest crack observed in five SCC initiation specimens from two Alloy 600MA heats, among which SCC initiation was only detected by DCPD in the CW specimens IN022 and IN052.

Based on these observations, the "practical" SCC initiation of Alloy 600 in PWR primary water can be categorized into three stages (Figure 40):

(a) IGA and crack nucleation: IGA forms immediately after exposure begins on all HAGBs intersecting the surface with attack depth increasing with time. There seems to exist a critical depth beyond which all IGAs will become opened cracks, triggering a local *K* that starts to promote short crack growth.

(b) Short crack growth and coalescence: this stage features development and growth of short cracks at accelerated rates than IGA, plus coalescence contributing to intermittent crack growth in size and rate. Cold work appears to have a key impact on this stage and has led to different behavior in non-CW vs. CW materials. IGA and coalescence drive the formation of long surface cracks in non-CW material, whereas higher SCC susceptibility of CW material produce cracks that quickly grow deep. Stress intensity *K* at crack front appears to be the dominant factor in controlling crack growth behavior.

(c) Transition to stable crack growth: this is featured by cracks reaching a critical size to produce a *K* for practical SCC initiation and sustained growth at engineering relevant rates. This *K* is lower for more susceptible CW materials than for non-CW materials.

This framework will be used to guide model development for SCC initiation that will be presented later following a summary on the effect of key factors influencing SCC initiation behavior of Alloy 600.

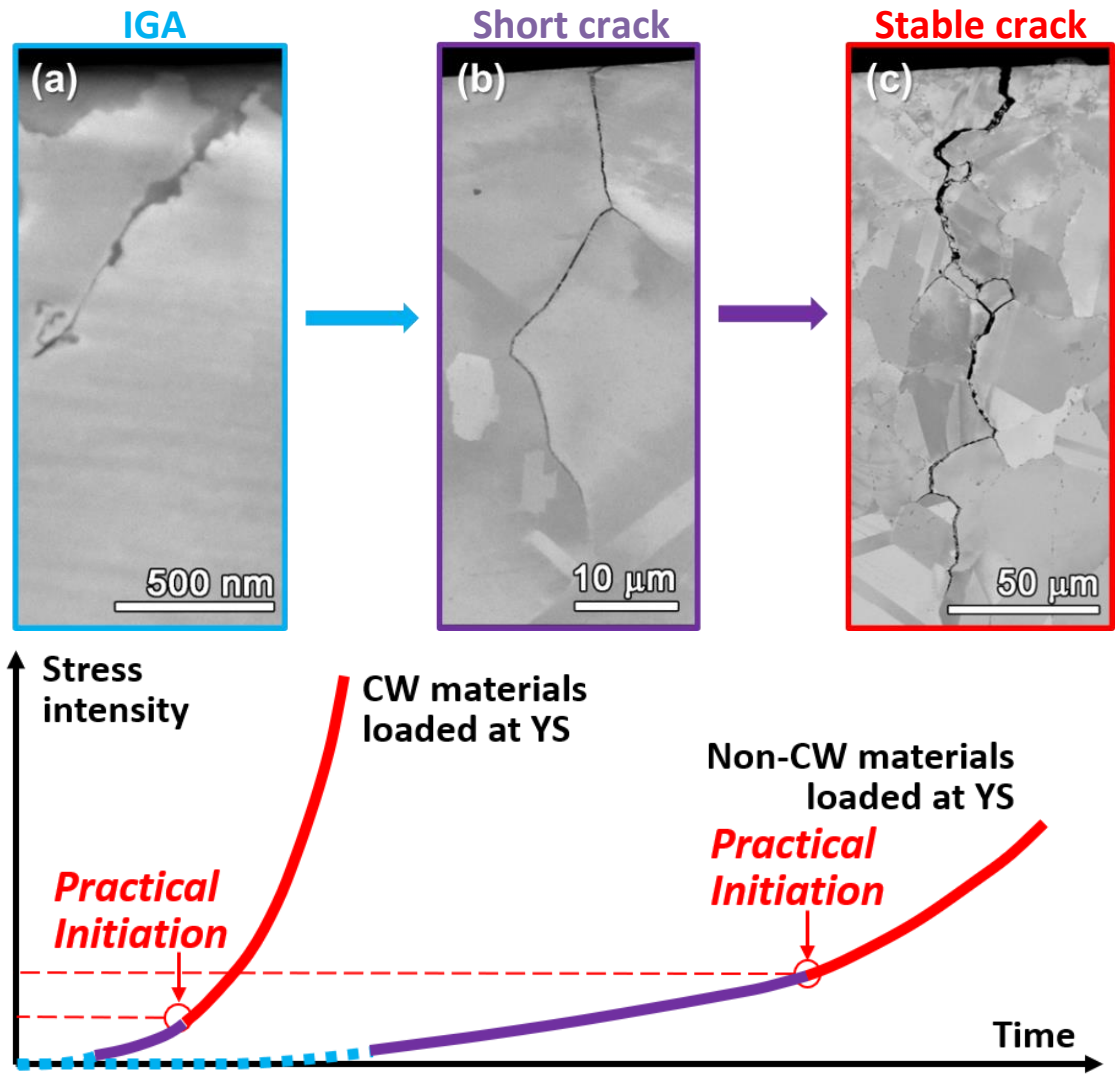

Figure 40. Schematic illustrating the three stages leading to practical SCC initiation in Alloy 600 materials with transition criteria highlighted as a function of stress intensity *K* (note that the IGA stage is plotted in dotted line as *K* is non-existent for uncracked IGAs and the kinetics at this step is not governed by *K*).

Identification of Critical Parameters and Their Role in SCC Initiation

To date, SCC initiation tests have been completed on 81 specimens from eight different Alloy 600 heats with varying material and environmental conditions. DCPD-indicated SCC initiation times were determined for 73 of them, while the remaining 8 specimens were removed before clear indication of SCC initiation for destructive characterizations to obtain complementary insights on the development of SCC precursors. It should be noted that due to the impact of the COVID-19 pandemic, not all testing and characterization activities have been completed as planned. However, combined with the results obtained from complimentary unstressed exposures and low-*K* SCC crack growth tests, sufficient data has been generated to identify critical parameters during IGA development and short crack growth, the two consecutive steps that lead to practical SCC initiation in Alloy 600. Below a summary will be provided on the effects of influencing factors evaluated in this study on Alloy 600 SCC initiation and key trends revealed will be discussed.

Effects of Mechanical Factors on Practical SCC Initiation of Alloy 600

Applied Stress and Cold Work

The relationship between SCC initiation time and applied stress is shown in Figure 41 and for the level of cold work in Figure 42. Dashed lines in the plots are meant to bound the data and aid in visualization of the initiation response. As discussed in the previous section, DCPD detection of SCC initiation is likely associated with reaching a critical crack size relative to specimen gauge diameter that can sustain stable crack growth at engineering relevant rates. Since non-CW and CW specimens from the same material can have a difference up to ~2 mm in gauge diameter in order to allow them to be tested in one load train at yield stress under a fixed load, it will require non-CW specimens to grow ~80 μm deeper in order to have SCC initiation detected by DCPD. Considering crack grows much more slowly in non-CW materials than in CW materials, this additional depth to grow can result in two to four orders of magnitude more hours of exposure before SCC initiation can be detected by DCPD assuming a CGR for large cracks in non-CW materials is in the range of 1×10^{-7} to 1×10^{-9} mm/s. To tackle this potential bias, a revision on the DCPD-detected SCC initiation times was performed by normalizing the initiation times to the average specimen gauge diameter of 3.55 mm. The revised data is also shown in Figures 41b and 42b. While little change in SCC initiation time distribution was observed among the CW specimens because the difference in their gauge diameters is not large, the revision has significantly brought down the SCC initiation times in non-CW materials by ~1000–2000 hours. If not mentioned otherwise, these normalized SCC initiation times will be used hereafter for data analysis to evaluate the effects of factors on SCC initiation in Alloy 600.

In Figure 43, the normalized SCC initiation data is highlighted on the three Alloy 600MA heats that were investigated for the effects of applied stress (Figure 43a) and cold work level (Figure 43b). Whether analyzed as a function of stress or cold work level, the data show a substantial reduction in SCC initiation time between no cold work and low levels of cold work, while higher levels of cold work or stress have caused no or only a small additional reduction. More specifically, materials with a cold work level of 7-8% or more have all initiated in less than 2600 hours, whereas confirmed SCC initiation in non-CW materials only occurred in one non-CW specimen at ~2800 hours for the highly susceptible service CRDM heat M3935 and two non-CW specimens at ~6000 hours for the plate heat NX6106XK-11. The non-CW specimens from the other CRDM tubing heat 93510 did not exhibit SCC initiation after exposure up to ~8000 hours. It is also worth noting that while these results show a strong effect of small amounts of cold work, the concurrent application of higher stress in the CW materials must also be having an effect. To better isolate the effects of applied stress and cold work, additional testing at 90% YS is currently underway in collaboration with a joint NRC-EPRI SCC initiation program at PNNL on two Alloy 600MA heats that have already been tested at 100%YS. These tests have been significantly delayed by the COVID-19 pandemic and results will be reported in the future.

Meanwhile, Figure 44 offers an alternative way to interpret the combined effect of applied stress and cold work by plotting the SCC initiation times as a function of the stress ratio in the form of applied stress vs. yield stress in non-CW condition. It appears that a better fit with data was obtained when using the stress ratio, indicating a strong link between SCC initiation behavior and baseline, non-CW material microstructure for Alloy 600. This finding will be considered in modeling SCC initiation of Alloy 600 materials that will be detailed in later sections.

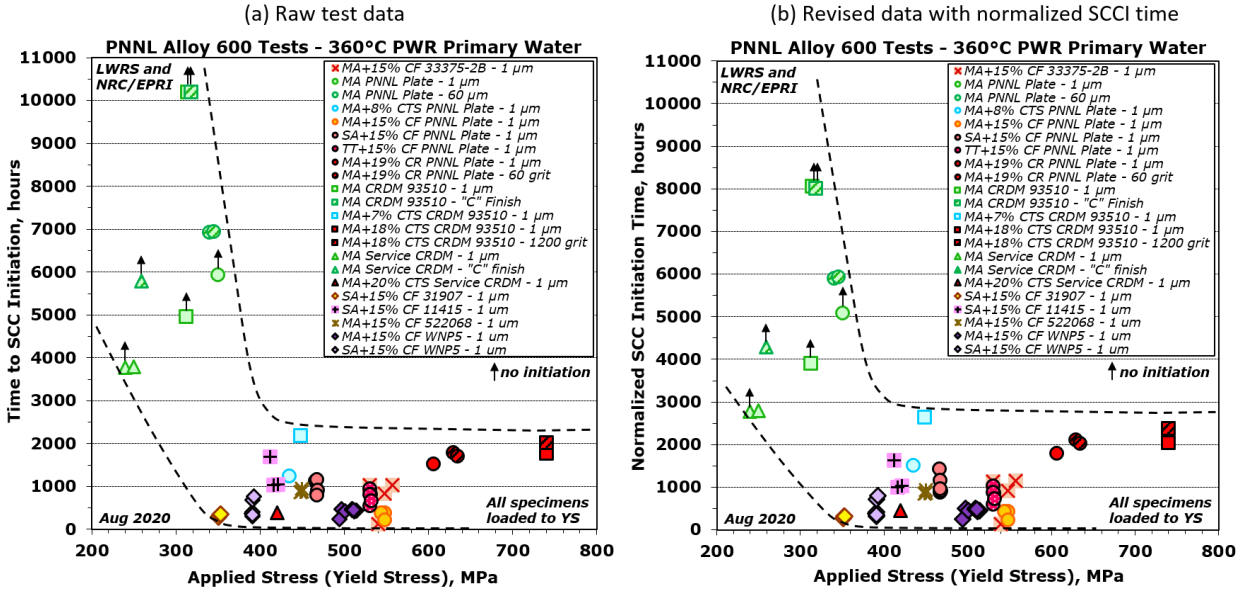

Figure 41. Correlation between practical SCC initiation and applied stress using SCC initiation time measured by DCPD (a) and SCC initiation time normalized to a standard gauge diameter (b). Dashed lines are meant to bound the data and aid in visualization of the initiation response.

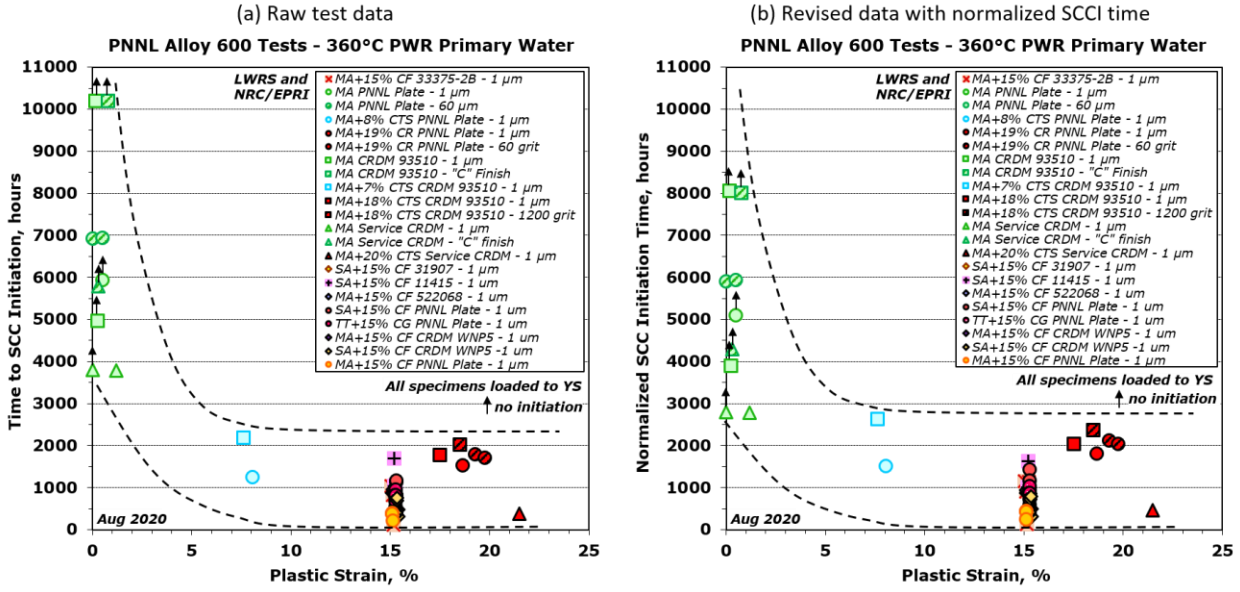

Figure 42. Correlation between practical SCC initiation and plastic strain using SCC initiation time measured by DCPD (a) and SCC initiation time normalized to a standard gauge diameter (b). Dashed lines are meant to bound the data and aid in visualization of the initiation response.

(a)

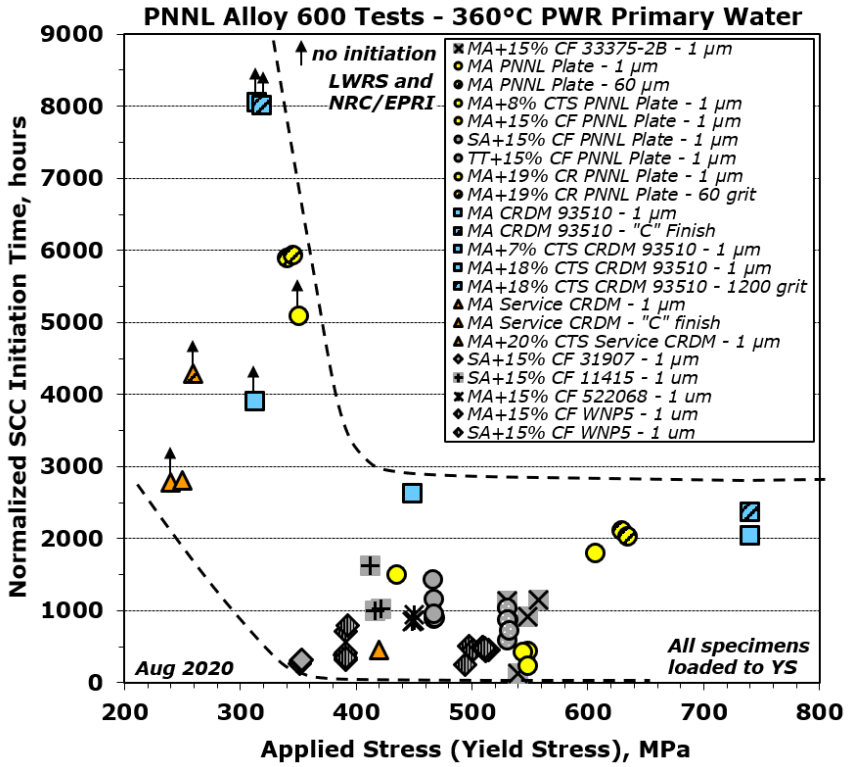

(b)

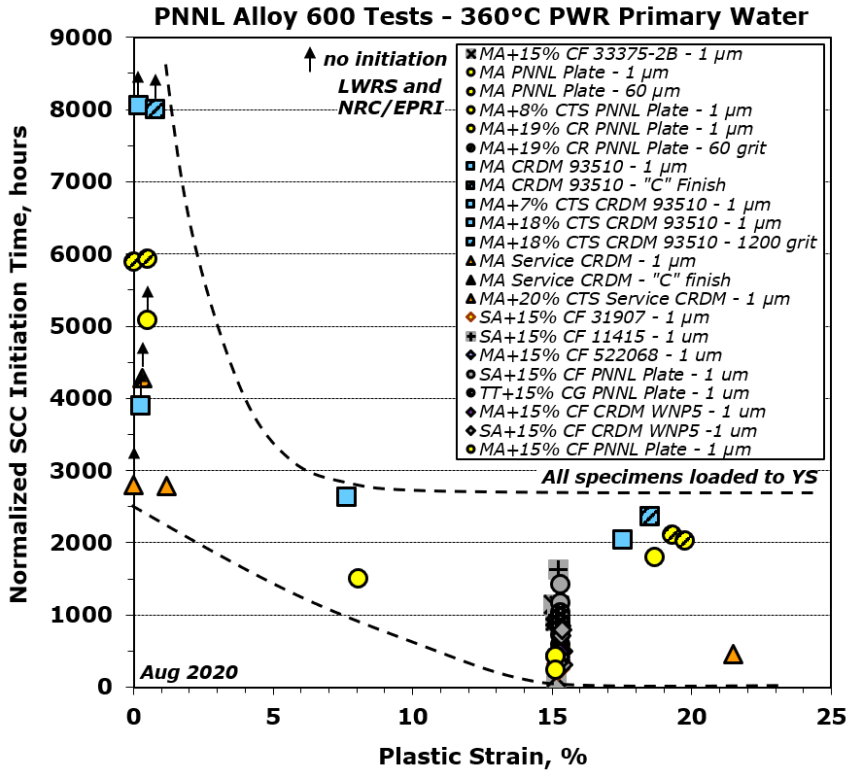

Figure 43. Normalized SCC initiation time as a function of applied stress (a) and plastic strain (b) with the heats evaluated for these dependencies highlighted in colors (yellow – A600MA plate heat NX6106XK-11, blue – A600MA CRDM tubing heat 93510, and orange – A600MA service CRDM heat M3935).

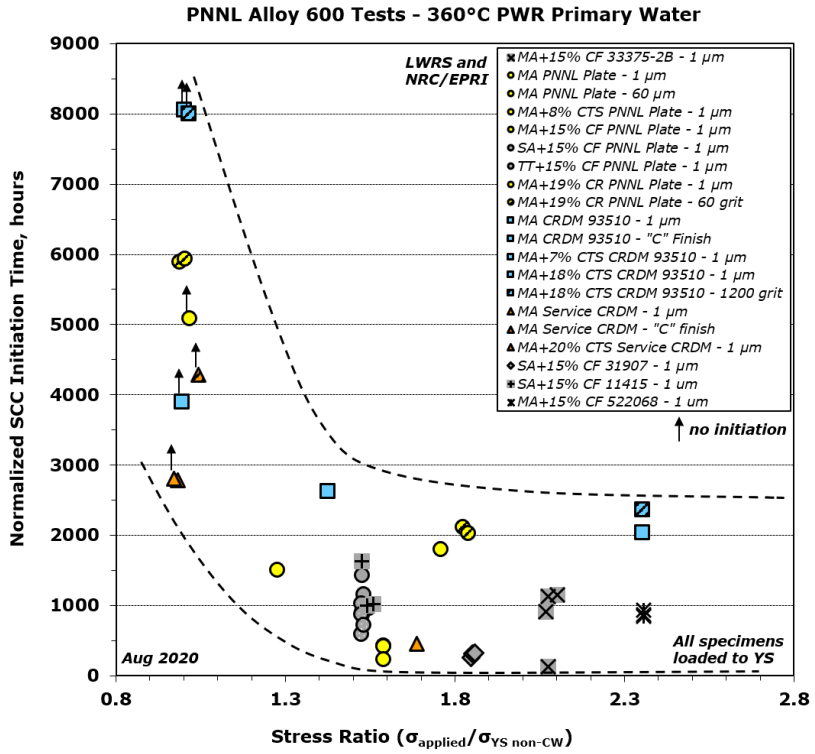

Figure 44. Normalized SCC initiation time as a function of stress ratio with the heats evaluated for stress and cold work dependencies highlighted in colors (yellow – A600MA plate heat NX6106XK-11, blue – A600MA CRDM tubing heat 93510, and orange – A600MA service CRDM heat M3935).

Results presented above clearly demonstrated that cold work can greatly reduce the resistance to SCC initiation in Alloy 600. A similar strong effect of cold work on SCC propagation was also found in CGR testing. However, the CGR values were usually obtained using a *K* of 20 MPa√m or higher, which is above the range relevant to the practical SCC initiation investigated in this study. To better link SCC initiation and crack growth at lower *K* levels, complimentary CGR testing were conducted in collaboration with an NRC project at PNNL to more fully compare SCC initiation response to low *K* SCC growth response. In Figure 45, the SCC initiation response and CGR response are displayed side-by-side with heats investigated in both tests highlighted in the same color. Several trends were revealed: the first being for a single heat, time to practical SCC initiation decreases with increase in susceptibility to crack growth at low *K* levels. This is evidenced by the significant increase in CGR in the Alloy 600MA plate heat NX6106XK-11 from the non-CW to the 15%CF condition, which is consistent with much longer initiation time detected in the non-CW materials (~6000 hours vs. ~400 hours at 360°C). Another trend is that for materials in non-CW condition or with the same cold work level, the heat showing higher CGRs also exhibits a lower SCC initiation time. For example, the 15%CW Alloy 600SA heat 31907 exhibited the highest CGRs at low *K* and the shortest SCC initiation times (~260-320 hours). The four highlighted 15%CF Alloy 600MA heats exhibited similar but slightly longer SCC initiation times between 400-1200 hours, which also showed similar CGRs at low K that are slower than the SA+15%CW 31907 heat. IN the non-CW materials, a ~2X lower SCC initiation was observed for the service CRDM heat M3935 that is highly susceptible to SCC growth in comparison to the plate heat NX6106XK-11. The fact that the SCC initiation response correlates well with the low-*K* CGR in multiple Alloy 600 heats indicates that short crack growth plays a key role in practical SCC initiation of Alloy 600. The obtained data will be used to develop the SCC initiation model which will be discussed later.

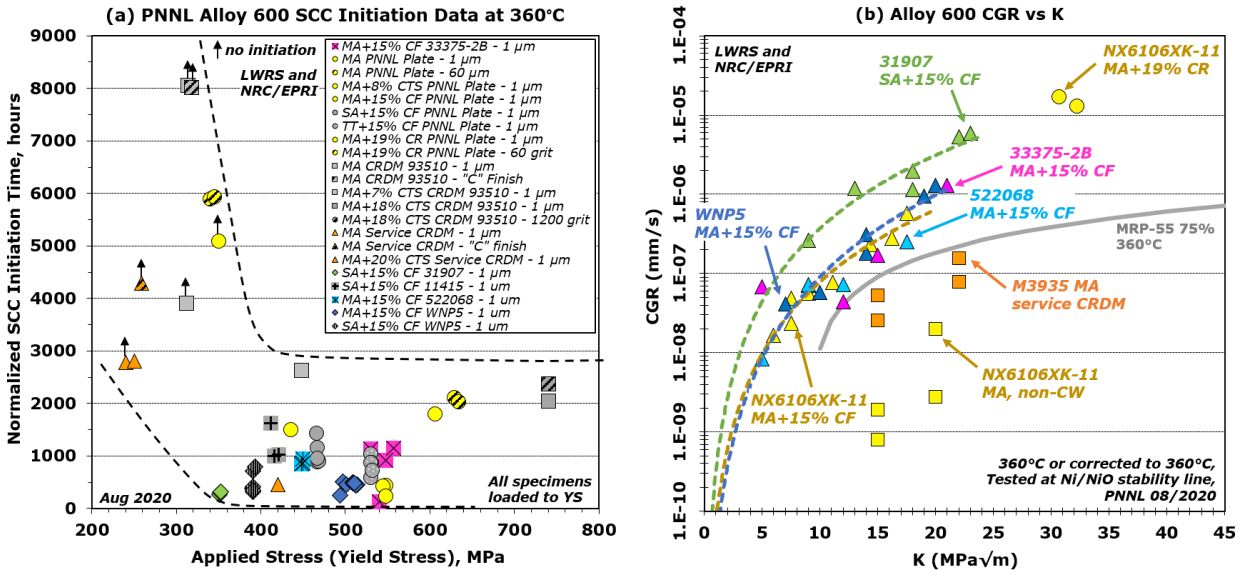

Figure 45. (a) Normalized SCC initiation time as a function of applied stress and (b) measured SCC CGRs for Alloy 600 materials as a function of stress intensity *K* in 360°C simulated PWR primary water. The heats evaluated for both SCC initiation and crack growth response are highlighted using the same colors in both plots.

Another key aspect of this study was to evaluate the effect of applied stress and cold work on IGA development. In order to achieve this, unstressed exposure tests and SCC initiation tests were performed on selected heats with planned interruptions. At each test interruption, one specimen from each investigated material condition was removed from the test for destructive examinations. IG precursor damage was documented on the cross-section of the removed specimen at each test interruption, enabling the evolution of the precursor damage depth to be recorded as a function of time. To ensure representativeness of the data, IGA depth measurements were performed on more than 100 random high-energy GBs in each specimen. An overview of the results is presented in Figure 46 for the most extensively investigated Alloy 600MA plate heat NX6106XK-11. In unstressed exposure coupons, both the non-CW and CW materials exhibited a gradual increase in IGA as exposure extends with a rate fast decreasing with time. It is interesting to note that for the same exposure length, IGA seemed to have grown deeper in the non-CW than in the 15%CW condition. This can be possibly attributed to a more compact chromia layer formed on the surface of the CW materials due to faster diffusion of Cr along GBs and other short circuit paths created by cold working [48], but further investigation is needed to confirm this hypothesis. In comparison with their unstressed counterparts, a significantly faster increasing trend over time was seen on the 15%CF SCC initiation specimens. Within 500 hours, the value of the average IGA depth has already increased by >2X than that in the unstressed specimens after 4400 hours of exposure. Data with longer exposure times is not available for the 15%CF SCC initiation specimens because all tested samples initiated within 500 hours. Meanwhile, a smaller yet obvious increase in the average IGA depth was also observed for the non-CW SCC initiation specimens after ~6000 hours of exposure as compared to the trend shown for its unstressed counterpart. These findings indicate a key role of applied stress in the IGA growth preceding crack nucleation.

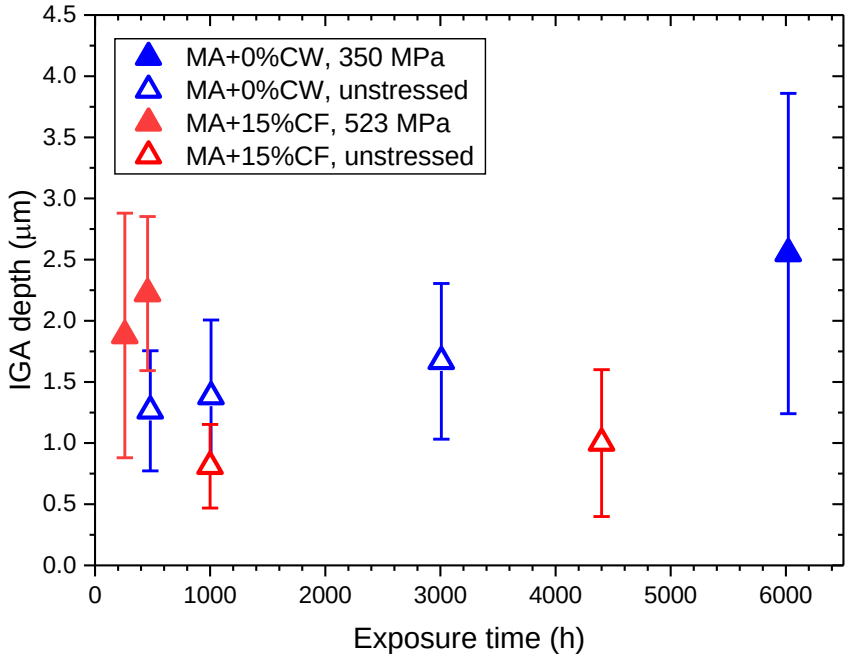

Figure 46. Comparison of the average IGA depth evolution over time in the Alloy 600MA heat NX6106XK-11 in unstressed exposure coupons and SCC initiation specimens loaded at material yield stress in both non-CW condition (blue) and 15%CF condition (red). The tests were all conducted in 360°C simulated PWR primary water.

Effects of Material Factors on Practical SCC Initiation of Alloy 600

Grain Boundary Carbides

Grain boundary carbides produced by thermal treatment are considered beneficial in improving the resistance to SCC crack growth in Alloy 600, but it remains unclear how they influence SCC initiation. Therefore, one set of test has been performed on the Alloy 600MA plate heat NX6106XK-11 to evaluate the effects of heat treatment and grain boundary carbides on the key steps leading to practical SCC initiation (Table 3).

Measurements of the IGA depth evolution over time was performed on the 15%CF MA, SA, and SA+TT SCC initiation specimens following the same methodology described in the above section with results shown in Figure 47. Typical morphology of the IGA and short crack morphology in these different material conditions can be found in a milestone report published last year [49]. Upon encountering a GB carbide, IGA always bifurcates and circumvents along the carbide/metal interface before the two ends rejoin and continue to move forward down the GB. Interestingly, the carbides that are reached by IGA usually could not preserve their original ellipsoidal shape but appear to be eaten away by exhibiting a thin Ni-rich/Cr-depleted layer between the IGA and the Cr-rich core with rough, serrated edges. These characteristics are indicators of enhanced local corrosion/oxidation around carbides, but they do not seem to have slowed down IGA penetration into the material. As shown in Figure 47, the IGA depth and its evolution over time does not reveal any statistically significant difference between the MA, SA, and SA+TT 15%CF Alloy 600 materials in either unstressed or stress-assisted conditions. Instead, applied stress appears to exert a predominant role over GB microstructure in IGA growth. This is also illustrated in Figure 47, where the stress-assisted IGA in SCC initiation specimens loaded at yield stress exhibit an average depth roughly twice as deep as the IGA in the unstressed exposure coupons after 1000 hours of exposure. It is also obvious that the stress-assisted IGA in all SCC initiation specimens grow much more rapidly with increasing exposure time than the IGA in the unstressed samples.

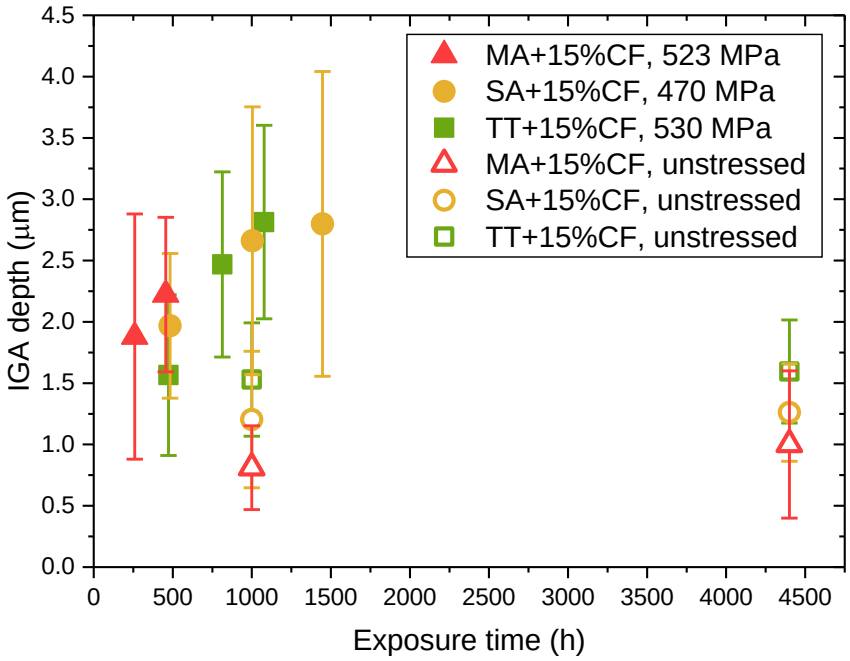

Figure 47. Summary of the time evolution of average IGA depth in the 15%CF Alloy 600MA, SA and TT heat NX6106XK-11 unstressed exposure coupons and SCC initiation specimens loaded at yield stress in 360ºC simulated PWR primary water.

The next analysis incorporated the depth statistics on short cracks (<10 μm) into the uncracked IGA in the form of cumulative frequency distributions for the SCC initiation specimens in all three materials conditions (Figures 48-50). It should be noted that data at each test interruption is acquired from a different specimen. Considering that specimens with the same material condition should behave similarly, insights can be obtained on the precursor damage evolution from these statistics. Firstly, a gradual increasing trend was observed for the depth of precursor damage with the increase in exposure time. Nevertheless, despite the increase in exposure time, the percentage of short cracks remained relatively stable at ~10% for the SA and TT+15%CF conditions, but increased from <5% to >20% in the MA+15%CF condition. To better visualize the contribution of these short cracks to the overall distribution, the depth of short cracks is also plotted for each specimen in the bar diagram in terms of percentage of short cracks over all GBs observed. It turns out that with the progression of test time, the formation of new cracks in the SA and TT+15%CF condition appears limited because the specimens underwent longer exposure did not show a higher fraction of very short cracks, but instead, they show a higher distribution gravitating towards deeper cracks. This suggests that in all material conditions, nucleation of new cracks decreases as exposure time increases, although IGA continued to grow. One possible explanation for this phenomenon is that the transition from IGA to short cracks is associated with bulk creep strain rate – with the exhaustion of primary creep at early stage of the tests, it becomes difficult for new cracks to form compared to growth of existing cracks. This finding seems to agree with a study by Parkins et al. [50], where they demonstrated in constant load tests that a sufficiently fast creep strain rate is necessary for cracking to take place given favorable electrochemical conditions.

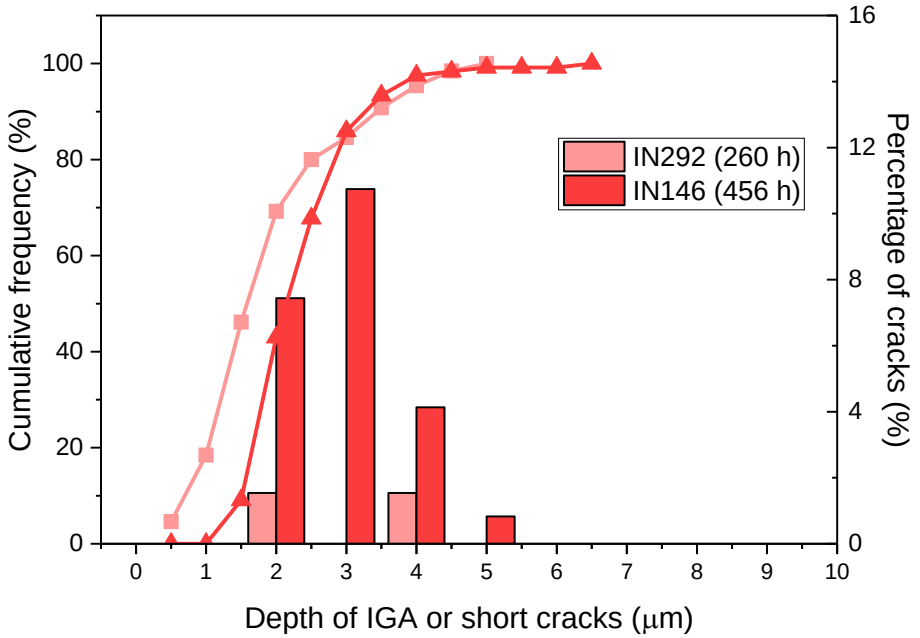

Figure 48. Cumulative frequency of precursor damage depth for the 15%CF Alloy 600MA heat NX6106XK-11 SCC initiation specimens taken out at each test interruption and the conclusion of the tests in 360ºC simulated PWR primary water.

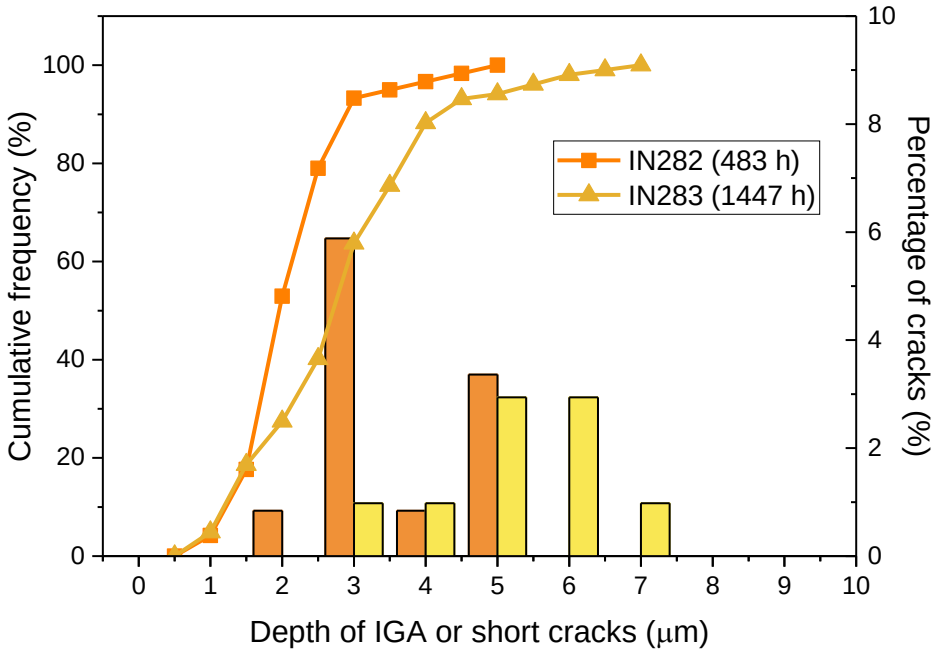

Figure 49. Cumulative frequency of precursor damage depth for the 15%CF Alloy 600SA heat NX6106XK-11 SCC initiation specimens taken out at each test interruption and the conclusion of the tests in 360ºC simulated PWR primary water.

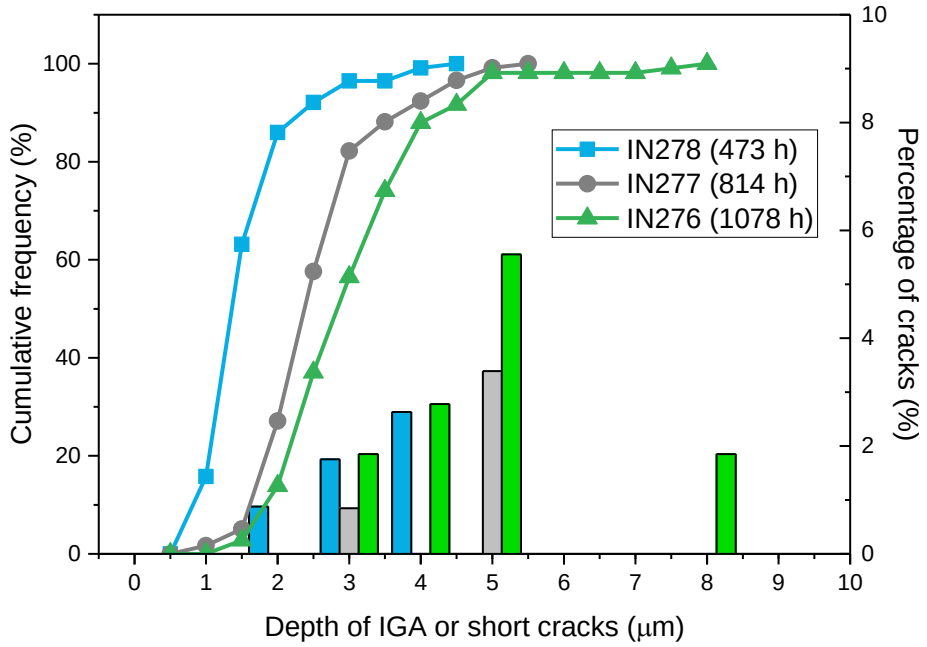

Figure 50. Cumulative frequency of precursor damage depth for the 15%CF Alloy 600TT heat NX6106XK-11 SCC initiation specimens taken out at each test interruption and the conclusion of the tests in 360ºC simulated PWR primary water.

Effects of material condition and GB carbides on practical SCC initiation behavior was first evaluated for the plate heat NX6106XK-11 with results shown in Figure 51. DCPD-detected SCC initiation time data were collected for three specimens in the MA+15%CF condition and five specimens from both the SA and SA+TT+15%CF condition. The detailed DCPD response can be found in a previous report [49]. Comparison on the normalized SCC initiation times between the MA, SA, and SA+TT 15%CF Alloy 600 materials suggests that GB microstructure may have modified SCC initiation behavior as a result of thermal history. In general, the SA and SA+TT 15%CF specimens exhibited much longer SCC initiation times and more gradual increase in the DCPD referenced strain [49], indicating an improved resistance to short crack growth in these two conditions over the MA condition. However, it should be noted that the MA+15%CF specimens exhibited inhomogeneous microstructure that likely shortened the time to practical SCC initiation from a uniform microstructure. This will be discussed in more detail in a later section focusing on the effect of grain size. Meanwhile, the SA+ and SA+TT 15%CF materials did not exhibit significant difference in SCC initiation time and SCC initiation morphology. In fact, the TT+15%CF specimens even exhibited slightly shorter SCC initiation times (500-1000 hours) in comparison to the SA+15%CF specimens (800-1100 hours), but the trend is likely to be convoluted by different magnitudes of stress applied during test on these two types of specimens. As shown in Figure 51, the TT+15%CF specimens were loaded at a yield stress ~12% higher than that of the SA+15%CF specimens.

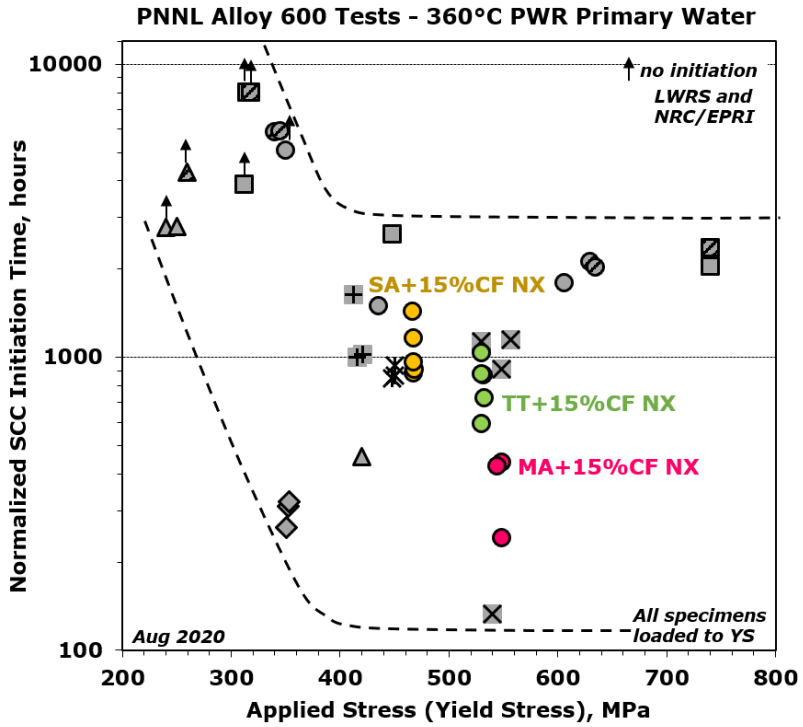

Figure 51. Normalized SCC initiation time as a function of applied stress for CW Alloy 600 materials tested at yield stress in 360ºC simulated PWR primary water highlighted with the three material conditions investigated for the plate heat NX6106XK-11.

Since the assessments on the plate heat NX6106XK-11 is somewhat inconclusive, another CRDM nozzle heat WNP5 was selected for an additional round of evaluation to better understand material condition effects on SCC initiation (Table 3). The schedule of this testing effort has been delayed by the COVID-19 pandemic and the last test of this series on the TT+15%CF is still ongoing at the time of writing. Nevertheless, sufficient data on SCC initiation times have been collected and the results are highlighted in Figure 52. While also showing high susceptibility in its as-received MA condition after 15% cold working with SCC initiation times between ~200 – 400 hours, this heat exhibits a more uniform microstructure than the plate heat NX6106XK-11. Interestingly, solution annealing and subsequent thermal treatment did not show obvious improvement over the MA condition in SCC initiation resistance for this material. As shown in Figure 52, four of the six SA+15%CF specimens exhibited practical SCC initiation between ~250-350 hours and two of the six TT+15%CF materials exhibited practical SCC initiation around ~300 hours of exposure. Again, the trend may have been convoluted by the ~12% difference in applied stress (i.e. yield stress) between the MA, TT, and SA+15%CF condition. Extra complexity might involve different *K* dependence of CGR in the short crack growth regime for the different material conditions. Nevertheless, the unexpected observation of the SCC initiation time being consistently lower for the TT+15%CF condition with higher applied stress than for the SA+15%CF with lower applied stress in both heats may indicate that mechanical factor (i.e. applied stress) has a predominant role over GB carbides in SCC initiation of Alloy 600. It also suggests that the beneficial role of thermal treatment observed in SCC crack growth of Alloy 600 does not readily apply to SCC initiation. One possible reason is that the thermal treatment usually leads to a certain degree of Cr depletion along the GBs due to heavy precipitation of Cr-rich carbides. This can degrade material resistance to IGA as revealed in Figure 47 and eventually lead to more rapid SCC initiation. Detailed cross-section examinations will be performed on IGA and short cracks in the WNP5 specimens after the last test concludes to verify whether the same trend will be found.

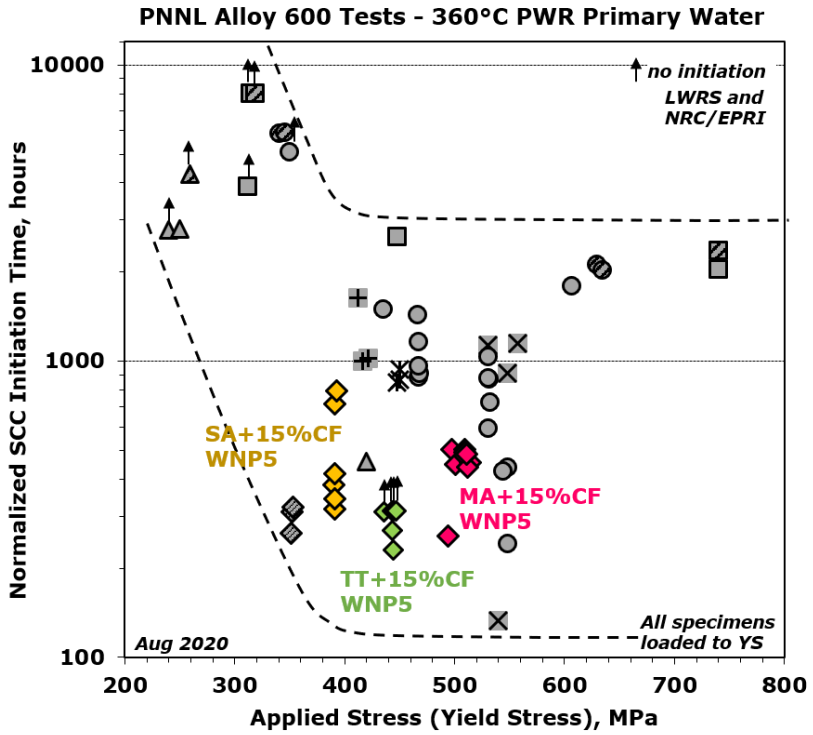

Figure 52. Normalized SCC initiation time as a function of applied stress for CW Alloy 600 materials tested at yield stress in 360ºC simulated PWR primary water highlighted with the three material conditions investigated for the CRDM heat WNP5. Note that the evaluation on the TT+15%CF condition is ongoing with SCC initiation detected by DCPD in two specimens so far.

Grain Size

While the effect of grain size could not be explicitly isolated without considering other mechanical or materials factors, its impact on SCC initiation has been observed in at least two different scenarios. The first is that the grain size can affect the way crack coalescence. As discussed in Key Steps Leading to Practical SCC Initiation, the criterion for two off-set, neighboring cracks to coalesce depends on their lateral distance falling within a certain range so that the crack tip plastic zone of the two cracks can interact. This critical distance is usually ~14% of the average surface length of the two interacting cracks. As a result, the coalescence of off-set neighboring cracks plays a lesser role in materials with large grain size (i.e. hundreds of micrometers). However, it has been observed that coplanar coalescence still exists in these materials as short cracks nucleated at different GBs can link together when they share mutual GBs roughly along the same plane, especially when the plane is normal to the direction of the applied stress. The resultant impact on SCC initiation can go either way. On one hand, it can retard practical SCC initiation because of reduced opportunity of forming large cracks; on the other hand, it can also promote time to SCC initiation since a lesser density of cracks suggests fewer cracks will be retarded due to stress shielding from growth and coalescence of other cracks, therefore a higher chance to grow into a critical size leading to practical SCC initiation. In either case, the outcome cannot be determined directly without considering synergistic effects with other factors and the situation may need to be evaluated case-by-case.

Another important finding is that microstructural inhomogeneity associated with grain size can strongly impact SCC initiation behavior of materials. As reported previously [22], the MA and cold worked Alloy 600 plate heat NX6106XK-11 materials usually exhibit an SCC initiation between ~1000–2000 hours when tested at yield stress in 360°C simulated PWR primary water. However, unexpected short SCC initiation times were measured between 220 and 400 hours for three MA+15%CF specimens

(Figure 53). Detailed microstructural characterizations revealed that the inhomogeneous microstructure appears to promote differences in SCC initiation response [51]. Early crack initiation was found to preferentially occur at sporadic large elongated grains in the banded plate especially when it protruded deep into the gauge (Figures 54 and 55). This is consistent with the SCCGR measurements on CW Ni-base alloys with inhomogeneous microstructures, where higher propagation rates have been reported when aligning the cold work and crack growth directions with the banded microstructure [52-54].

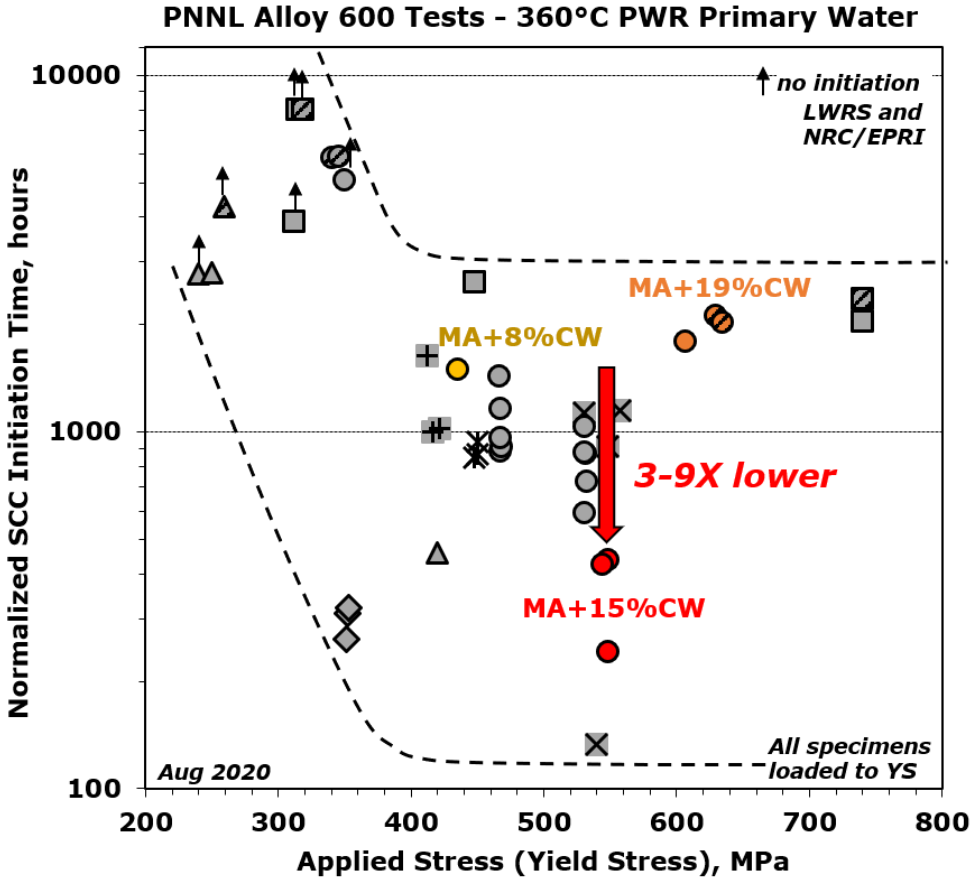

Figure 53. Normalized SCC initiation time as a function of applied stress. Dashed lines are meant to bound the data and aid in visualization of the initiation response. The data from CW Alloy 600MA plate heat NX6106XK-11 specimens are highlighted.

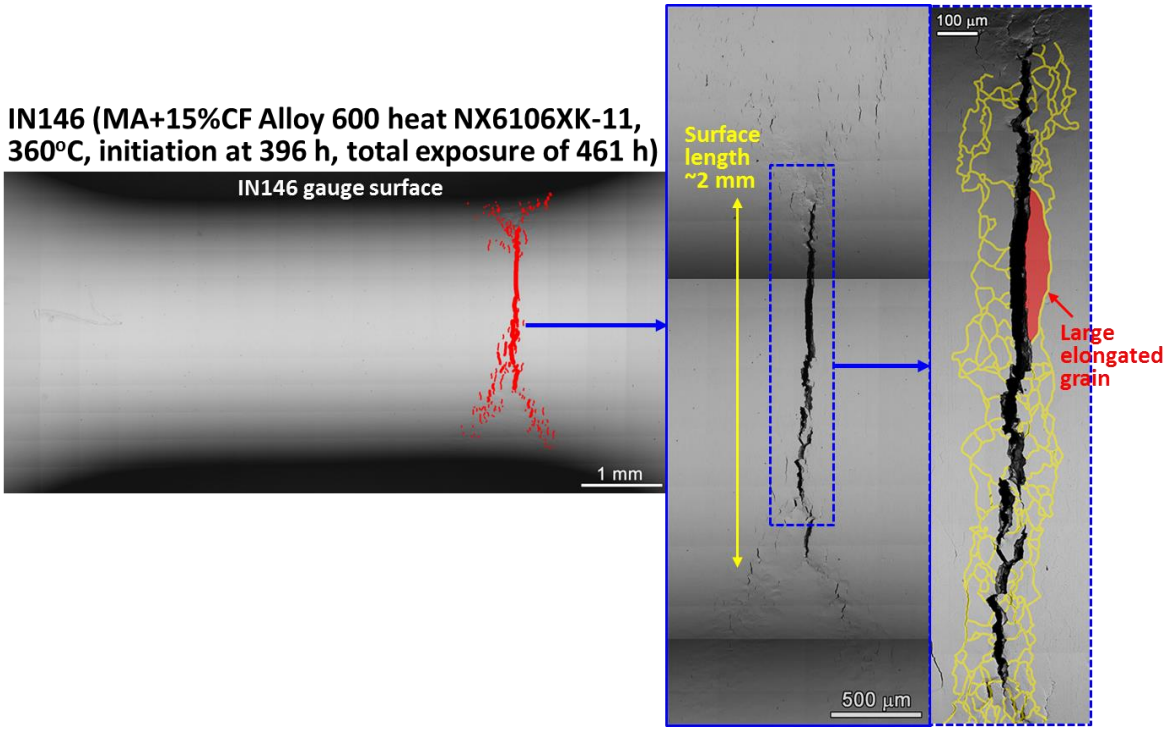

Figure 54. Post-test SEM-BSE imaging on the gauge surface of the MA+15%CF Alloy 600 plate heat NX6106XK-11 specimen IN146 with DCPD initiation detection at 396 hours of exposure (total exposure of 461 hours). The primary crack was found to nucleate along an elongated large grain in a banded region where grain boundaries are highlighted in yellow.

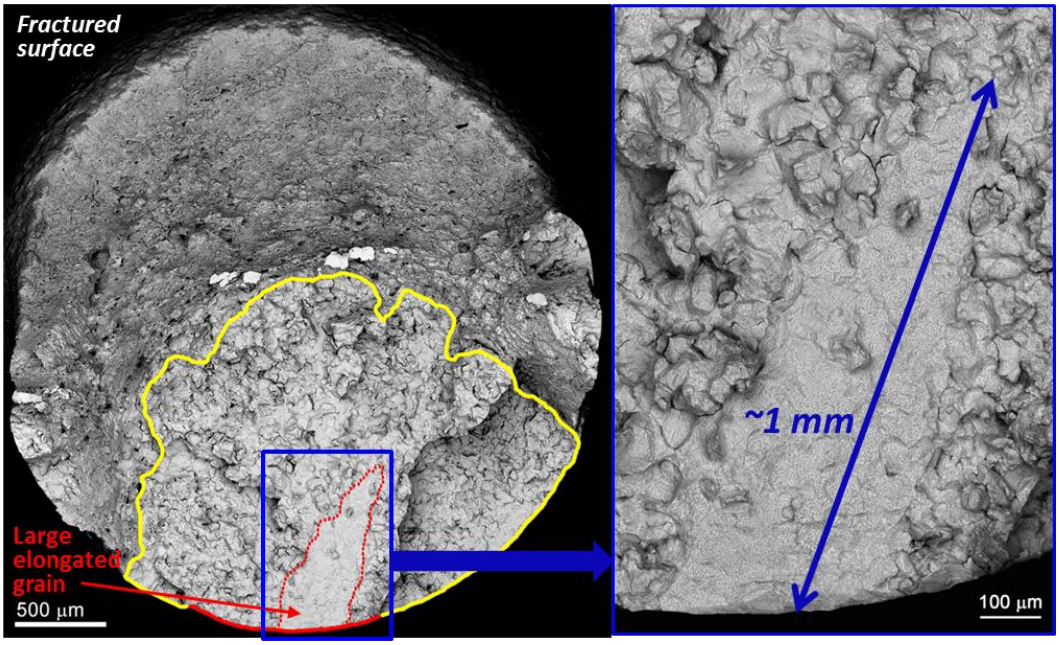

Figure 55. SEM-BSE imaging on the fracture surface of the MA+15%CF alloy 600 plate heat NX6106XK-11 specimen IN147 with DCPD initiation detection at 385 hours of exposure. The region of IG failure is enclosed in yellow with the primary crack on the surface identified in red. The region of the large elongated grain is outlined using dashed red lines to aid visualization and a zoom-in image of the region is provided on the right side.

Others

Surface Finish

Service experience suggest that SCC initiation first occurs on highly stressed, heavily damaged or ground surfaces, which is believed to be caused during component assembly activities or from loose part impacts during reactor operation [55-57]. This surface damaged region can include a thin nanocrystalline layer with extreme levels of deformation and a work-hardened layer below it that can have high levels of deformation but more closely resembles the bulk grain shape. This work-hardened layer is typically produced at lower temperatures and is often effectively a CW region. The depth of the work-hardened layer depends strongly on how the deformation was introduced, and the total thickness of the surface damaged region may have a strong influence on SCC initiation time [46, 55, 58]. A shallow cold work layer (<20 μm deep) is reported to have little effect on initiation time whereas a thick surface damaged layer can increase crack density, allow for rapid crack extension deeper into the material, and reduce SCC initiation time [55, 58]. For the present work, the surface damaged layer from grinding was found to be less than 50 μm deep in the non-CW Alloy 600 specimens suggesting that it should have little effect on initiation time. In fact, the direct comparisons of data presented in Ref.[21] suggest that the ground specimens initiate slightly after the polished specimens. Because of the relatively thin surface damaged layer for these specimens, this trend for longer initiation times could be considered data scatter in a thickness regime where there is little effect on SCC initiation time. However, comparison of the oxide morphology near surface between highly polished samples and ground samples suggest that additional time is required for corrosion and cracking to proceed through the ground region. It is shown that in the ground sample, corrosion occurred almost exclusively in the thin layer of recrystallized nanocrystalline grains produced by aggressive grinding. This is consistent with various experimental observations obtained on both stressed and unstressed Alloy 600 samples in similar environmental conditions [59, 60]. High-resolution composition analysis revealed a thin film of Cr-enriched oxide on the outer surface of the sample and elevated Cr content in the surface damage layer [59]. Therefore, the deformed nanocrystalline layer not only creates a microstructural barrier (albeit temporary) between bulk grain boundaries and the environment, but may also accelerate Cr diffusion to the surface to produce more protective oxides. In comparison, a highly polished surface ensures that all grain boundaries reaching the surface have direct access to the corrosion environment and IGA can begin immediately on exposure.

Effects of Environmental Factors on Practical SCC Initiation of Alloy 600

Temperature

Laboratory SCC initiation testing is often performed at temperatures above typical PWR operating conditions to accelerate degradation. To allow extrapolation of elevated temperature results to more PWR-relevant temperatures, correlations between initiation time and test temperature have been investigated in this study. In addition, to better link SCC initiation and crack growth and to develop a mechanistic model of SCC initiation, complementary crack growth testing has been conducted in collaboration with an NRC project at PNNL to evaluate the effect of temperature on SCC crack growth response. Three mill-annealed (MA) Alloy 600 heats WNP5, 522068, 33375-2B and one solution annealed (SA) heat 31907 in 15% cold forged (CF) condition were tested for CGR evaluation. Three of these materials (SA+15% CF 31907, MA+15% CF 522068, and MA+15%CF WNP5) were also evaluated for SCC initiation behavior plus an additional MA heat (MA+15% CF NX6106XK-11). For the SCC crack growth tests, one CT specimen was investigated from each material condition maintaining nearly the same stress intensity between the different observations. The CGR values were measured using in-situ DCPD technique. More details on these tests can be found in the chapter of Experimental Methods. For the SCC initiation tests, three tensile specimens were evaluated at each temperature for each material condition at constant load equivalent to the material yield stress. All SCC initiation and crack growth tests were performed in simulated PWR primary water with dissolved hydrogen concentration adjusted to maintain the electrochemical corrosion potential equivalent to the Ni/NiO stability line.

The results of the SCC initiation and CGR measurements are both presented in Figure 56 as a function of temperature in the form of 1/T. As the time of writing, one more test is still ongoing to evaluate the SCC initiation response of the MA+15%CF WNP5 materials at 325°C, but an obvious trend was already revealed by the data collected so far. A consistent decrease in CGR was revealed in all four heats with decreasing temperature from 360 to 342 to 325 to 300/290°C. The results indicate an activation energy of ~145 kJ/mol for the SA+15%CF heat 31907 and ~120-160 kJ/mol for the three MA + 15%CF Alloy 600 heats, suggesting heat-to-heat variability has a higher impact on temperature dependency than heat treatment alone. In comparison, three heats (SA+15%CF 31907, MA+15%CF 522068, and MA+15%CF WNP5) exhibited an apparent plateau in SCC initiation time between 342 and 360°C. This is different from the trend observed in their crack growth response and also different from prior results by KAPL showing a classic Arrhenius dependence for tests conducted at multiple temperatures between 316°C and 360°C [18, 61]. These findings clearly indicate different dependency on temperature between SCC initiation and crack growth in CW Alloy 600. Since the trend in temperature dependency for crack growth is not expected to change significantly with the magnitude of *K*, the difference in temperature dependency observed between SCC initiation and crack growth is likely associated with a different temperature functionality on IGA development. Unfortunately, due to the impact of the COVID-19 pandemic, detailed analysis has yet to be performed on this topic and the results will be reported in the future.

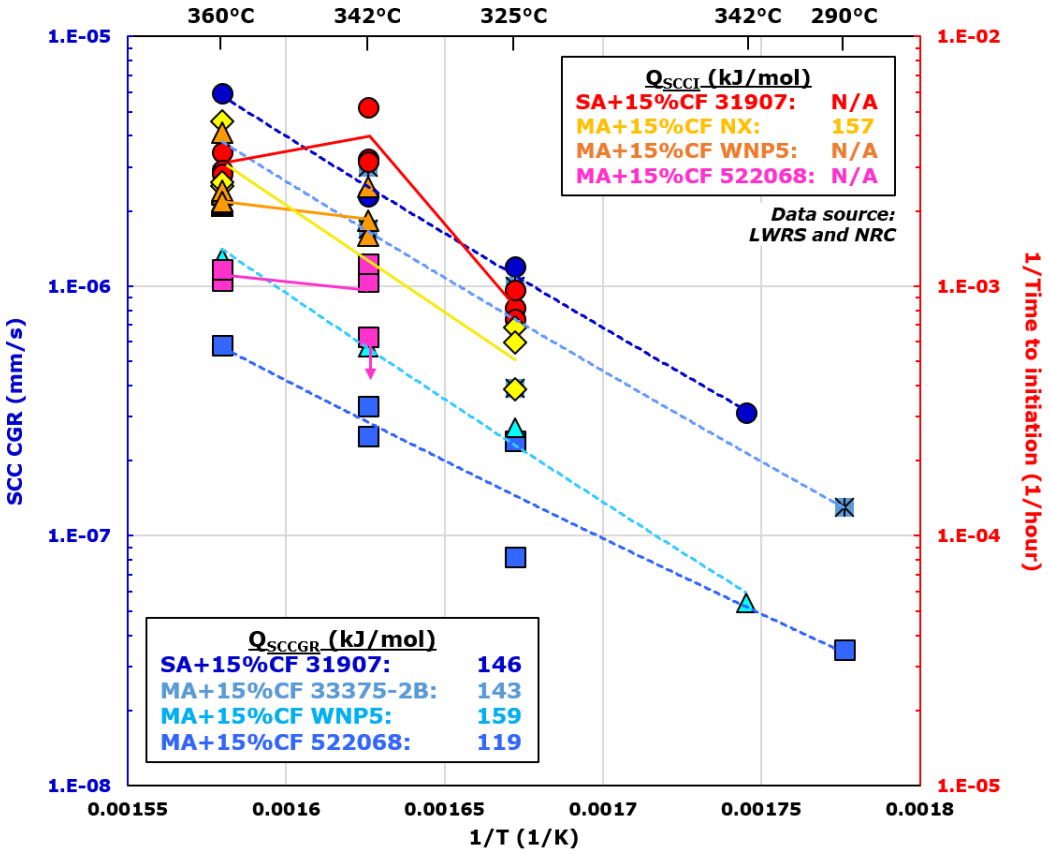

Figure 56. SCC initiation times (in shades of yellow and red) and SCCGR (in shades of blue) plotted as a function of testing temperature for the Alloy 600 heats evaluated for temperature dependence in simulated PWR water at 290-360°C with a dissolved H_2 concentration corresponding to the Ni/NiO stability line at each temperature.

Dissolved Hydrogen

It is generally agreed that both SCC initiation and crack growth exhibit a peak in susceptibility at corrosion potentials in proximity to the Ni/NiO phase transition. The dissolved hydrogen (DH) for all SCC initiation tests performed has been adjusted to the level matching this transition line to optimize data acquisition efficiency. Due to limited resources, no tests were performed at other DH levels to investigate the effect of DH (i.e. corrosion potential) on SCC initiation of Alloy 600 in PWR primary water. However, Etien et al. [18] have performed extensive testing on this topic on an high-temperature annealed Alloy600 heat using the same test methods as ours and found that the SCC initiation times are much longer under conditions where NiO is stable than where Ni metal is stable (Figure 57). Consistent findings were also obtained with tests using conventional reversed U-bend specimens, and this trend has been reported independent of test temperature on the NiO stability region but shows a more progressive decrease in SCC initiation susceptibility on the Ni metal stability region with increase in temperature [62]. This is different from the response of SCC crack growth to DH where SCCGR tended to decrease symmetrically when moving away from the Ni/NiO phase transition into either the Ni metal or NiO stability region. This trend has also been shown as independent of stress intensity when $K \geq 27.5$ MPa$\sqrt{m}$ [63]. In addition, unstressed exposure and post-exposure straining tests were performed by Fournier et al. to evaluate the effect of DH on IG oxygen penetration and GB embrittlement in Alloy 600 exposed to 325°C simulated PWR primary water [64]. The results demonstrated maximum in IG cracking at corrosion potentials close to the Ni/NiO equilibrium potential during post-exposure straining, which coincides with the known maximum in PWSCC propagation susceptibility as a function of corrosion potential. However, no direct data was provided on the IGA development as a function of DH, especially in scenarios where stress is present. Future research on this topic will be valuable to improve the understanding on the effect of DH on the early precursor stage of SCC initiation and to allow better prediction of SCC initiation in service relevant environments.

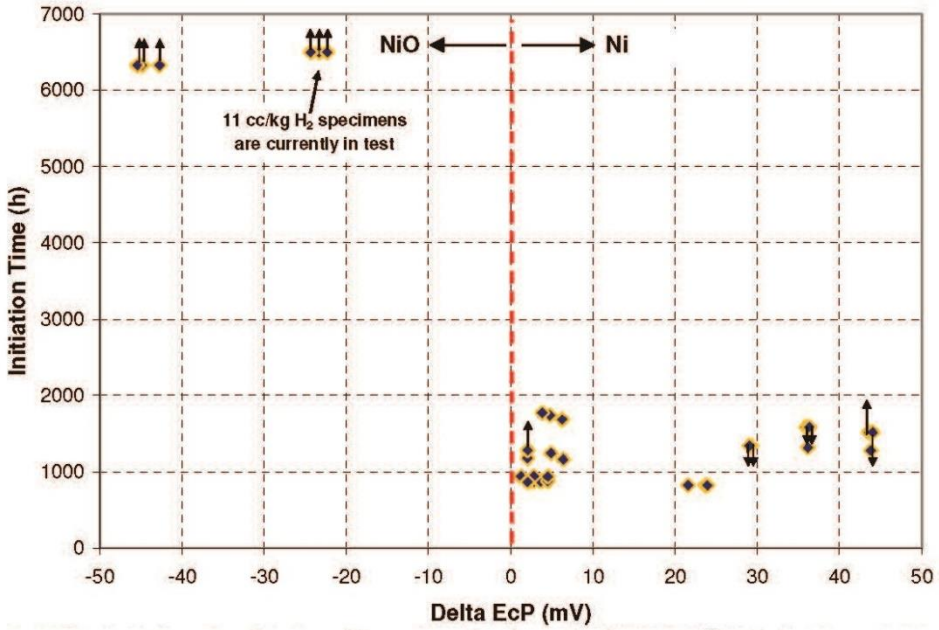

Figure 57. Effect of DH on the SCC initiation time measured by DCPD in a high-temperature annealed Alloy 600 in 360°C simulated PWR primary water [18].

Modeling Practical SCC Initiation in Alloy 600

Model Development

Mechanistic Implications from Experimental Data

The obtained experimental data revealed several important mechanistic insights on the SCC initiation behavior of Alloy 600. Despite heat-to-heat variability in SCC initiation response, the effects of influencing factors are consistent across different heats and material conditions:

- Applied stress and cold work (i.e. material strength) have a predominant effect on both IGA development and short crack growth that are involved in the practical SCC initiation of Alloy 600. In general, SCC initiation susceptibility increases with increasing applied stress and cold work level, but the effect is more evident between non-CW and CW conditions instead of variation in cold work level for CW materials. For IGA development, stress-assisted IGA in SCC initiation specimens grew much faster than IGA in the unstressed coupons after identical exposure time for any given material condition. For short crack growth, the crack growth and coalescence are found to be governed by mechanics-based relationships. In addition, it is demonstrated that the transition between IGA and short crack and between short crack growth and practical initiation are also of mechanics nature and can be associated with critical damage size and applied stress.
- The functionality of temperature seems to be different for SCC initiation and crack growth. Crack growth has a typical Arrhenius relationship with temperature between 290-360°C. In comparison, SCC initiation time showed a plateau in the 340-360°C range for multiple Alloy 600 heats. Since crack growth dependency on temperature is likely independent of *K*, the observed different response to temperature between practical SCC initiation and crack growth is likely dominated by IGA development. Currently additional characterizations are underway to investigate the cause of this difference.
- Grain boundary carbides (i.e. heat treatment) and surface condition do not appear to have obvious impact on practical SCC initiation of Alloy 600.
- Larger grain size can reduce the likelihood of crack coalescence. Microstructural inhomogeneity associated with abnormally large grain tend to promote SCC initiation.

In addition, results acquired through systematic testing and characterizations on IGA development and short crack growth helped underpinning the controlled mechanism in each step and provided quantitative data to determine the criteria between transition of the two stages and to practical SCC initiation. In the following sub-sections, the efforts on model development for each of these categories will be detailed.

Modeling IGA Development

As shown in Figures 46 and 47, the average IGA depth in the specimens increases over time with a decreasing rate that is close to a parabolic relationship with time. This suggests a solid state diffusion controlled process that can be described using the Wagner's model [65] in the following equation:

$$x^2 = k_p t \tag{21}$$

where in this case, *x* is the IGA depth and k_p is the corrosion constant that is usually associated with diffusivity. A number of studies have performed stress-assisted oxidation investigation on Ni-based alloys [66, 67] and demonstrated that accelerated diffusion resulted by applied stress promoted IG penetration in materials. More specific formulations of k_p were proposed based on stress and diffusivity relationship, but in this study a direct fit to k_p based on our test data was employed first for simplicity using data summarized in Figures 46 and 47. The curve fitting to average IGA depth data against exposure time using Equation (21) is shown in Figure 58 for stressed and unstressed specimens from the Alloy 600 plate heat NX6106XK-11 in both CW and non-CW conditions. The curves fit well for the stressed-assisted IGA in SCC initiation specimens, while for unstressed exposure coupons, the IGA depths only changed

slightly from beyond 1000 hours, which resulted in noticeable difference between measured IGA depth and fitted curves. The estimated growth constant, k_p, are plotted in Figure 59. As expected, the stressed testing shows highest IGA growth rate.

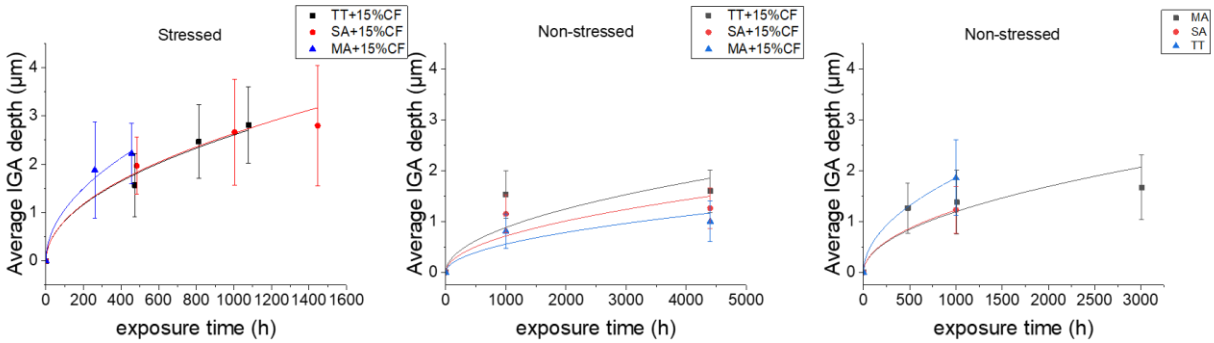

Figure 58. Fitting average IGA depth-exposure time measured in experimental data to Equation (21).

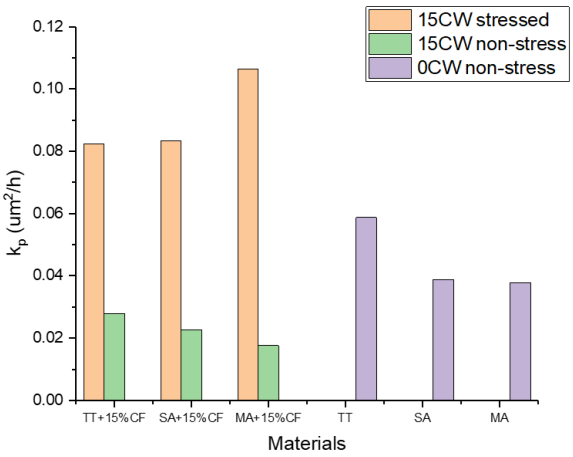

Figure 59. Estimated k_p for stressed and non-stressed tests on cold worked and non-cold worked specimens.

The overall distribution of precursor damage depth over time is also fitted using statistical distributions based on data acquired on the cumulative frequency of precursor damage depth as those presented in Figures 48-50. To find a suitable distribution description, comparison was made among log-normal, gamma, normal, Weibull and exponential models, for all datasets. The goodness of fitting metrics, such as R-squared, reduced Chi-squared, Akaike information criterion, and Bayesian information criterion, show that log normal model, Equation (22), performs noticeably better than other models in most datasets. We can see that the log normal distribution with parameters μ and σ, plotted as solid curves in Figure 60, fits well with the data in most cases.

$$CDF = \int_0^m \frac{1}{\sigma x\sqrt{2\pi}} exp(-\frac{(ln(x)-\mu)^2}{2\sigma^2})dx \quad (22)$$

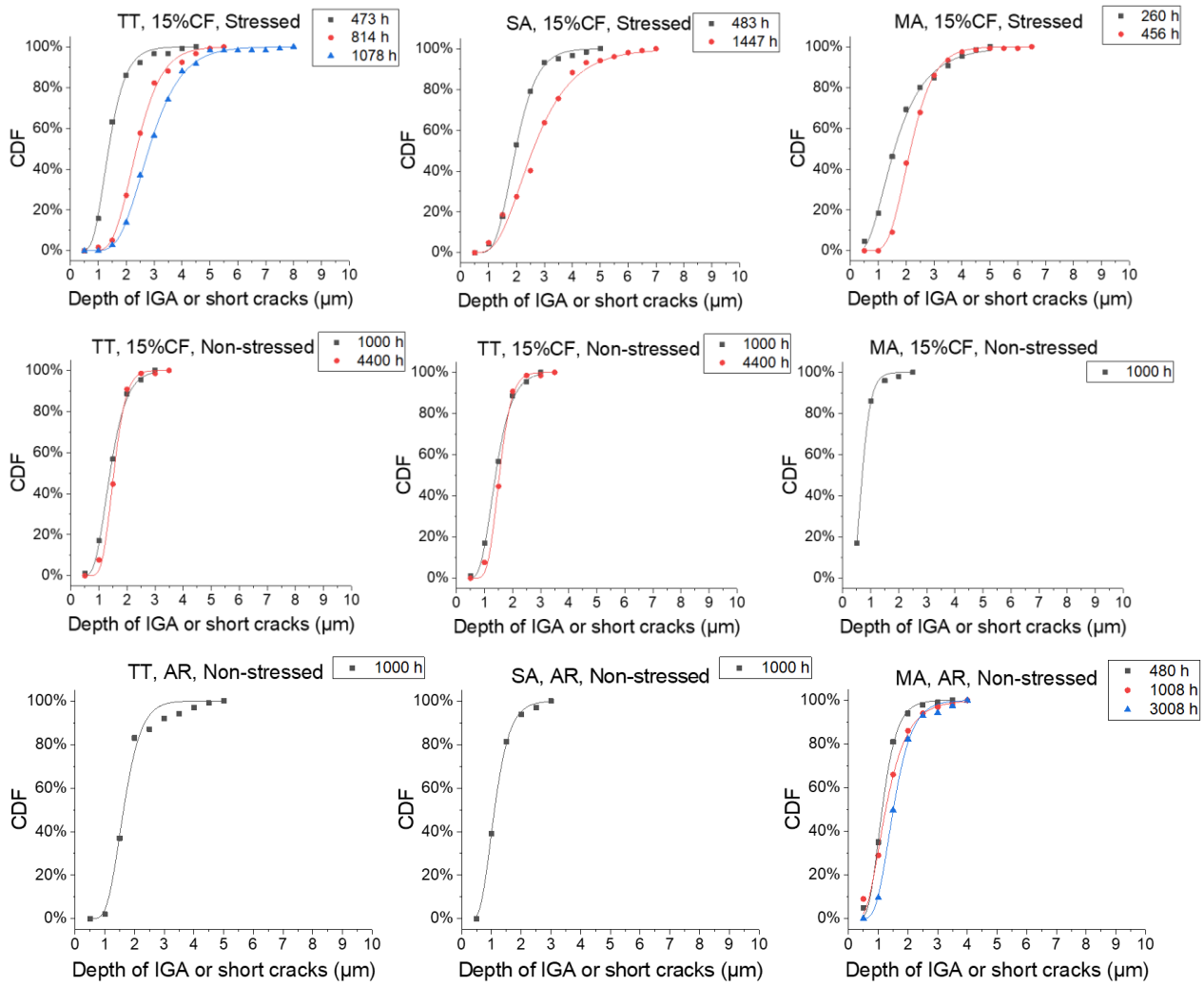

Figure 60. Fitting cumulative distribution functions for the IGA depth distributions among stressed and non-stressed tested cold worked and non-cold worked specimens. Solid lines are fitting of data. The log normal distribution is selected due to overall better performance in goodness of fitting after comparing log-normal, gamma, normal, Weibull and exponential models.

The average IGA depth in Equation (21) can be expressed using the mean of the log normal distribution of IGA depth, as shown in Equation (23). Therefore, the parameters determining the IGA depth distributions can be linked with time. Plotting these two parameters against time in Figure 61 shows that μ is strong correlated with time while there is no obvious trend for σ. For approximation, σ is set to around 0.33 where majority of estimated values reside, and the parameter μ is fitted with logarithm relationship with time.

$$exp(\mu + \frac{\sigma^2}{2}) = (k_p t)^{0.5} \tag{23}$$

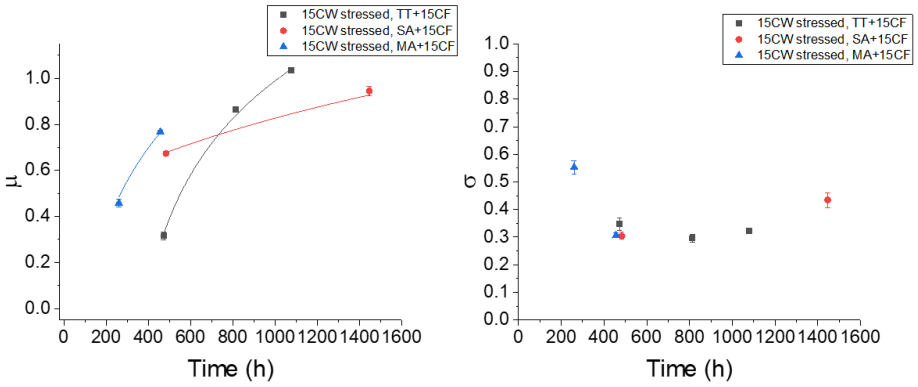

Figure 61. Parameters μ and σ as a function of time for stressed testing on 15%CF specimens.

Modeling the Transition from IGA to Short Crack

As discussed in the section of Key Steps Leading to Practical SCC Initiation, the change in kinetics from IGA growth to crack growth occurs when the precursor depth reaches a critical depth D_1. Note that different from what is proposed by Couvant et al. [17], this critical depth is not necessarily associated with oxide fracture making IGA become opened cracks, but rather a change in dominating mechanism that lead to faster growth of precursors. In fact, statistics (Figure 30) suggest that by the time precursor reaches D_1, all IGA have already become opened cracks but it is assumed that cracks with depth below D_1 grow very slowly similar to uncracked IGA. As shown in Figure 33, D_1 is strongly dependent on applied stress and cold work level and the dependence can be fit reasonably well with a logarithmic relationship in the form of:

$$D_1 = a\, ln(\frac{\sigma_{\text{applied}}}{\sigma_{\text{YS non-CW}}}) + b \tag{24}$$

where a and b are material dependent constants, and the stress ratio $\frac{\sigma_{\text{applied}}}{\sigma_{\text{YS non-CW}}}$ counts for the effect of cold work and applied stress. For most materials, a has a value close to -12 and b is generally ranging from 8–9.

Modeling Short Crack Growth

The most widely accepted prediction of PWSCC CGR in Alloy 600 correlates with the crack tip stress intensity factor K and is first proposed by Scott et al. [43] and later reinforced in MRP-55 [68] in the equation below:

$$CGR = A(K - K_{th})^B \tag{25}$$

where A is the crack growth amplitude constant, K_{th} is the stress intensity threshold below which crack growth is negligible, and B is an exponent coefficient. The widely used values for K_{th} and B were obtained through fitting field and laboratory data and are 9 and 1.16, respectively. However, the low-K CGR tests performed on multiple Alloy 600 heats in this study clearly demonstrates that crack growth can take place below 9 MPa√m. For 15%CF materials, the CGR at 9 MPa√m can be as high as in the orders of 10^{-8}–10^{-7} mm/s. To allow prediction of CGR in lower K levels, Equation (25) is revisited and updated to the form below that eliminates the K_{th} term:

$$CGR = AK^B \tag{26}$$

Our low-*K* CGR data presented in Figure 45b is fitted to Equation (26) and the results are shown in Figure 62 and Table 5.

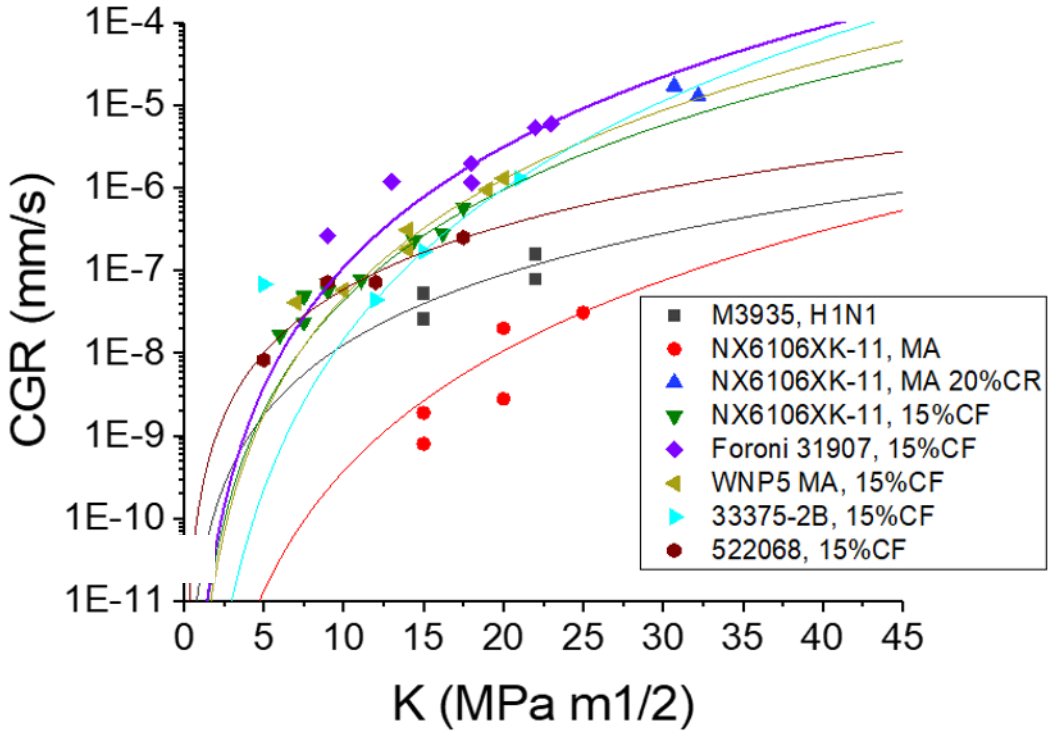

Figure 62. Curve fitting to Equation (26) using experimental data for each material.

Table 5. Summary of estimated fitting parameters for CGR-K relationships using Equation (26).

Materials	*A* ((um/hr)/(MPa√m))	*B*
M3935, MA non-CW	$6.746\pm4.192\times10^{-6}$	2.828±2.035
NX6106XK-11, MA non-CW	$2.009\pm13.017\times10^{-8}$	4.828±2.042
NX6106XK-11, MA 15%CF	$5.641\pm12.816\times10^{-6}$	4.444±0.809
Foroni 31907 15%CF	$5.853\pm17.108\times10^{-6}$	4.828±0.945
WNP5 MA 15%CF	$3.092\pm4.316\times10^{-6}$	4.742±0.472
33375-2B 15%CF	$4.815\pm11.335\times10^{-8}$	6.041±0.775
522068 15%CF	$5.966\pm9.250\times10^{-4}$	2.552±0.554

Recall that for short cracks, the crack tip stress intensity *K* is predicted using Equation (20) where stress intensity factor *F* is a necessary input dependent on crack shape and size. As shown in Figures 25 and 26, the shape of most short cracks prior to practical SCC initiation can be approximated to semi-elliptical. In addition, based on the quantitative information from Figure 28, cracks prior to practical SCC initiation tend to have a fixed aspect ratio (*a*/*b*) of ~0.8. This allows the value of *F* to be found in numerical tables published by FEM studies such as in Ref.[33] as a function of *a*/*D* for a fixed crack aspect ratio where *a* is the crack depth and *D* is the specimen gauge diameter. However, estimation of *F* is only possible at discrete *a*/*D* values using these tables and are plotted in solid square data points shown in Figure 63 for a fixed *a*/*b* = 0.8. To enable *F* to be predicted with continuously changing *a*/*D* that is needed for simulation, a curve fitting is performed on these data points as a quick solution. The best fit is

obtained via an exponential law in the form of Equation (27) and the fit is shown in the red curve in Figure 63.

$$F = y_0 + A\, exp(\, R_0(\frac{a}{D})) \tag{27}$$

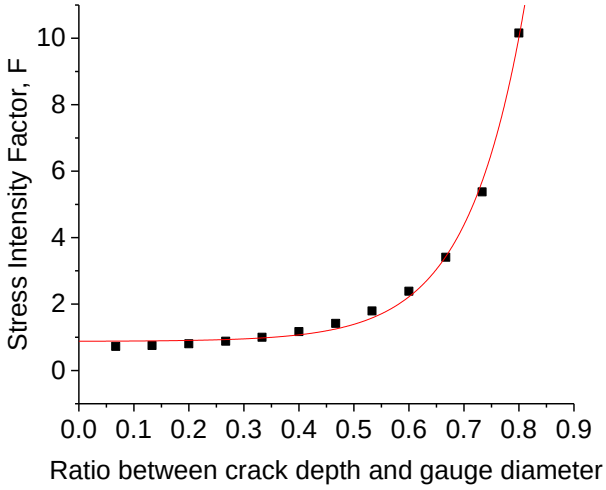

Figure 63. Fitting of stress intensity factor *F* against crack depth to gauge diameter ratio *a*/*D* using Equation (27). The *F* value was obtained from FEM in [33] assuming crack has an aspect ratio of ~0.8.

The proposed model detailed above provides mechanistic-based quantitative relationships derived using reliable experimental data for each step involved in the macroscopic SCC initiation behavior of Alloy 600. The point of practical SCC initiation is well defined and associated with a criterion that can be easily applied to realistic scenarios. The parameters in Equations (21), (24), and (26) are material based and can be determined for any given heat using data obtained from relatively simple, straight forward tests or existing database, enabling SCC initiation behavior to be quickly predicted for a wide range of materials. Meanwhile, it also has the flexibility to be used to evaluate SCC initiation behavior under the influence of factors other than applied stress and cold work by incorporating additional terms in the equations or in the equation parameters once the relationship can be confidently developed for the other factors.

Framework for Simulation

While the controlling processes have been identified in the key steps leading to practical SCC initiation and the corresponding kinetics based on key influencing parameters have been established, the impact of other parameters are not explicitly derived due to lack of/inclusive data. To count in these uncertainties, it might be inevitable to employ a Monte Carlo approach incorporating stochastic elements into the deterministic relationships we obtained in the previous sub-section for predicting practical SCC initiation. The outcome will be expressed with an associated probability. The simulation flow for modeling a single crack is illustrated in Figure 64 with inputs identified in the right column. Stochastic approach can be introduced in both the IGA development and short crack growth stages and is currently under evaluation. While in more realistic situations multiple crack initiation and growth, coalescence and dormancy need to be considered, these aspects fall into the field of mechanics studies rather than SCC studies therefore is beyond the scope of this project. We are currently seeking collaborations with other groups to further explore these topics.

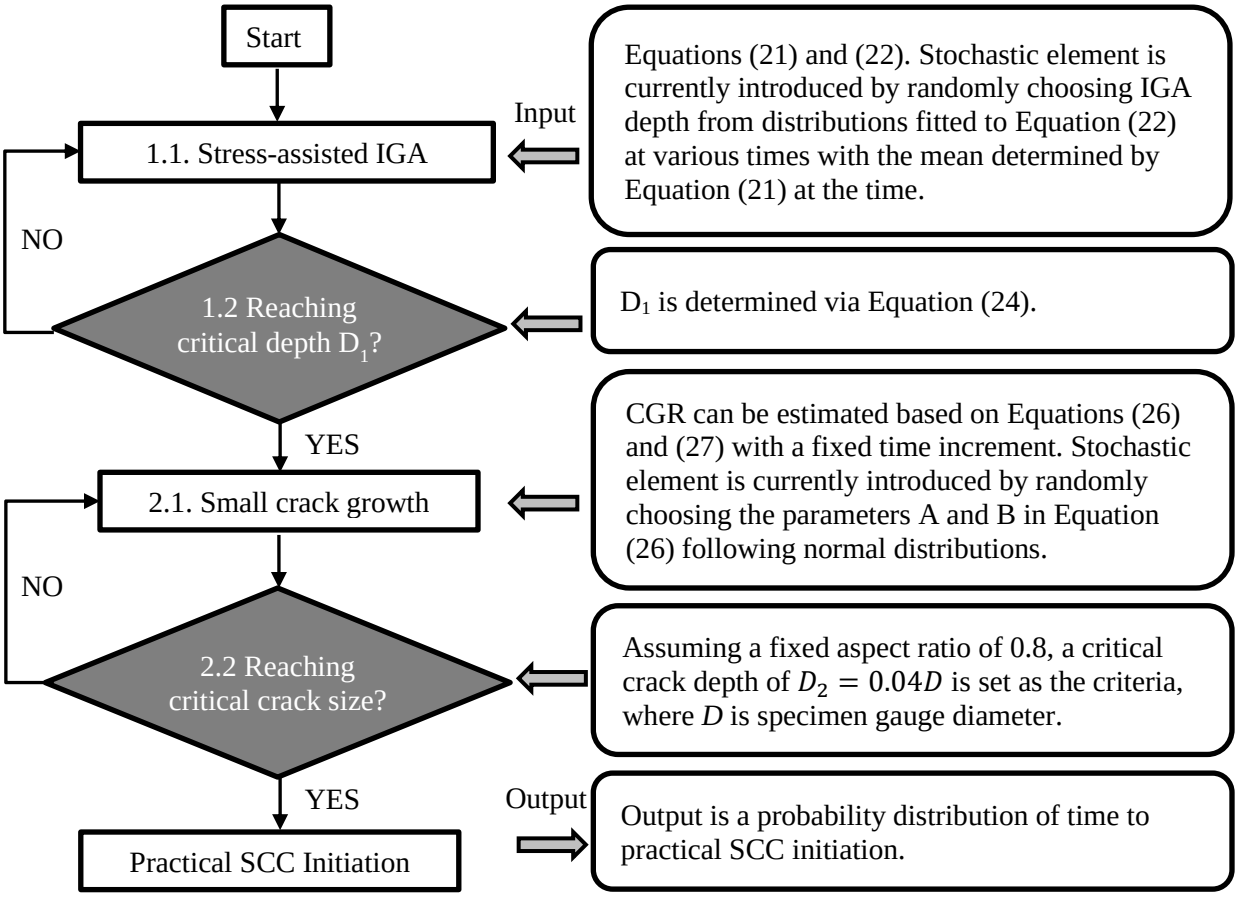

Figure 64. Schematics of the stochastic approach under development for estimating SCC initiation kinetics based on quantitative relationships determined in the previous section.

ALLOY 182 SCC INITIATION TEST RESULTS

As the compatible weld metal for Alloy 600, Alloy 182 continues to have a presence in pressure boundaries of existing pressurized water reactors, including locations where it is used to attach primary water piping to the reactor vessel or other structures. To support the joint NRC-EPRI xLPR program that seeks to better estimate the lifetime of Alloy 182 welds associated with primary water piping, SCC initiation measurements of Alloy 182 are under investigation at PNNL. LWRS does not directly fund the SCC initiation test and characterization activities on Alloy 182 but collaborates with an ongoing joint NRC-EPRI project through experience and resource sharing. The goal of the NRC-EPRI project is to produce SCC initiation data in support of a factor of improvement determination for Alloys 690/152/52 over Alloys 600/182, and to generate temperature, stress, and material strength dependencies for the Alloy 182 SCC initiation models being developed in the xLPR program. This is a multiyear test program with a large test matrix, and the testing to-date has first focused on the effect of material strength. In this chapter, a brief summary will be provided on Alloy 182 SCC test status, and the applicability of the SCC initiation model developed for Alloy 600 in the previous chapter to predict Alloy 182 SCC initiation behavior will be discussed.

Four welds of Alloy 182 from different sources were selected for this study with the bulk composition provided in Table 6. As part of the research scope, SCC CGR testing was performed on all these materials in their as-welded (AW) condition. All materials showed SCC susceptibility with Studsvik and KAPL welds exhibiting the highest CGRs. PNNL 30.5 mm (1.2 inches) tall uniaxial tensile specimens were used for the SCC initiation tests. Care was taken during specimen preparation to ensure that the gauge and the fillet of the specimens were always made entirely of the weld metal.

Table 6. Alloy 182 composition (wt% unless noted).

Heat #	Ni	Cr	Fe	Mn	Nb	Si	Ti	C	V	Al	Mo	Co	Cu	B*	P*	S*
KAPL 823030	68	11	7.2	8.6	2.9	0.81	0.88	NM†	0.027	0.02	0.0016	0.0075	0.0019	8	69	39
Studsvik 8001231	68	12	7.2	10	2.6	0.24	0.028	NM	0.035	0.0066	0.005	0.03	0.032	4.7	70	38
Phase 2B	69	11	7.5	9.9	2.3	0.39	0.47	NM	0.043	0.0094	0.065	0.018	0.028	5.7	55	62
Flawtech 844305	70	14	7.5	6	2.5	0.26	0.25	NM	0.02	0.022	0.073	0.038	0.015	0.36	100	19

* Unit in wt% ppm. † NM = not measured.

The early focus of the SCC initiation testing of Alloy 182 is on the effect of cold work in which all specimens are tested at material yield strength. To-date, assessments were mostly performed on materials in the 15%CF condition. The 15%CF condition was selected as the baseline condition for the Alloy 182 SCC initiation testing for its relevance to material conditions where initiations have been observed in the field and to serve as a test accelerant. The forging plane was aligned to the T-S orientation of the welds and specimens were aligned for cracking in the T-S orientation. Tests are being conducted on 36 specimens (9 from each of the four weld) in this condition with SCC initiation detected in eleven of them (5 from the Studsvik weld, 2 from the Phase 2B weld, and 3 from each of the two other welds). In general, Alloy 182 has initiations are strongly peaked towards very low initiation times with a tail out to very long initiation times. At least one specimens of each weld showed an initiation time below 150 hours, which is well below that of Alloy 600 with similar cold work levels. Meanwhile, the high initiation times generally exceeded the longest initiation times seen in Alloy 600 at this approximate cold work level (Figure 65).

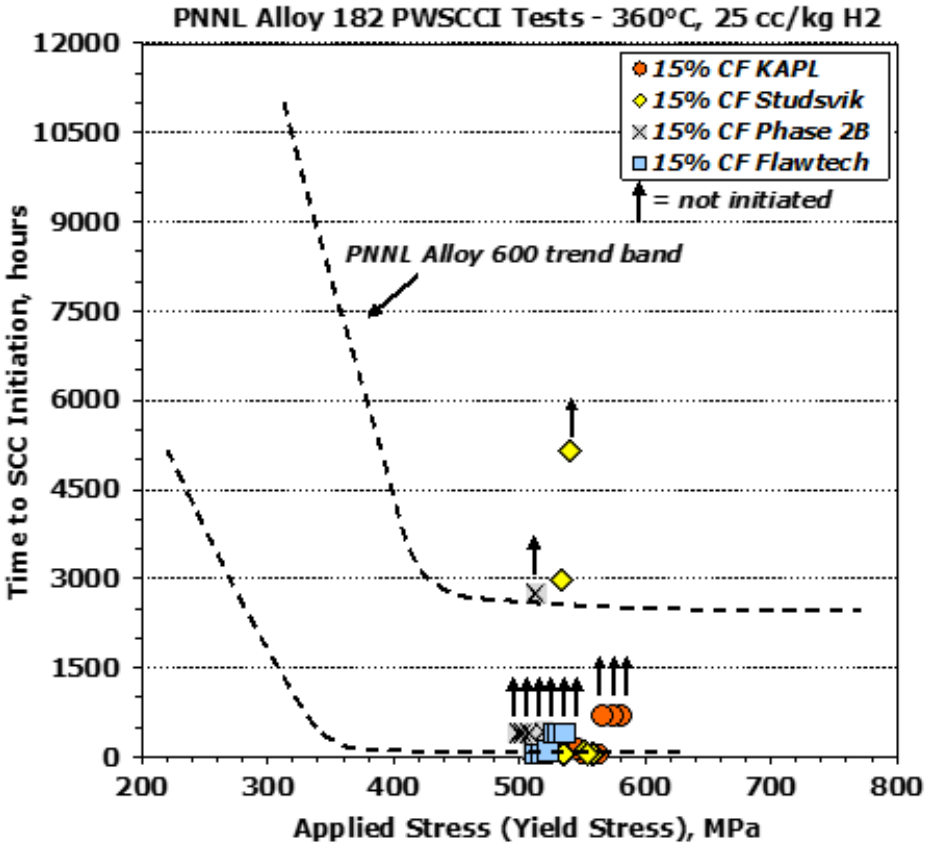

Figure 65. SCC initiation times measured by DCPD as a function of applied stress using for Alloy 182 materials tested at yield stress in 360°C simulated PWR primary water. Data credit to NRC-EPRI.

SEM examinations were carried out routinely on all specimens to record precursor and SCC initiation morphology prior and post to each test, and at test interruptions if applicable. Since Alloy 182 is known for its susceptibility to welding defects, one primary focus of the SEM examinations was to probe pre-existing defects on the surface and track their evolution during the testing periods. Small cracks ranging from tens to hundreds of micrometers in length were occasionally found on specimen surface and have been observed to result in rapid SCC initiation in the 15%CF materials. However, it should be noted that only two out of the 10 specimens with early initiation (SCC initiation time <150 hours) can be associated with pre-existing weld defects, suggesting there must be other factors that also played a role in causing the rapid SCC initiation. More detailed high microscopy examinations are underway to better understand this behavior. Cross-section examinations of tested specimens were not performed to the extent as in the LWRS research, but limited data also revealed IGA and short cracks preceding macroscopic SCC initiation. More details of the characterization results can be found elsewhere [69].

While tests on AW and low-CW conditions are in-progress under the NRC-EPRI program, systematic evaluation on the effect of cold work and applied stress is yet to be made. The limited data available for now revealed that IGA formation precedes crack nucleation in Alloy 182, which is similar to what was observed in Alloy 600. This suggests Alloy 182 initiation can be modeled following the same steps as those established for Alloy 600, i.e., through IGA development and short crack growth leading to crack reaching a critical size. Applied stress and cold work again seem to play a key role in the practical SCC initiation in Alloy 182, but early data suggest that the dependencies may be different from Alloy 600. As a result, the quantitative relationships developed to describe IGA and crack growth for Alloy 600 could not be readily applied to Alloy 182. More SCC initiation data needs to be collected and quantification of precursor damage evolution needs to be performed to establish quantitative relationships for Alloy 182

SCC initiation prediction. In addition, the observed highly variable response both for initiation times and for observed cracking behavior is suggestive of strong spatial variability of SCC susceptibility within the same weld. While investigation is underway to underpin the cause of this variability, it likely involves complex interactions between multiple factors and might be best treated by introducing stochastic into the modeling.

SUMMARY AND CONCLUSIONS

This report reviewed current knowledge on mechanistic understandings of PWSCC initiation behavior in Alloys 600 and 182 obtained through systematic SCC initiation research at PNNL. It also summarized the ongoing SCC initiation model development activities for Alloy 600. The practical SCC initiation in both Alloys 600 and 182 involves three stages: IGA development, short crack growth and coalescence, and transition to stable crack growth. Data acquired to-date enabled identification of critical parameters and establishment of quantitative relationships that are necessary for predicting material behavior in each step leading to practical SCC initiation in Alloy 600. The observation and quantification on IGA development suggest that it is governed by solid state diffusion process, whereas short crack growth and coalescence appear to be of mechanics nature. The transition between IGA and short crack signifies as the precursor depth reaching a critical value that is likely associated with a shift in growth kinetics from a diffusion-controlled process to a stress-intensity dominated one. The short cracks are sensitive to presence of other cracks, and their growth can be accelerated via coalescence or retarded due to stress shielding from neighboring cracks. The transition to stable crack growth at engineering relevant rates is found to be associated with crack reaching a critical shape with respect to specimen gauge diameter, at which point stable crack growth is established at engineering relevant rates and SCC initiation are detected by DCPD. In all these steps, the effect of applied stress and cold work (i.e. material strength) appear to be predominant over other parameters, and currently the SCC initiation model is based upon quantitative relationships developed in each of the above-mentioned steps on these two parameters. The investigation on temperature effects suggest that the SCC initiation dependency on temperature cannot be fitted with a classical Arrhenius relationship, indicating additional mechanisms might have played a role and requires further investigation. Other parameters appear to have minor impact on SCC initiation and for the moment they are treated as stochastic elements in the model. However, deterministic terms can be derived and added to the model if a better understanding becomes available.

The current limited data on Alloy 182 suggests there is a significant spatial variability in SCC susceptibility especially in the 15%CW condition, which challenges an explicit quantification on the effects of parameters for model development. Nevertheless, knowledge and experience gained with Alloy 600 have proven to be very helpful in understanding Alloy 182 behavior and will continue to be used to guide future testing and characterization activities for the on-going SCC initiation research on Alloy 182 for better predictions of its behavior.

REFERENCES

[1] R. Bandy, D.V. Rooyen, Stress Corrosion Cracking of Inconel Alloy 600 in High Temperature Water—An Update, Corrosion (Houston), 40 (1984) 425-430.

[2] C. Amzallag, S. Le Hong, C. Pagès, A. Gelpi, Stress Corrosion Life Assessment of Alloy 600 PWR Components, Ninth International Symposium on Environmental Degradation of Materials in Nuclear Power Systems—Water Reactors, (1999).

[3] D. Rudland, C. Harington, xLPR Version 1.0 Report, ML110660292, 2011.

[4] P.M. Scott, An overview of materials degradation by stress corrosion in PWRs, in: D. Féron (Ed.) Corrosion Issues in Light Water Reactors, Woodhead Publishing, 2007, pp. 3-24.

[5] Y.S. Garud, Incremental Damage Formulation and Its Application to Assess IGSCC Growth of Circumferential Cracks in a Tube, Corrosion (Houston), 47 (1991) 523-527.

[6] Y.S. Garud, R.S. Pathania, A simplified model for SCC initiation susceptibility in Alloy 600, with the influence of cold work layer and strength characteristics, in: Proceedings of the Ninth International Symposium on Environmental Degradation of Materials in Nuclear Power Systems - Water Reactors -, 1999, pp. 261-267.

[7] J.A. Gorman, K.D. Stavropoulos, A.R. McIlree, Guidelines for prediction of PWSCC in steam generator tubes, Societe Francaise d'Energie Nucleaire, France, 1994.

[8] Y. Garud, Stress Corrosion Cracking Initiation Model for Stainless Steel and Nickel Alloys, Electric Power Research Institute (EPRI): Palo Alto, CA, USA, (2009).

[9] S. Le Hong, C. Amzallag, A. Gelpi, Modelling of stress corrosion cracking initiation of Alloy 600 in primary water of PWRs, in: 9th International Symposium on Environmental Degradation of Materials in Nuclear Power Systems - Water Reactors, The Minerals, Metals & Materials Society, 1999, pp. 115-123.

[10] J.A. Gorman, R.W. Staehle, K.D. Stavropoulos, Statistical Analysis of Steam Generator Tube Degradation, EPRI NP-7493, 1991.

[11] R. Staehle, Bases for predicting the earliest penetrations due to SCC for Alloy 600 on the secondary side of PWR steam generators, Argonne National Laboratory, 2001, 2001.

[12] J.P. Park, C. Park, Y.-J. Oh, J.H. Kim, C.B. Bahn, Statistical analysis of parameter estimation of a probabilistic crack initiation model for Alloy 182 weld considering right-censored data and the covariate effect, Nuclear Engineering and Technology, 50 (2018) 107-115.

[13] C. Benhamou, C. Amzallag, Prediction of stress corrosion initiation time of alloy 600 PWR components, in: 14th International Conference on Environmental Degradation of Materials in Nuclear Power Systems - Water Reactors, American Nuclear Society, 2009, pp. 109-118.

[14] Y. Sakakibara, I. Shinozaki, G. Nakayama, T. Nan-Nichi, T. Fujii, Y. Shimamura, K. Tohgo, Monte Carlo Simulation Based on SCC Test Results in Hydrogenated Steam Environment for Alloy 600, in: J.H. Jackson, D. Paraventi, M. Wright (Eds.) Proceedings of the 18th International Conference on Environmental Degradation of Materials in Nuclear Power Systems – Water Reactors: Volume 2, Springer International Publishing, Cham, 2018, pp. 335-345.

[15] T. Couvant, Prediction of IGSCC as a Finite Element Modeling Post-analysis, in: J.H. Jackson, D. Paraventi, M. Wright (Eds.) Proceedings of the 18th International Conference on Environmental Degradation of Materials in Nuclear Power Systems – Water Reactors: Volume 2, Springer International Publishing, Cham, 2018, pp. 319-334.

[16] T. Couvant, M. Wehbi, C. Duhamel, J. Crepin, R. Munier, Development of a local model to predict IGSCC: preiliminary calibration of parameters for nickel alloys exposed to primary water, in: 17th International Conference on Environmental Degradation of Materials in Nuclear Power Systems - Water Reactors, Canadian Nuclear Society, 2015, pp.

[17] T. Couvant, J. Caballero, C. Duhamel, J. Crépin, T. Maeguchi, Calibration of the Local IGSCC Engineering Model for Alloy 600, in: J.H. Jackson, D. Paraventi, M. Wright (Eds.) Proceedings of

the 18th International Conference on Environmental Degradation of Materials in Nuclear Power Systems – Water Reactors: Volume 2, Springer International Publishing, Cham, 2018, pp. 295-317.
[18] R.A. Etien, E. Richey, D.S. Morton, J. Eager, SCC initiation testing of alloy 600 in high temperature water, in: 15th International Conference on Environmental Degradation of Materials in Nuclear Power Systems - Water Reactors, The Minerals, Metals & Materials Society, 2011, pp. 2274-2284.
[19] S.M. Bruemmer, M.J. Olszta, D.K. Schreiber, M.B. Toloczko, Corrosion and Stress Corrosion Crack Initiation of Cold Worked Alloy 600 and Alloy 690 in PWR Primary Water Environments, Technical Milestone Report M2LW-13OR0402035, Light Water Reactor Sustainability Program, DOE Office of Nuclear Energy, September 2014.
[20] M.J. Olszta, D.K. Schreiber, M.B. Toloczko, S.M. Bruemmer, Microstructure, Corrosion and Stress Corrosion Crack Initiation of Alloy 600 in PWR Primary Water Environments, Technical Milestone Report M3LW-13OR0403032, Light Water Reactor Sustainability Program, DOE Office of Nuclear Energy, March 2013.
[21] Z. Zhai, M.B. Toloczko, M.J. Olszta, S.M. Bruemmer, Stress corrosion crack initiation of alloy 600 in PWR primary water, Corrosion Science, 123 (2017) 76-87.
[22] Z. Zhai, M.B. Toloczko, M.J. Olszta, D.K. Schreiber, S. Bruemmer, Stress corrosion crack initiation of alloy 600 in simulated PWR primary water, Pacific Northwest National Laboratory: Technical Milestone Report M2LW-17OR0402034, Light Water Reactor Sustainability Program, DOE Office of Nuclear Energy, September 2017.
[23] M.B. Toloczko, M.J. Olszta, Z. Zhai, S.M. Bruemmer, Stress corrosion crack initiation measurements of alloy 600 in PWR primary water, in: 17th International Conference on Environmental Degradation of Materials in Nuclear Power Systems - Water Reactors, Canadian Nuclear Society, 2015, pp.
[24] P.L. Andresen, I.P. Vasatis, F.P. Ford, Behavior of short cracks in stainless steel at 288°C, in: CORROSION 1990, NACE, 1990, pp.
[25] E. Richey, D.S. Morton, M.K. Schurman, SCC initiation testing of nickel-based alloys using in-situ monitored uniaxial tensile specimens, in: 12th International Conference on Environmental Degradation of Materials in Nuclear Power Systems - Water Reactors, The Minerals, Metals & Materials Society, 2005, pp. 947-956.
[26] S.M. Bruemmer, M.J. Olszta, D.K. Schreiber, M.B. Toloczko, Stress Corrosion Crack Initiation of Cold-Worked Alloy 600 and Alloy 690 in PWR Primary Water, Pacific Northwest National Laboratory: Technical Milestone Report M2LW-14OR0404023, Light Water Reactor Sustainability Program, DOE Office of Nuclear Energy, September 2014.
[27] D.K. Schreiber, M.J. Olszta, K. Kruska, S.M. Bruemmer, Role of Grain Boundary Cr_5B_3 Precipitates on Intergranular Attack in Alloy 600, in: Proceedings of the 18th International Conference on Environmental Degradation of Materials in Nuclear Power Systems – Water Reactors: Volume 1, Springer International Publishing, 2018, pp. 359-374.
[28] D.K. Schreiber, M.J. Olszta, K. Kruska, Intergranular oxidation of thermally treated Alloy 600 coupons, Pacific Northwest National Laboratory: Technical Report DE-AC05-76RL01830, July 2018.
[29] D. Alley, D. Dunn, Testing and analyses of Davis-Besse UNS N06600 control rod drive mechanism nozzles, in: CORROSION 2015, NACE International, 2015, pp.
[30] S.M. Bruemmer, M.J. Olszta, D.K. Schreiber, N.R. Overman, M.B. Toloczko, Characterizations and Stress Corrosion Cracking Evaluations of Alloy 600 CRDM Nozzle Heats from the Davis Besse Nuclear Power Plant, NRC Report, August 2013.
[31] P.J. Meadows, P.L. Andresen, M.B. Toloczko, W.-J. Kuang, S. Ritter, M. Bjurman, L. Zhang, M. Ernestova, A. Toivonen, F. Perosanz-Lopez, J.W. Stairmand, K.J. Mottershead, International Round-Robin on Stress Corrosion Crack Initiation of Alloy 600 Material in Pressurized Water Reactor Primary Water, Corrosion (Houston), 76 (2020) 719-733.
[32] P. Scott, P. Combrade, R. Kilian, A. Roth, P. Andresen, Y. Kim, Status Review of Initiation of Environmentally Assisted Cracking and Short Crack Growth, 1011788, 2005.

[33] C.S. Shin, C.Q. Cai, Experimental and finite element analyses on stress intensity factors of an elliptical surface crack in a circular shaft under tension and bending, International Journal of Fracture, 129 (2004) 239-264.
[34] R.N. Parkins, P.M. Singh, Stress Corrosion Crack Coalescence, Corrosion (Houston), 46 (1990) 485-499.
[35] Y.Z. Wang, J.D. Atkinson, R. Akid, R.N. Parkins, Crack interaction, coalescence and mixed fracture mechanics, Fatigue & Fracture of Engineering Materials & Structures, 19 (1996) 51-63.
[36] Y.Z. Wang, K. Ebtehaj, D. Hardie, R.N. Parkins, The behaviour of multiple stress corrosion cracks in a Mn-Cr and a Ni-Cr-Mo-V steel: I—Metallography, Corrosion Science, 37 (1995) 1651-1675.
[37] Y.Z. Wang, K. Ebtehaj, D. Hardie, R.N. Parkins, The behaviour of multiple stress corrosion cracks in a Mn-Cr and a Ni-Cr-Mo-V steel: II—Statistical characterisation, Corrosion Science, 37 (1995) 1677-1703.
[38] Y.Z. Wang, D. Hardie, R.N. Parkins, The behaviour of multiple stress corrosion cracks in a Mn-Cr and a Ni-Cr-Mo-V steel: III—Monte Carlo simulation, Corrosion Science, 37 (1995) 1705-1720.
[39] O. Calonne, L. Fournier, P. Combrade, P. Scott, P. Chou, Experimental study of short crack coalescence in nickel-base alloys in PWR primary water, in: 15th International Conference on Environmental Degradation of Materials in Nuclear Power Systems -Water Reactors, The Minerals, Metals & Materials Society, 2011, pp. 1561-1578.
[40] X.J. Xin, E.R.D.L. Rios, Interactive effect of two coplanar cracks on plastic yielding and coalescence, Fatigue & Fracture of Engineering Materials & Structures, 17 (1994) 1043-1056.
[41] M.A. Astiz, An incompatible singular elastic element for two- and three-dimensional crack problems, International Journal of Fracture, 31 (1986) 105-124.
[42] A. Carpinteri, Elliptical-arc surface cracks in round bars, Fatigue & Fracture of Engineering Materials & Structures, 15 (1992) 1141-1153.
[43] P. Scott, An analysis of primary water stress corrosion cracking in PWR steam generators, in: NEA/CSNI Specialist Meeting on Operating Experience with Steam Generators, 1991, pp. 5-6.
[44] A.R. McIlree, R.B. Rebak, S. Smialowska, Relationship of stress intensity to crack growth rate of alloy 600 in primary water, in: International Colloquium on Contribution of materials Investigation to the Resolution of Problems Encountered in PWR Plants, Societe Francaise d'Energie Nucleaire, 1990, pp. 260-267.
[45] J. Hickling, A. Mcllree, R.S. Pathania, Materials Reliability Program (MRP) Crack Growth Rates for Evaluating Primary Water Stress Corrosion Cracking (PWSCC) of Thick-Wall Alloy 600 Materials (MRP-55) Revision 1, 1006695, 2002.
[46] S. Le Hong, Influence of Surface Condition on Primary Water Stress Corrosion Cracking Initiation of Alloy 600, Corrosion (Houston), 57 (2001) 323-333.
[47] J. Toribio, N. Álvarez, B. González, J.C. Matos, A critical review of stress intensity factor solutions for surface cracks in round bars subjected to tension loading, Engineering Failure Analysis, 16 (2009) 794-809.
[48] J. Robertson, The mechanism of high temperature aqueous corrosion of stainless steels, Corrosion Science, 32 (1991) 443-465.
[49] Z. Zhai, M.B. Toloczko, M.J. Olszta, S.M. Bruemmer, Grain boundary microstructure effects on stress corrosion crack initiation mechanisms in Alloy 600 and Alloy 690, Pacific Northwest National Laboratory: Technical Milestone Report M2LW-19OR0402031, Light Water Reactor Sustainability Program, DOE Office of Nuclear Energy, September 2019.
[50] R.N. Parkins, 1990 Plenary Lecture: Strain Rate Effects in Stress Corrosion Cracking, Corrosion (Houston), 46 (1990) 178-189.
[51] Z. Zhai, M. Toloczko, S. Bruemmer, Microstructural Effects on SCC Initiation in PWR Primary Water for Cold-Worked Alloy 600, in: J.H. Jackson, D. Paraventi, M. Wright (Eds.) Proceedings of the 18th International Conference on Environmental Degradation of Materials in Nuclear Power Systems – Water Reactors: Volume 1, Springer International Publishing, Cham, 2018, pp. 217-229.

[52] D.J. Paraventi, W.C. Moshier, Alloy 690 SCC Growth Rate Testing, in: Workshop on Cold Work in Iron- and Nickel-Base Alloys, EPRI, 2007, pp.
[53] D.R. Tice, S.L. Medway, N. Platts, J.W. Startmand, Crack Growth Testing on Cold Worked Alloy 690 in Primary Water Environment, in: 15th International Conference on Environmental Degradation of Materials in Nuclear Power Systems - Water Reactors, The Minerals, Metals & Materials Society, 2011, pp. 71-87.
[54] P. Andresen, M.M. Morra, A. Ahluwalia, Effect of deformation temperature, orientation and carbides on SCC of Alloy 690, in: 16th International Conference on Environmental Degradation of Materials in Nuclear Power Systems - Water Reactors, NACE International, 2013, pp.
[55] J.P. Berge, Importance of surface preparation for corrosion control in nuclear power stations, Materials Performance, 36 (1997) 56-62.
[56] D. Deforege, L. Duisabeau, S. Miloudi, Y. Therbault, T. Couvant, F. Vaillant, E. Lemaire, Learnings from EDF Investigation on SG Divider Plates and Vessel Head Nozzles: Evidence of Prior Deformation Effect on Stress Corrosion Cracking, in: Fontevraud 7 - Contribution of materials investigations to improve the safety and performance of LWRs, Société française d'énergie nucléaire, 2011, pp. 10.
[57] P. Scott, M.C. Meunier, F. Steltzlen, O. Calonne, M. Foucault, P. Combrade, C. Amzallag, Comparison of laboratory and field experience of PWSCC in alloy 182 weld metal, in: 13th International Conference on Environmental Degradation of Materials in Nuclear Power Systems - Water Reactors, Canadian Nuclear Society, The Minerals, Metals & Materials Society, 2007, pp. 186-206.
[58] O. Raquet, D. Feron, G. Santarini, J.M. Boursier, IGSCC of alloy 600 in PWR primary water influence of a cold worked layer on crack initiation, in: International Conference on Hydrogen Effects on Material Behaviour and Corrosion Deformation Interactions, 2003, pp. 761-770.
[59] R.A. Morris, N. Lewis, D.S. Morton, 3D Analysis of Surface Treatment Effect on the Oxidation of Grain Boundaries in Alloy 600, in: 16th International Conference on Environmental Degradation of Materials in Nuclear Power Systems - Water Reactors, NACE International, 2013, pp.
[60] F. Scenini, R.C. Newman, R.A. Cottis, R.J. Jacko, Effect of Surface Preparation on Intergranular Stress Corrosion Cracking of Alloy 600 in Hydrogenated Steam, Corrosion (Houston), 64 (2008) 824-835.
[61] E. Richey, D.S. Morton, R.A. Etien, SCC initiation testing of nickel-based alloys in high temperature water, in: 13th International Conference on Environmental Degradation of Materials in Nuclear Power Systems - Water Reactors, Canadian Nuclear Society, The Minerals, Metals & Materials Society, 2007, pp. 831-850.
[62] T. Cassagne, F. Vaillant, O. De Bouvier, P. Combrade, An update on the influence of hydrogen on the PWSCC of Nickel base alloys in high temperature water, in: the 8th International Symposium on Environmental Degradation of Materials in Nuclear Power Systems - Water Reactors, American Nuclear Society, 1997, pp. 307-315.
[63] D.S. Morton, S.A. Attanasio, G.A. Young, Primary Water SCC Understanding and Characterization Through Fundamental Testing in the Vicinity of the Nickel/Nickel Oxide Phase Transition, in: 10th International Conference on Environmental Degradation of Materials in Nuclear Power Systems - Water Reactors NACE International, 2001, pp. Medium: ED; Size: 782 Kilobytes pages.
[64] L. Fournier, O. Calonne, P. Combrade, P. Scott, P. Chou, R. Pathania, Grain boundary oxidation and embrittlement prior to crack initiation in Alloy 600 in PWR primary water, in: 15th International Conference on Environmental Degradation of Materials in Nuclear Power Systems - Water Reactors, The Minerals, Metals & Materials Society, 2011, pp. 1411-1421.
[65] C. Wagner, Theoretical Analysis of the Diffusion Processes Determining the Oxidation Rate of Alloys, Journal of The Electrochemical Society, 99 (1952) 369.
[66] J. Nguejio, J. Crépin, C. Duhamel, F. Gaslain, C. Guerre, F. Jomard, M. Maisonneuve, Diffusion Processes as Possible Mechanisms for Cr Depletion at SCC Crack Tip, in: J.H. Jackson, D. Paraventi, M. Wright (Eds.) Proceedings of the 18th International Conference on Environmental

Degradation of Materials in Nuclear Power Systems – Water Reactors: Volume 1, Springer International Publishing, Cham, 2018, pp. 337-357.
[67] J.D. Ramsay, H.E. Evans, D.J. Child, M.P. Taylor, M.C. Hardy, The influence of stress on the oxidation of a Ni-based superalloy, Corrosion Science, 154 (2019) 277-285.
[68] EPRI, Materials Reliability Program (MRP) - Crack Growth Rates for Evaluating Primary Water Stress Corrosion Cracking of Thick-Wall Alloy 600 Material (MRP-55), 2002.
[69] M. Toloczko, Z. Zhai, S. Bruemmer, SCC Initiation Behavior of Alloy 182 in PWR Primary Water, in: J.H. Jackson, D. Paraventi, M. Wright (Eds.) Proceedings of the 18th International Conference on Environmental Degradation of Materials in Nuclear Power Systems – Water Reactors: Volume 1, Springer International Publishing, Cham, 2018, pp. 137-160.